学　位　論　文

In Vitro and In Vivo Delivery of Drugs and siRNA Mediated by Water-Soluble Fullerenes

（水溶性フラーレンを用いた薬剤および siRNA
の in vitro，in vivo 輸送)

平成２４年１２月博士（理学）申請
東京大学大学院理学系研究科　化学専攻

南　　皓　輔

Abstract

Nanomaterials have gained much attention as their potential applications in the fields of material and biological sciences. Especially in the field of biomedical applications, development of drug delivery systems is a challenging work since improving drug efficacy and reducing side effects of drugs. Research efforts are focused on designing drug carriers, which effectively deliver into cells. For the carriers controlling the size in the range of several tens of nanometer to submicrometer and their surface functionalities are important subjects. Water-soluble fullerene derivatives form nano- to micrometer-sized aggregates and show unique structures in water due to the high hydrophobicity and strong cohesive force of fullerene backbones. Construction of well-controlled aggregated structures of fullerenes and their surface functionalities enables us to utilize them for biomedical applications. In this thesis, I have developed the fullerene-based nanomaterials and applied them for drug and siRNA delivery systems.

Chapter 1 describes the general introduction of drug and gene delivery systems. Especially, the concept, and recent approaches and challenges of the systems were emphasized. In addition, the use of [60]fullerene derivatives in biological and biomedical application was also discussed.

Chapter 2 describes a siRNA delivery using a water-soluble cationic fullerene in vitro. First half of this chapter is about the properties of the cationic fullerene, and its aggregates with and without siRNA in water. The latter half of this chapter is the application for the siRNA delivery in vitro.

Chapter 3 describes a lung-specific siRNA delivery via agglutination-induced lung accumulation using the water-soluble cationic fullerene. Agglutination of fullerene-siRNA complexes with plasma proteins was investigated. Accumulation of the agglutinated fullerene-siRNA complexes and specific delivery of siRNA in lung were studied, and I discuss the lung-specific delivery of siRNA. Finally, I studied this system for the therapeutic applications.

Chapter 4 describes a development of post-functionalization of a fullerene vesicle, and its application as a drug delivery vehicle. Stepwise-modified fullerene vesicles were evaluated by dynamic light scattering and electron microscopic analyses. The use of a state-of-art, subnanometer spatial resolution, low-accelerating-voltage scanning electron microscopy was emphasized. Finally, I describe that this vesicle showed the ability of drug delivery.

Finally, the summary and future prospects of this study and drug delivery systems are stated in chapter 5.

Acknowledgement

I would like to express my sincerest gratitude to my research mentor, Professor Eiichi Nakamura, for educating me to be a researcher and giving me a wonderful opportunity to research this interesting project, which stand not only on chemistry but also on biology. His professional guidance and evocative suggestions greatly contributed to the success of this project.

I am indebted to Dr. Koji Harano for having fruitful discussions about this project, giving me meaningful advices, taking SEM and STEM images, and his persistent and great efforts to understand biological results about this project.

I owe a very important debt to Dr. Eisei Noiri and Dr. Kent Doi in the medical school of the University of Tokyo for giving me a great opportunity to research this project, and precious discussions and advices about this project. Without their supports I could not have written this thesis.

I also thank other staff members of Nakamura's group; Dr. Hayato Tsuji, Dr. Laurean Ilies, Dr. Hideyuki Tanaka, and Dr. Shunsuke Furukawa for their guidance in specific techniques and skills of experiments and their valuable and encouraging suggestions. Two of the former staff member of Nakamura's group: Professor Yutaka Matsuo in the University of Tokyo and Dr. Naohiko Yoshikai in Nanyang Technological University are also gratefully acknowledged.

I am grateful to my senior student, Dr. Tatsuya Homma for giving me enthusiastic training not only about experimental techniques and skills of the chemistry research but also about the researcher's life. I learned much from him, and keep trying to do my best to be a great scientist like him.

I would like to thank Dr. Koji Okamoto in Noiri's group for his helpful guidance in unfamiliar techniques and skills of biological experiments and his insightful suggestions.

I would like to thank Dr. Waka Nakanishi in Tohoku University and Dr. Rui Maeda-Mamiya in Tsukuba University previously for their advice of previous studies about the DNA transfection experiments using cationic fullerenes.

I want to thank all of the members in Nakamura's group, especially the members in Harano's subgroup; Ms. Utako Takeda, Mr. Ricardo Mizoguchi Gorgoll, Mr. Hirohisa Nitta, Mr. Satoshi Okada, Mr. Junya Yamada, Mr. Takakazu Seki and Mr. Kei Matsumoto. I also wish to acknowledge former members in Harano's subgroup; Dr. Li-Fu Huang, Mr. Shinya Takenaga, Mr. Akimitsu Narita, Mr. Dennis Chung-Yang Huang, Ms. Eri Nishiyama, Mr. Shinichiro Mizuno, Ms. Kaori Kubo, Ms. Mami Nakatake. I also want to thank all colleagues who studied with me as the same grade; Mr. Masaki Sekine, Mr. Tatsuo Kojima, Mr. Masashi Maruyama, Mr. Yuki Yokoi, Ms. Hiromi Ohyama, Mr. Jun Okabe, and Mr. Iku Tanaka.

I want to thank all previous and present members in Noiri's group; Dr. Kohsuke Negishi, Dr. Yoshifumi Hamasaki, Dr. Kenjiro Honda, Dr. Daisuke Katagiri, Dr. Maki Tsukamoto, and Dr. Emi Ogasawara.

I also want to thank the members of my previous group in Department of Agricultural and Environmental Science, The University of Tokyo, from which I graduated; Dr. Susumu Katsuma and Dr. Shinpei Kawaoka for their guidance in techniques and skills of genetics and molecular biology and for their discussions.

As for AFM measurements, I thank Dr. Ohta, Dr. Moriguchi and Dr. Kogure from Shimadzu Co., Ltd (Chapter 2).

I would like to thank the Japan Society for the Promotion of Science for their financial support as a predoctoral fellowship. I also would like to thank the University of Tokyo Global COE program, "Chemistry Innovation through Cooperation of Science and Engineering" for their financial support as a research assistant.

Finally, I would like to thank my parents, Kenji Minami and Nami Minami, and my brother, Taisuke Minami for their continuous encouragements and financial support throughout 9 years study in the University of Tokyo.

Kosuke Minami

Hongo, Tokyo

December 2012

List of Publications

"Protein-coated nanocapsules *via* multilevel surface modification. Controlled preparation and microscopic analysis at nanometer resolution." Harano, K.; Minami, K.; Noiri, E.; Okamoto, K.; Nakamura, E. *Chem. Commun.* **2013**, *49*, 3525–3527.

Publications Not Included in This Thesis

"Developmentally synchronized expression of two *Bombyx mori* Piwi subfamily genes, *SIWI* and *BmAGO3* in germ-line cells." Kawaoka, S.; Minami, K.; Katsuma, S.; Mita, K.; Shimada, T. *Biochem. Biophys. Res. Commun.* **2008**, *367*, 755–760.

Abbreviations

2,6-ANS:	2-anilinonaphthalene-6-sulfonic acid
Å:	angstrom
A:	ampere(s); adenine
AFM:	atomic force microscopy
Anal.:	combustion elemental analysis
APCI:	atmospheric pressure chemical ionization
aq:	aqueous
BF:	bright field
Boc:	*tert*-butoxycarbonyl
bp:	base pair(s)
Br:	brain
Bu:	butyl
C:	cytosine
°C:	degrees Celsius
calcd:	calculated
CCD:	charge-coupled device
cDNA:	complementary deoxyribonucleic acid
d:	day(s); doublet (spectral)
DDS:	drug delivery system(s)
DEPT:	distorsionless enhancement by polarization transfer
DLS:	dynamic light scattering
D-MEM:	Dalbecco's modified Eagle's medium
DMPU:	1,3-dimethyl-3,4,5,6-tetrahydro-2(1*H*)-pyrimidinone
DMSO:	dimethyl sulfoxide
DNA:	deoxyribonucleic acid
DNase:	deoxyribonuclease
DOX:	doxorubicin
EDX:	electron dispersive x-ray spectroscopy
EGFP:	enhanced green fluorescent protein
ELISA:	enzyme-linked immunosorbent assay
EPR:	enhanced permeation and retention (effect)
eq:	equation; equivalent
et al.:	and others
eV:	electron volt(s)
FBS:	fetal bovine serum
FT:	Fourier transform
g:	gram(s)
G:	guanine
GFP:	green fluorescent protein
GPC:	gel permeation chromatography
h:	hour(s)
H&E:	hematoxylin and eosin (staining)
HEK:	human embryonic kidney
HOPG:	highly oriented pyrolytic graphite
hpf:	high-power field
HPLC:	high-performance liquid chromatography
HRMS:	high-resolution mass spectroscopy
Ht:	heart
Hz:	hertz
IC_{50}:	half maximal inhibitory

	concentration
IR:	infrared
i.t.:	intratracheal injection
ITO:	indium-tin-oxide
i.v.:	intravenous injection
J:	coupling constant (in NMR spectrometry)
k:	prefix to unit denoting kilo (kV)
K:	kelvin(s) (absolute temperature)
Kd:	kideny
L:	liter(s)
Lg:	lung
Lv:	liver
m:	meter(s); multiplet (spectral); prefix to unit denoting milli (mM)
M:	molar (moles per liter); prefix to unit denoting mega (MHz)
min:	minute(s)
mRNA	messenger ribonucleic acid
MS:	mass spectroscopy
MTT:	3-(4,5-di*m*ethyl*t*hiazol-2-yl)-2,5-diphenyl-*t*etrazolium bromide
n:	prefix to unit denoting nano (nm)
NMR:	nuclear magnetic resonance
N/P:	nitrogen-to-phosphorous (ratio)
ODCB:	*o*-dichlorobenzene
ODS:	octadecylsilyl
p:	prefex to unit denoting pico (pA)
P:	p value (statistics)
P:	peritoneum
PBS:	phosphate buffered serine
PCR:	polymerase chain reaction
PDI:	polydispersity index
PEG:	polyethylene glycol
ppm:	part(s) per million
q:	quartet (spectral)
qRT-PCR:	quantitative real-time reverse transcriptase-polymerase chain reaction
R:	reagent-to-base pair ratio (*R* value was calculated by dividing the nitrogen-to-phosphorus (N/P) ratio by 2.)
RNA:	ribonucleic acid
RNAi:	ribonucleic acid interference
ROS:	reactive oxygen species
rpm:	revolutions per minute
rt:	room temperature
s:	second(s); singlet (spectral)
SD:	standard deviation
SEM:	scanning electron microscopy; standard error mean (statistics)
siGFP:	GFP-targeted small interfering ribonucleic acid (siRNA)
siNEG:	scrambled small interfering ribonucleic acid (siRNA)
siRNA:	small interfering ribonucleic acid
siTLR4:	TLR4-targeted small interfering ribonucleic acid (siRNA)
Sp:	spleen
STEM:	scanning transmission electron microscopy
t:	triplet (spectral)
T:	thymine
TBAF:	tetrabutylammonium fluoride
TEG:	tetra(ethylene)glycol

TEM:	transmission electron microscopy
THF:	tetrahydrofuran
TIPS:	triisopropylsilyl
TLC:	thin-layer chromatography
TLR4:	toll-like receptor 4
Tm:	melting temperature
TOF:	time-of-flight
TPFE:	tetra(piperazino)fullerene epoxide
UV:	ultraviolet
V:	volt(s)
vis:	visible
W:	watt(s)
WD:	working distance
δ:	chemical shift in parts per million downfield from tetramethylsilane
λ_{em}:	emission wavelength
λ_{ex}:	excitation wavelength
μ:	prefix to unit denoting micro (μm)

Table of Contents

Chapter 1. General Introduction

1.1. Drug delivery systems

Drug delivery systems (DDS) have emerged a central focus in drug delivery research, as it can reduce non-specific toxicity and/or enhance efficacy of therapy. Main focus of DDS researches can be divided two major delivering targets: drugs and genes. Most of drugs have no selectivity between normal and diseased cells or tissues. Therefore, research efforts are currently focused on designing biocompatible carriers with ability of controlling release of drugs and of targeting to diseased cells or tissues. By comparison of drugs, gene therapy has a high selectivity towards genetic disorders using oligonucleotides. However, oligonucleotides, such as DNA and RNA, are rapidly degraded by nucleases in human body. Research efforts are always focused on designing effective carriers that compact and protect oligonucleotides for gene therapy.

1.1.1 Carriers for drug delivery

As for the candidates of the drug carriers nanometer-sized materials are usually studied, such as nanoparticles, micelles, vesicles, dendrimers, nanoshells and polymer nanospheres, because of the efficiency of cellular uptakes. Of these materials, liposomes have been most widely studied,[1] because of the possibility of liposomes to modify with the various functionalities (Figure 1-1).[2] Conventional liposomes composed of typical phospholipid (neutral and/or negative) are either neutral or negatively charged, but for the cationic liposomes there are several way to impose a positive charge. For prolonging circulation time sterically stabilized or "Stealth" liposomes carry polymer coatings, such as polyethylene glycol (PEG). Liposomes with specific reactivity have also developed, such as immunoliposomes, in which liposomes embedded antibodies for targeting selective cells and tissues. However, the flexible structure of liposomes leads to the instability of carriers and artificial

lipids cause the toxicity of carriers.

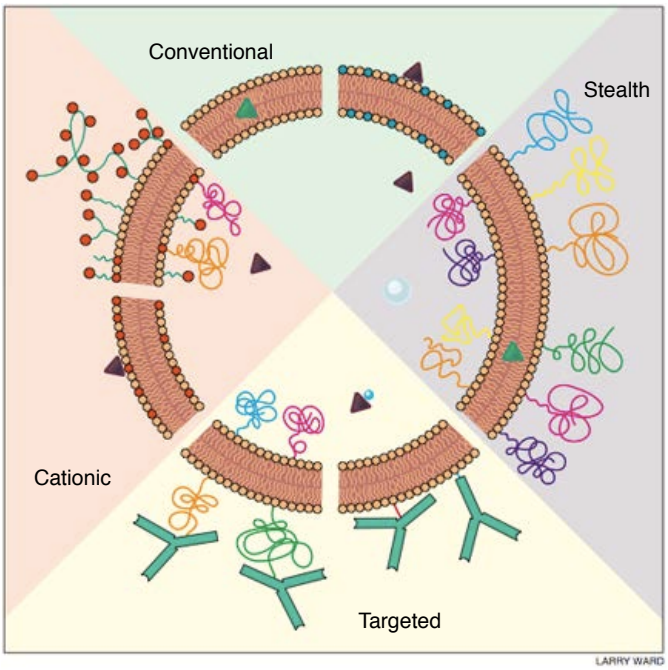

Figure 1-1. Schematic illustration of four major types of liposomes. Different modes of hydrophobic and hydrophilic drugs association with liposomes are also shown as green and purple triangles, respectively. Neutral, negatively charged and positively charged lipids represent in orange, blue and red, respectively. Sterically stabilized ("stealth") liposomes carry polymer coatings. Y-shaped objects indicate the antibodies. Ref. 2.

1.1.2 Carriers for gene transfection

As for the candidates of the gene delivery carriers, viral vectors have been initially studied, including both retro- and adenoviruses, as these viruses exhibited high efficiency of delivering both DNA and RNA. However, there are fundamental problems, such as toxicity, immunogenicity, and limitation with scale-up procedures. Recently, cationic nanocarriers, such as liposomes, polymers, dendrimers, and nanoparticles, are focused as a non-viral vector system.[3] The cationic components interact with and neutralized polyanionic nature of oligonucleotides by electrostatic interactions, thereby condensing the oligonucleotides into more compact structures. Cationic liposomes have been

already utilized as a biotechnology, such as Lipofectin and Lipofectamine, both are commercially available lipid-based carriers. However, the cationic carriers, especially cationic liposomes, show dose-dependent cyto- and organ toxicities depending on the polyvalent cationic species.[4]

1.2. Water-soluble fullerene derivatives for drug delivery systems

One promising alternative nanocarrier to liposomes and other carriers is carriers composed of carbon nanoclusters, especially [60]fullerene derivatives. Fullerene is a family of carbon allotropes. The existence of fullerene was first predicted by Osawa in 1970,[5] and its structure was discovered by Kroto, Curl, and Smalley in 1985[6] as the spherical I_h-symmetric soccer ball structure (Scheme 1-1). Since the discovery, chemical and physical properties of fullerenes, especially [60]fullerene, have been extensively investigated.[7] The discovery of various functionalization methods, such as chemical reactions with nucleophiles, such as amines,[8,9] organolithium reagents,[10] Grignard reagents,[10] organocopper reagents,[11] activated methylenes (Bingel reaction),[12] carbenes,[13] 1,3-dipolar cycloaddition of azomethine ylides (Prato reaction),[14] and Diels-Alder reactions with dienes[15] and anthracene,[16] is capable of modifying highly hydrophobic fullerene with hydrophilic groups to create water-soluble and biocompatible fullerenes. Therefore, recently water-soluble fullerenes have gained significant attention as a potential component of biomedical applications,[17] such as enzyme inhibition,[18,19,20] DNA photocleavage,[21,22] photodynamic therapy,[23,24] neuroprotection[25], apoptotic protection,[26] and inhibition of viral infection,[27] owing not only to the electronic and hydrophobic properties of the fullerene but also to its size of the fullerene core, which fits in the pocket of the binding sites of enzymes.[18]

Scheme 1-1. Reactions of [60]fullerene.

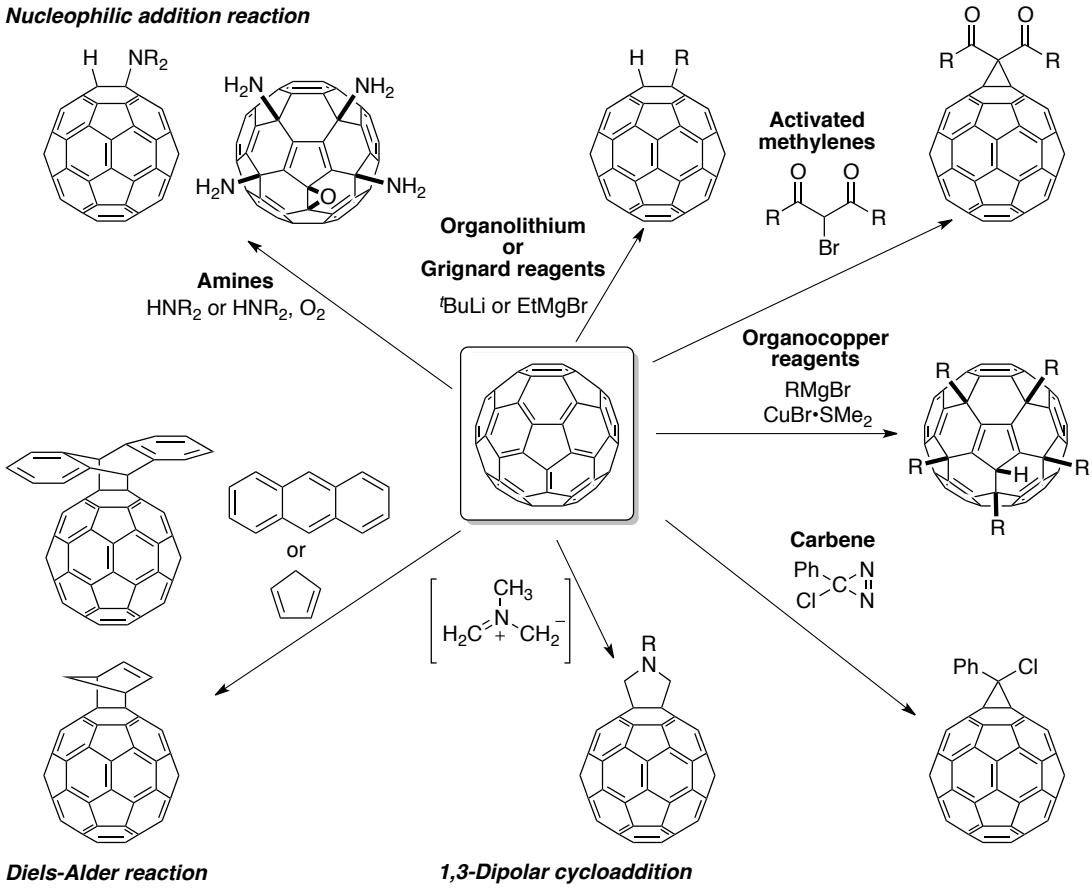

One of the significant features of the fullerenes is the high cohesive force between fullerenes. By utilizing the high cohesive force combined with the high hydrophobicity of fullerene, the water-soluble fullerene derivatives show unique self-assembled structures in water, such as rods,[28, 29] wires,[30] nanoparticles,[31] micelles[28, 32] and vesicles.[33, 34] For example, Hirsch et al. have reported that amphiphilic fullerene hexa-addcut **1** form vesicular structure, so-called buckysome, with a diameter ranging from 100 to 400 nm (Figure 1-2).[34] Interestingly, a fluorescein-labeled buckysome associated with human coronary artery endothelial cells.[35] Moreover, Conyers et al. achieved a delivery of hydrophobic molecules to the cells using this motif.[36]

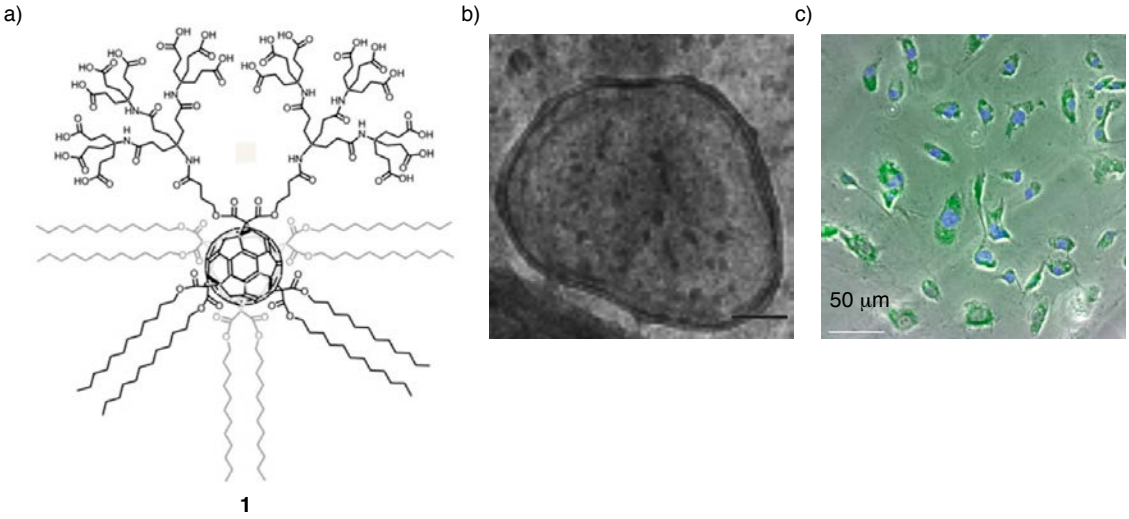

Figure 1-2. Fullerene-based nanocarriers for the delivery of hydrophobic molecules. a) Structure of amphiphilic fullerene hexa-adduct **1**. b) Cryo-transmission electron microscopy (TEM) image of buckysome. c) Superimposed image of hexa-adduct-coupled fluorescein and DAPI emission and bright field image of cells.

More recently, Zeng and Wu et al. have reported water-dispersible fullerene aggregates for both chemo- and photodynamic therapey.[23] Authors covalently incorporated doxorubicin (DOX)-based prodrugs and folic acid-based targeting ligand onto fullerenes. The functionalized fullerene formed nanometer-sized aggregates in water. The aggregates delivered in cancer cells by folic acid, and under acidic condition like cancer cells the aggregates released DOX due to the acid-mediated cleavage of the bond between drug and carrier. Moreover, they also achieved the photodynamic therapy because the fullerene aggregates themselves exhibited a photodynamic effect upon irradiation of light.

In addition, fullerene-based gene transfection agents have also been reported (Chart 1-1).[37, 38] Two kinds of tetraamino-fullerenes, two-handed fullerene **2** and tetra(piperazino)fullerene epoxide (TPFE), are a unique amphiphile possessing fullerene as a central core with four cationic amino

groups on one side of fullerene. The four cationic amines exert strong electrostatic interactions with phosphate backbones of DNA duplex, and the fullerene core provides a hydrophobic interaction for condensing of DNA and also for delivering the DNA into the interior of the target cells.

Chart 1-1. Structures of fullerene-based gene transfection agents.

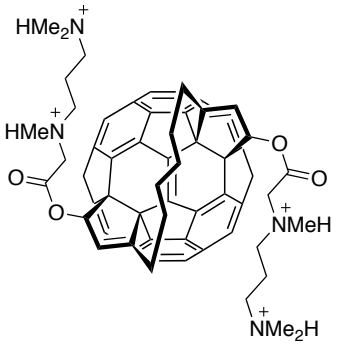

Two-handed fullerene **2**

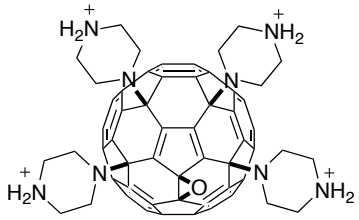

Tetra(piperazino)fullerene epoxide (TPFE)

References

[1] Storm, G.; Crommelin, D. J. A. *Pharm. Sci. Technol. Today* **1998**, *1*, 19–31.

[2] Lasic, D. D. *Sci. Am. Sci. Med.* **1996**, *3*, 34–43.

[3] Mintzer, M. A.; Simanek, E. E. *Chem. Rev.* **2009**, *109*, 259–302.

[4] Dokka, S.; Tokedo, D.; Shi, X.; Castranova, V.; Yojanasakul, Y. *Pharm. Res.* **2000**, *17*, 521–525.

[5] Osawa, E. *Kagaku* **1970**, *25*, 854–863.

[6] Kroto, H. W.; Heath, J. R.; O'Brien, S. C.; Curl, R. F.; Smalley, R. E. *Nature* **1985**, *318*, 162–163.

[7] López, A. M.; Mateo-Alonso, A.; Prato, M. *J. Mater. Chem.* **2011**, *21*, 1305–1318.

[8] Hirsch, A.; Li, Q.; Wudl, F. *Angew. Chem. Int. Ed. Engl.* **1991**, *30*, 1309–1310.

[9] Isobe, H.; Tanaka, T.; Nakanishi, W.; Lemiègre, L.; Nakamura, E. *J. Org. Chem.* **2005**, *70*, 4826–4832.

[10] Hirsch, A.; Soi, A.; Karfunkel, H. R. *Angew. Chem. Int. Ed. Engl.* **1992**, *31*, 766–768.

[11] (a) Sawamura, M.; Iikura, H.; Nakamura E. *J. Am. Chem. Soc.* **1996**, *118*, 12850‑12851. (b) Matsuo, Y.; Muramatsu, A.; Tahara, K.; Koide, M.; Nakamura, E. *Org. Synth.* **2006**, *83*, 80–87.

[12] Bingel, C. *Chem. Ber.* **1993**, *126*, 1957–1959.

[13] (a) Komatsu, K.; Kagayama, A.; Murata, Y.; Sugita, N.; Kobayashi, K.; Nagase, S.; Wan, T. S. M. *Chem. Lett.* **1993**, *22*, 2163–2166. (b) Yamago, S.; Tokuyama, H.; Nakamura, E.; Kikuchi, K.; Kananishi, S.; Sueki, K.; Nakahara, H.; Enomoto, S.; Ambe, F. *Chem. Biol.* **1995**, *2*, 385–389.

[14] Maggini, M.; Scorrano, G.; Prato, M. *J. Am. Chem. Soc.* **1993**, *115*, 9798–9799.

[15] Rubin, Y.; Khan, S.; Freedberg, D. I.; Yeretzian, C. *J. Am. Chem. Soc.* **1993**, *115*, 344–345.

[16] Schlueter, J. A.; Seaman, J. M.; Taha, S.; Cohen, H.; Lykke, K. R.; Wang, H. H.; Williams, J. M. *J. Chem. Soc., Chem. Commun.* **1993**, 972–974.

[17] Parth, R.; Conyers, J. L. *Int. J. Nanomed.* **2009**, *4*, 261–275.

[18] Friedman, S. H.; DeCamp, D. L.; Sijbesma, R. P.; Srdanov, G.; Wudl, F.; Kenyon, G. L. *J. Am. Chem. Soc.* **1993**, *115*, 6506–6509.

[19] Isobe, H.; Cho, K.; Solin, N.; Werz, D. B.; Seeberger, P. H.; Nakamura, E. *Org. Lett.* **2007**, *9*, 4611–4614.

[20] Maoyong, S.; Guibin, J.; Junfa, Y.; Hailin, Y. *Chem. Commun.* **2010**, *46*, 1404–1406.

[21] Tokuyama, H.; Yamago, S.; Nakamura, E. *J. Am. Chem. Soc.* **1993**, *115*, 7918–7919.

[22] Boutorine, A. S.; Tokuyama, H.; Takasugi, M.; Isobe, H.; Nakamura, E.; Hélène, C. *Angew. Chem. Int. Ed. Engl.* **1994**, *33*, 2462–2465.

[23] Fan, J.; Fang, G.; Zeng, F.; Wang, X.; Wu, S. *Small* **2013**, *9*, 613–621.

[24] Mizuno, K.; Zhiyentayev, T.; Huang, L.; Khalil, S.; Nasim, F.; Tegos, G. P.; Gali, H.; Jahnke, A.; Wharton, T.; Hamblin, M. R. *J. Nanomed. Nanotechnol.* **2011**, *2*, 2–8.

[25] Dugan, L. L.; Turetsky, D. M.; Du, C.; Lobner, D.; Wheeler, M.; Almli, C. M.; Shen, C. K.-F.; Luh, T.-Y.; Choi, D. W.; Lin, T.-S. *Proc. Natl. Acad. Sci. U. S. A.* **1997**, *94*, 9434–9439.

[26] Hu, Z.; Guan, W.; Wang, W.; Huang, L.; Xing, H.; Zhu, Z. *Cell Biol. Int.* **2007**, *31*, 798–804.

[27] Luczkowiak, J.; Munoz, A.; Sanchez-Navarro, M.; Ribeiro-Viana, R.; Ginieis, A.; Illescas, B. M.; Martín, N.; Delgado, R.; Rojo, J. *Biomacromol.* **2013**, *14*, 431–437.

[28] Cassell, A. M.; Asplund, C. L.; Tour, J. M. *Angew. Chem. Int. Ed.* **1999**, *38*, 2403–2405.

[29] Georgakilas, V.; Pellarini, F.; Prato, M.; Guldi, D. M.; Melle-Franco, M.; Zerbetto, F. *Proc. Nat. Acad. Sci. U.S.A.* **2002**, *99*, 5075–5080.

[30] Tsunashima, S.; Noro, S.; Akutagawa, T.; Nakamura, T.; Kawasaki, H.; Toma, K. *Chem.–Eur. J.* **2008**, *14*, 8169–8176.

[31] Fujita, N.; Yamashita, T.; Asai, M.; Shinkai, S. *Angew. Chem.* **2005**, *117*, 1283–1287; *Angew. Chem. Int. Ed.* **2005**, *44*, 1257–1261.

[32] Schade, B.; Ludwig, K.; Böttcher, C.; Hartnagel, U.; Hirsch, A. *Angew. Chem. Int. Ed.* **2007**, *46*, 4393–4396.

[33] Zhou, S.; Burger, C.; Chu, B.; Sawamura, M.; Nagahama, N.; Toganoh, M.; Hackler, U. E.; Iosbe, H.; Nakamura, E. *Science* **2001**, *291*, 1944–1947.

[34] Brettreich, M.; Burghardt, S.; Böttcher, C.; Bayerl, T.; Bayerl, S.; Hirsch, A. *Angew. Chem. Int. Ed.* **2000**, *39*, 1845–1848.

[35] Partha, R.; Lackey, M.; Hirsch, A.; Casscells, S. W.; Conyers, J. L. *J. Nanobiotechnol.* **2007**, *5*, 1–11.

[36] Partha, R.; Mitchell, L. R.; Lyon, J. L.; Joshi, P. P.; Conyers, J. L. *ACS Nano* **2008**, *2*, 1950–1958.

[37] (a) Isobe, H.; Nakanishi, W.; Tomita, N.; Jinno, S.; Okayama, H.; Nakamura, E. *Mol. Pharm.* **2006**, *3*, 124–134. (b) Ying, Q.; Zhang, J.; Liang, D.; Nakanishi, W.; Isobe, H.; Nakamura, E.; Chu, B. *Langmuir* **2005**, *21*, 9824–9831. c) Nakamura, E.; Isobe, H.; Tomita, N.; Sawamura, M.; Jinno, S.; Okayama, H. *Angew. Chem., Int. Ed.* **2000**, *39*, 4254–4257.

[38] (a) Maeda-Mamiya, R.; Noiri, E.; Isobe, H.; Nakanishi, W.; Okamoto, K.; Doi, K.; Sugaya, T.; Izumi, T.; Homma, T.; Nakamura, E. *Proc. Natl. Acad. Sci. U.S.A.* **2010**, *107*, 5339–5344. (b) Isobe, H.; Nakanishi, W.; Tomita, N.; Jinno, S.; Okayama, H.; Nakamura, E. *Chem.–Asian J.* **2006**, *1–2*, 167–175.

Chapter 2. siRNA Delivery Using Water-Soluble Cationic Amino-Fullerene In Vitro

2.1. Introduction

Gene therapy has been attracted much attention as a potential technique for targeting genetic disorders as well as an alternative method to traditional chemotherapy used in treating cancer. As for the gene therapy DNA has been utilized due to their easy handling. However, there are still some problems remaining in the gene therapy using DNA, such as a canceration derived from non-specific insertion into genome. Thus, it is required the alternative tools for the gene therapy.

RNA interference (RNAi) has emerged since its discovery[1] as a powerful tool of gene silencing, which inhibits gene expression at the post-transcriptional level by the sequence-specific cleavage of specific mRNA. RNAi is mediated by small interfering RNA (siRNA), which is small non-coding RNA with the 21 to 23 nucleotide-length. However, siRNAs are rapidly degraded by nuclease under physiological environment, and are difficult to permeate through the hydrophobic cell membranes due to their high solubility in water. Therefore, it needs the carriers with highly stabilizing as well as effectively delivering siRNA into cells to achieve the siRNA-based gene therapy.[2]

Recently, our group has developed DNA delivery systems using water-soluble cationic amino-fullerene derivatives.[3, 4] The cationic amino-fullerenes can aggregate with plasmid DNA by electrostatic interaction and hydrophobic effect of fullerene to form submicrometer-sized globules. The more hydrophobic nature of fullerenes than alkyl chains in lipids appears to enable the amino-fullerenes to form stable fullerene-DNA complexes, which led to effective stabilization of oligonucleotides by nucleases and to deliver the DNA into cells with no cytotoxicity, especially tetra(piperazino)fullerene epoxide (TPFE) was achieved in vivo gene delivery without acute organ toxicity.

In this chapter, I will report effective stabilization and delivery of siRNA using TPFE without cytotoxicity.

2.2. Structural analysis of TPFE-oligonucleotide complexes

2.2.1 Characterization of TPFE in water

A structure of TPFE in water was characterized by dynamic light scattering (DLS) and scanning transmission electron microscopy (STEM). TPFE dissolved in acidic buffer (KCl-HCl, pH 2.0) as two major aggregated structures with diameters of 9.1 and 309 nm, respectively, determined by DLS (Figure 2-1a, black). After centrifugal separation at 15,000 × *g*, supernatant gave a single peak with an average diameter of 7.2 nm (Figure 2-1a, red). STEM image also showed the small particles with the average diameter of 5.4 nm (Figure 2-1b and c). Our group has already reported that the similar structure of amphiphilic fullerenes form ca. 8 nm aggregated structure, such as sugar-appended fullerene penta-adduct in water (8.3 nm by DLS)[5] and perfluorinated fullerene penta-adduct in fluorous solvent (8.1 nm by DLS).[6] Moreover, it is known that bare [60]fullerene forms the close-packed crystalline structure with a specific numbers of C_{60} molecules $(C_{60})n$ due to the unique structure and strong cohesive power of fullerene.[7] According to the results of these aggregated fullerene amphiphiles including TPFE and result of close-packed crystalline structure of C_{60}, I surmised that TPFE aligned the truncated icosahedral structure to form a micellar structure, whose size is calculated as 6.5 nm (Figure 2-1d). This micellar structure exposed the piperazine moieties to aqueous phase, so the micelle has the cationic surface. Therefore, it is expected that the cationic micelle aggregates with polyanionic siRNA.

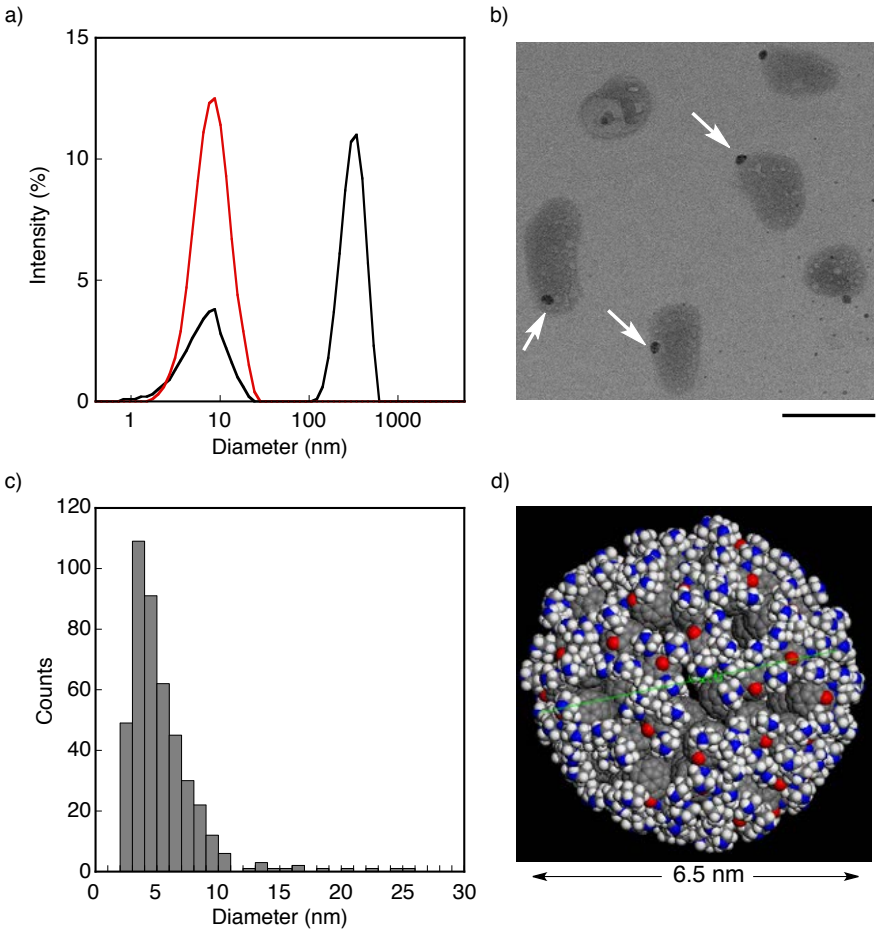

Figure 2-1. Size distributions of TPFE in acidic buffer. a) Size distribution of TPFE in water determined by DLS. Before and after centrifugal separation are shown as black and red, respectively. b) STEM image of TPFE on carbon film. Scale bar is 100 nm. White arrows indicate the aggregated TPFE. c) Histogram of TPFE aggregate determined by STEM. d) Model of TPFE micelle. The distance was calculated by Material Studio Software.

2.2.2 *Effective binding ability of TPFE with siRNA*

The ability of TPFE to bind siRNA was evaluated by gel electrophoresis (Figure 2-2). TPFE was mixed with GFP-targeted siRNA (siGFP) at various reagent-to-base pair ratio (*R*), which was calculated by dividing the nitrogen-to-phosphorous (N/P) ratio by two, from 1 to 50. TPFE-siRNA complexes and free siRNA were observed in bright field (BF) and UV images,

respectively. Free siRNAs were observed at the *R* value from 1 to 10. However, the free siRNA disappeared from the *R* value of 20. This result clearly indicates that TPFE completely bound siGFP at the *R* value of 20. The sizes of TPFE-siGFP complexes prepared at the *R* value from 1 to 50 were measured by DLS (Figure 2-2). Interestingly, the average diameters of the *R* values from 2 to 10 obtained significantly large aggregates (> 1 μm) with large amount of precipitates, whereas TPFE allowed to form submicrometer-sized globules after completion of binding with siRNA.

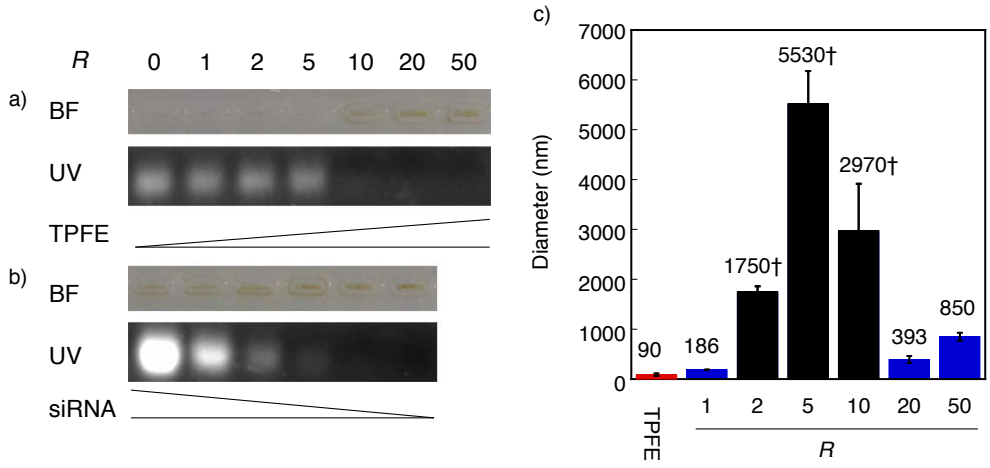

***Figure* 2-2.** Formation of TPFE-siRNA complexes. a), b) Upper and bottom figures are bright field (BF) and UV images, respectively, with different dose of TPFE (a) and siRNA (b). c) DLS analysis of TPFE-siRNA complexes. Numbers present in the figure are indicates the average diameters. † indicates the observation of precipitates.

Further characterization of TPFE-siRNA complex was carried out by atomic force microscopy (AFM) and STEM measurements (Figure 2-3, see also Figure 2-8 and Figure 2-9). Part of AFM image under ambient pressure and temperature on mica showed flower-like objects. The similar objects were also observed by SEM analysis. The sizes of objects were around 500 nm, which is good agreement with DLS data. These results suggest that the flower-like objects indicate TPFE-siRNA complexes. The size of siRNA is around 7 nm and

is as similar as that of TPFE micelle as I described above, so the both TPFE and siRNA work as molecular glue each other. TPFE and siRNA first form 10–50 nm particles, then further aggregates to form the submicrometer-sized particles. Thus, the ratio between TPFE and siRNA is critical for the formation of the submicrometer-sized objects.

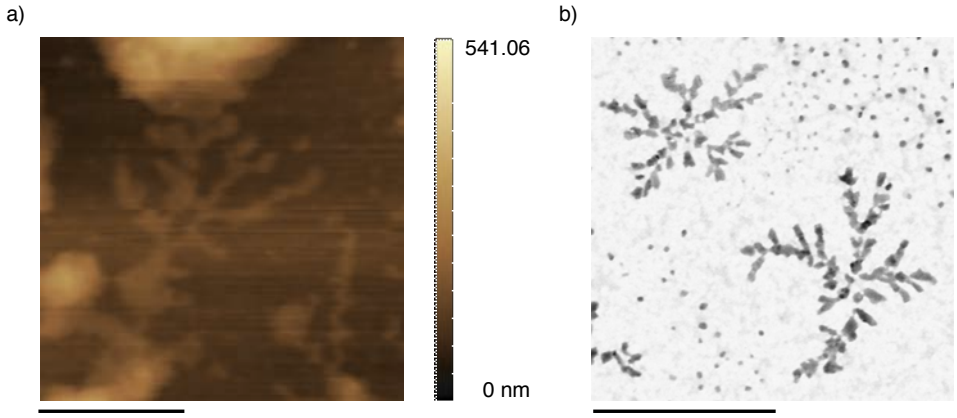

Figure 2-3. Microscopic images of TPFE-siRNA complex. a) AFM image on mica. Scale bar is 1 μm. b) SEM image on carbon film. Scale bar is 500 nm.

2.3. Stabilization of siRNA under physiological environment

The protection of siRNA from nuclease is critical issues for siRNA delivery. Stabilization of siRNA by TPFE was evaluated by agarose gel electrophoresis (Figure 2-4a).[8] TPFE-siGFP complex was incubated with 100 times diluted mouse serum for 15 min at 25 °C as a simulated physiological environment. siGFP in TPFE-siGFP complex was extracted by TRIzol reagent with a modified condition of manufactures' protocol (see 2.7 Experimental section). Free siGFP degraded about 40% in the presence of serum. On the other hand, siGFP extracted from TPFE-siGFP complex did not obtain a significant degradation, indicating that TPFE effectively protected siRNA from the nuclease. This result clearly suggests that the TPFE has a potential as the siRNA delivery vehicle.

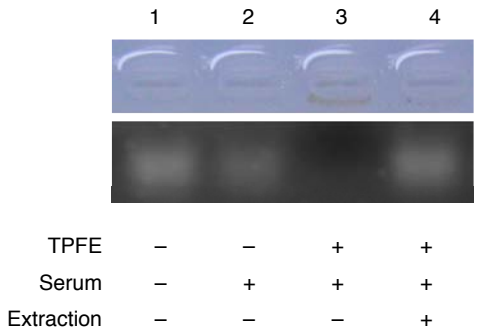

Figure 2-4. TPFE-siRNA complex under physiological condition. Agarose-gel electrophoresis for stabilization ability of siRNA. RNA was stained with ethidium bromide.

2.4. siRNA delivery efficiency of TPFE-siRNA complex in vitro

I found that TPFE completely bound with siRNA at the *R* value of 20, and allowed to form the submicrometer-sized globules. Then I studied the siRNA transfection efficiency of TPFE. The efficiency of TPFE-siRNA complexes as a carrier for siRNA delivery was determined in HEK293-GFP cells (genetically engineered HEK293 cells that express GFP) (Figure 2-5). TPFE-siGFP complexes were formed with siGFP or Stealth siGFP, which is chemically stabilized siRNA. HEK293-GFP cells were incubated with TPFE-siGFP complexes for 48 h. All experiments were carried out at a final concentration of siGFP (40 nM), and the concentration of TPFE was varied according to the *R* value. For comparison, parallel experiments were carried out using TPFE-siNEG complex with a scrambled siRNA (siNEG) as a negative control. As a positive control, the commercially available transfection reagent, Lipofectamine2000 was used. The transfection efficiency is expressed in % amount of GFP mRNA expression, and is normalized to the amount of house keeping gene expression (β-actin) present in the cells. The *R* value of 5, which based on previous our studies is the highest transfection efficiency showed as a DNA carrier,[4b] did not show significant transfection efficiency due to the low

loading amount of siRNA and formation of the large aggregates. However, the *R* value of 20 obtained the highest knockdown efficiency (61% for Stealth siGFP and 51% for siGFP), which is higher than that of Lipofectamine2000 (49% for Stealth siGFP and 35% for siGFP). Interestingly, the *R* value of 10 obtained no significant knockdown by TPFE-siGFP but 55% knockdown by TPFE-Stealth siGFP. This result may indicate that the loading amount of TPFE-siRNA (*R* = 10) is lower than that of TPFE-siRNA (*R* = 20), but the enough amount of Stealth siRNA was delivered into cells due to the stability of Stealth siRNA under the physiological condition.

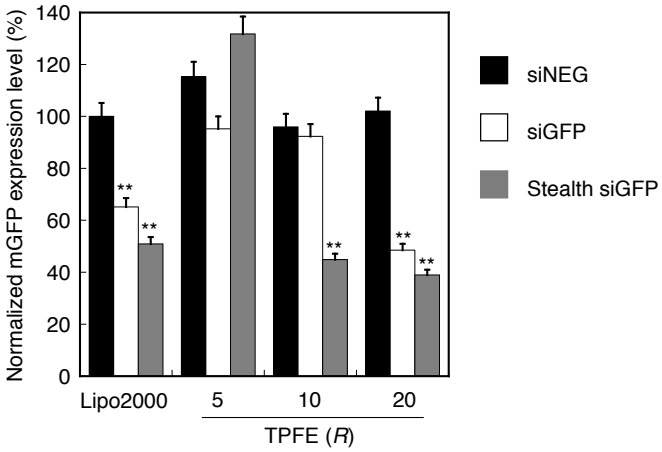

***Figure* 2-5.** siRNA delivery in vitro. Normalized expression level of mRNA was determined by qRT. siNEG (black), siGFP (white) and Stealth siGFP (gray) were shown. Lipo2000: Lipofectamine2000. Error bars are SEM ($N = 3$). ** $P < 0.001$ v.s. the expression level of mRNA of siNEG-treated cell lines.

2.5. Toxicity

Cytotoxicity is an inevitable issue for all of the delivery carriers at present, and lipid-based carriers are well known to have high cytotoxicity.[9,10] Previous report has been already revealed that TPFE-DNA complex has no or low cytotoxicity in vitro and in vivo.[4] In addition, cytotoxicity of tetraamino

fullerene derivative also revealed as no cytotoxicity.[11] However, as I mentioned above, TPFE-siRNA complex showed different complexation behavior compared with TPFE-DNA complexes. Then I studied the quantitative evaluation of cytotoxicity of TPFE-siRNA complexes using 3-(4,5-dimethylthiazol-2-yl)-2,5-diphenyl-tetrazolium bromide (MTT) assay.[12] MTT assay has been utilized for cytotoxicity measurement of various drugs including transfection agents. The principle of the assay is colorimetric detection of formazan dye at 455 nm, which was produced from tetrazolium salt, MTT by reductase in metabolic active cells. The resulting colored medium was quantified using a scanning multi-well spectrophotometer (ELISA reader).

TPFE-siRNA complexes were added to 293-GFP cells at various concentration with a ranging from 5.00 nM to 2.25 μM, and the cells were incubated at 35 °C with 5% of CO_2 for 48 h. After incubation, the stock solution of MTT in PBS was added and the cells were further incubated at 35 °C with 5% CO_2 for 4 h. After additional incubation, the solubilizing buffer (10% SDS in 0.01 M HCl solution) to solubilize the cells was added into each well, and then the plate was allowed to stand for overnight in the incubation chamber. The absorbance of the each well at 455 nm was measured by ELISA reader, and absorbance at 690 nm was used as a reference wavelength. The results were expressed as the relative value (%) of the control cells, which were incubated parallel with 50 μL of PBS (Figure 2-6), and plots were fitted by a dose-response logistic model;

$$f(x) = \frac{(b-a)}{1+(x/c)^d} = \frac{100}{1+(x/c)^d}$$

where a, b, c, and d indicate minimum value (0%), maximum value (100%), inhibitory concentration (IC_{50}, μM) and gradient of a fitting curve, respectively. Fitting curves of siGFP and siNEG were;

$$f(x) = \frac{100}{1+(x/706)^{2.13}}, R^2 = 0.939$$

$$f(x) = \frac{100}{1 + (x/689)^{1.72}}, R^2 = 0.892$$

respectively. According to the fitting curves the IC_{50} of TPFE-siGFP and TPFE-siNEG were determined as 710 and 690 μM, respectively. By comparison of the dose of in vitro transfection (40 nM), it can be said that TPFE-siRNA complexes do not have any cytotoxicity.

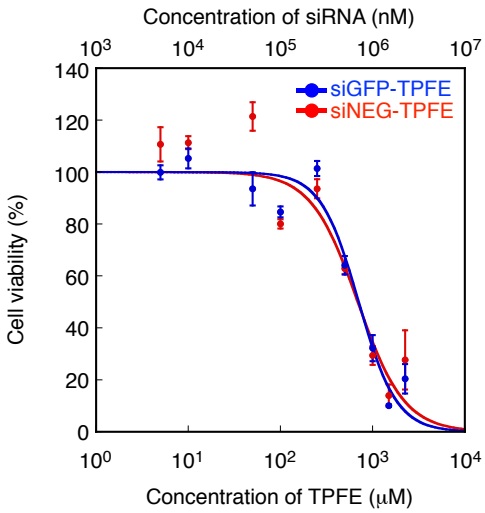

Figure 2-6. Cell viability assay. All data show the mean value together with SEM (N = 3). Fitting curves indicate the dose-response logistic model using KaleidaGraph software.

2.6. Conclusion

In summary, I have demonstrated that TPFE effectively delivers siRNA with no acute organ toxicity. TPFE can form submicrometer-sized globules with siRNA and deliver siRNA more effectively into cells than a conventional cationic liposome-based system in vitro. In addition, TPFE effectively stabilizes and protects siRNA from nucleases under the physiological environment. This study suggests the potential ability of TPFE for the in vivo siRNA delivery

2.7. Experimental section

General.

Distilled water was further deionized with Millipore Milli-Q. The dynamic laser light scattering (DLS) study was carried out on a Malvern Zetasizer Nano ZS machine. AFM measurement was conducted on a Shimadzu SPM-9700 with a silicon cantilever (Olympus, OMCL-AC160TS). Quantitative real-time reverse transcriptase-polymerase chain reaction (qRT-PCR) analyses were performed by ABI7000 Sequence Detection System (Applied Biosystems).

Materials.

Unless otherwise noted, materials were purchased from Tokyo Kasei Co., Aldrich Inc., and other commercial suppliers and used after appropriate purification before use. Anhydrous ethereal solvents (stabilizer-free) were purchased from WAKO Pure Chemical and purified by a solvent purification system (GlassContour)[13] equipped with columns of activated alumina and supported copper catalyst (Q-5) prior to use. All other solvents were purified by distillation and stored over molecular sieves 4Å. TPFE was synthesized as followed the reported procedure.[4] siRNA targeting green fluorescent protein (siGFP) (sense strand, 5′-CGGCAAGCUGACCCUGAAGUU-3′ and antisense strand, 5′-UGAACUUCUGGGUCUGCUUGC-3′), and scrambled siRNA as a negative control (siNEG) (sense strand, 5′-CGGCAAGUCUCCCAAGGAGUU-3′ and antisense strand, 5′-UGAACUCCUUGGGAGACUUGC-3′) were purchased from Hokkaido System Science Co., Ltd. (Hokkaido, Japan). Stealth™ RNAi GFP Receptor Control was purchased from Invitrogen. PCR primers were purchased from Invitrogen. Mouse serum is collected from C57BL/6 mice.

Cell line.

EGFP overexpressed human embryonic kidney cell line (293-GFP) was purchased from GenTarget Inc. (San Diego, CA) and maintained in D-MEM with 10% FBS.

Complex formation between siRNA and TPFE.

To determine the formation of oligonucleotide-TPFE complexes in various *R* values, DLS and agarose gel electrophoresis were used. The samples were prepared from stock solutions of siRNA and 2 mM TPFE solution. For DLS analysis the solution was diluted until 100 or 500 μL of final volume. For electrophoresis oligonucleotides were detected *via* electrophoresis on a 4% agarose gel and stained with ethidium bromide. Before loading siRNA, siRNA samples were denatured using DynaMarker RNA Eazy Measurement N (BioDynamics Laboratory) according to the manufactures' protocol. Gels were scanned with a charge-coupled device (CCD) camera systems (LAS-4000mini; Fuji Photo Film), and intensities of siRNA were measured on a DocuCentre Color 500 cp (Fuji-Xerox).

Determination of stabilization ability.

For evaluation of RNase resistance of siRNA-TPFE complex under the simulated biological environment, the siGFP was incubated with mouse serum. First, 1.0 μg of siRNA with or without 2.0 mM aqueous TPFE solution was incubated with serum at room temperature for 15 min. The reaction was quenched by addition of formaldehyde dye of DynaMarker RNA Eazy Measurement N (BioDynamics Laboratory), and the samples were heated up to 65 °C for 15 min.

As the case of re-extracted siRNA from siRNA-TPFE complex, the 10 μg of siGFP was used and the reaction was quenched by addition of 1 mL of

TRIzol® Reagent (invitrogen), and siGFP was extracted as followed optimized protocol. A siGFP sample was dissolved in 1.0 mL of TRIzol reagent, and incubated at 72 °C to denature the duplex for 5 min. 0.20 mL of Chloroform per 1.0 mL of TRIzol® reagent was added to the mixture, and mixed well by shaking. After incubation for additional 5 min at 72 °C, the mixture was centrifuged at 12,000 × *g* for 15 min at 4 °C. 0.40 mL of aqueous phase per 1.0 mL of initial TRIzol® reagent was transferred to a fresh tube. To the aqueous phase 1.0 mL of 2-propanol per 1.0 mL of TRIzol® reagent was added. After incubation at room temperature for 10 min, the mixture was centrifuged at 12,000 × *g* for 10 min at 4 °C to precipitate the siGFP. After removal of the supernatant, 1.0 mL of 80% ethanol per 1.0 mL of initial TRIzol reagent was added to the tube to wash the siGFP. After mixing the sample by voltexing, the sample was centrifuged at 7,500 × *g* for 5 min at 4 °C. After removal of the supernatant, the precipitate was briefly dried and dissolved in RNase-free water, and incubated at 55 °C for 5 min.The isolated siRNA was immediately denatured with formaldhyde dye of DynaMarker RNA Eazy Measurement N.

RNAs were detected *via* electrophoresis on a 4% agarose gel and stained with ethidium bromide. Gels were scanned with a charge-coupled device (CCD) camera systems (LAS-4000mini; Fuji Photo Film), and intensities of siRNA were measured on a DocuCentre Color 500 cp (Fuji-Xerox).

DLS analysis.

DLS measurement was performed on a Malvern Zetasizer Nano ZS equipped with an He-Ne laser operating at 4 mW power and 633 nm wavelength, and a computer-controlled correlator, at a 173° accumulation angle. Measurement was carried out at room temperature in a polystyrene or glass cuvette. The data were processed using dispersion technology software version 4.10 to give Z-average particle size and polydispersity index (PDI)

value by cumulant analysis, and particle size distribution by CONTIN analysis.[14]

STEM measurement.

STEM measurement of Figure 2-7 was conducted on a JEOL JEM-2100F at 294 K with a spherical aberration coefficient Cs = 1.0 nm at an acceleration voltage of 200 kV under reduced pressure of 1.0×10^{-5} Pa in the sample column. The current density is ca. 0.5 pA·cm^{-2}. The imaging instrument used was an ultrascan charge-coupled device (CCD) camera (512 × 512 pixels). 50 μM of TPFE (5 μL) was deposited on a transmission electron microscopy (TEM) copper mesh coated with carbon film (Super Ultra High Resoluton Carbon film, thickness < 6 nm, Oken Shoji Co., Ltd.), then dried under reduced pressure (4×10^{-2} Pa) at room temperature for 18 h.

STEM measurement of Figure 2-8 was conducted on a Magellan 400L at 298 K with a spherical aberration coefficient Cs = 1.0 nm at an acceleration voltage of 30 kV under reduced pressure at 5.0×10^{-5} Pa in the sample column. The current density is ca. 0.5 pA·cm^{-2}. The imaging instrument used was an ultrascan CCD camera (1024 × 884 pixels). 50 μM of TPFE (5 μL) was deposited on a transmission electron microscopy (TEM) copper mesh coated with carbon film (Super Ultra High Resolution Carbon film, thickness < 6 nm, Oken Shoji Co., Ltd.), then dried under reduced pressure (4×10^{-2} Pa) at room temperature for 3 h.

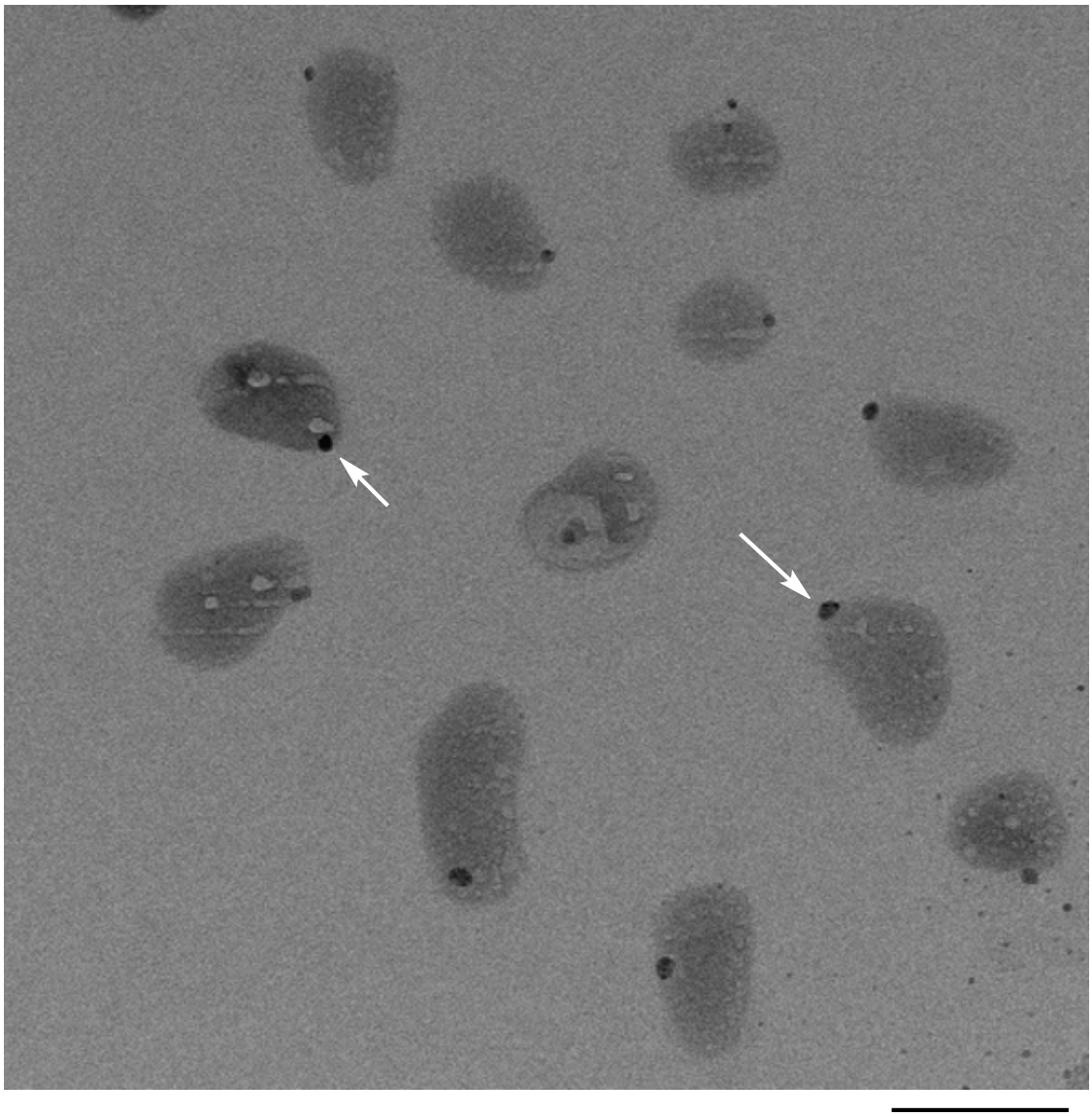

Figure 2-7. STEM image of TPFE on carbon film. Scale bar is 100 nm. White arrows indicate TPFE micelles.

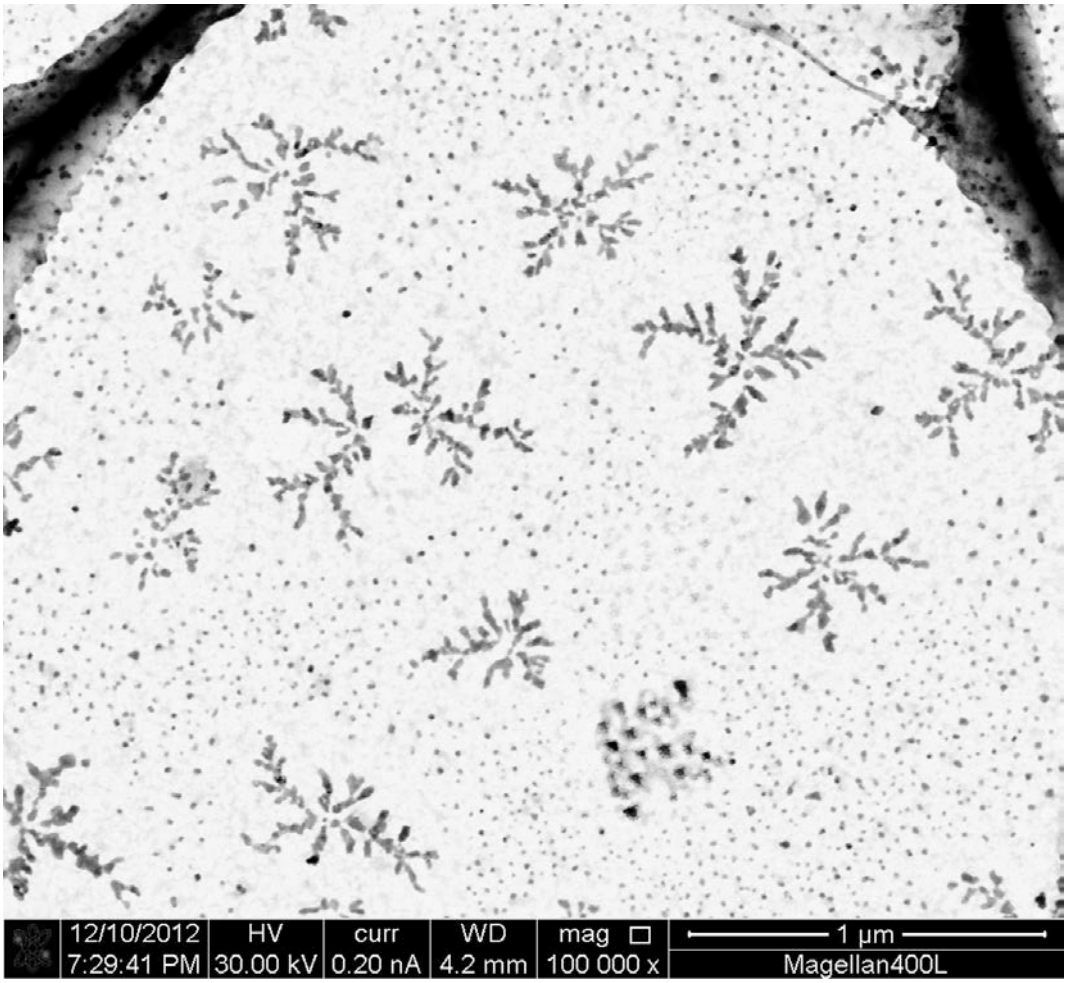

Figure 2-8. STEM image of TPFE-siRNA complex.

AFM measurement.

AFM measurement was conducted on a Shimadzu SPM-9700 with a silicon cantilever (Olympus, OMCL-AC160TS). Sample was deposited on a mica substrate in aliquot of TPFE-siRNA solution under air. After drying the sample under reduced pressure, the AFM images were obtained with AM mode measurement.

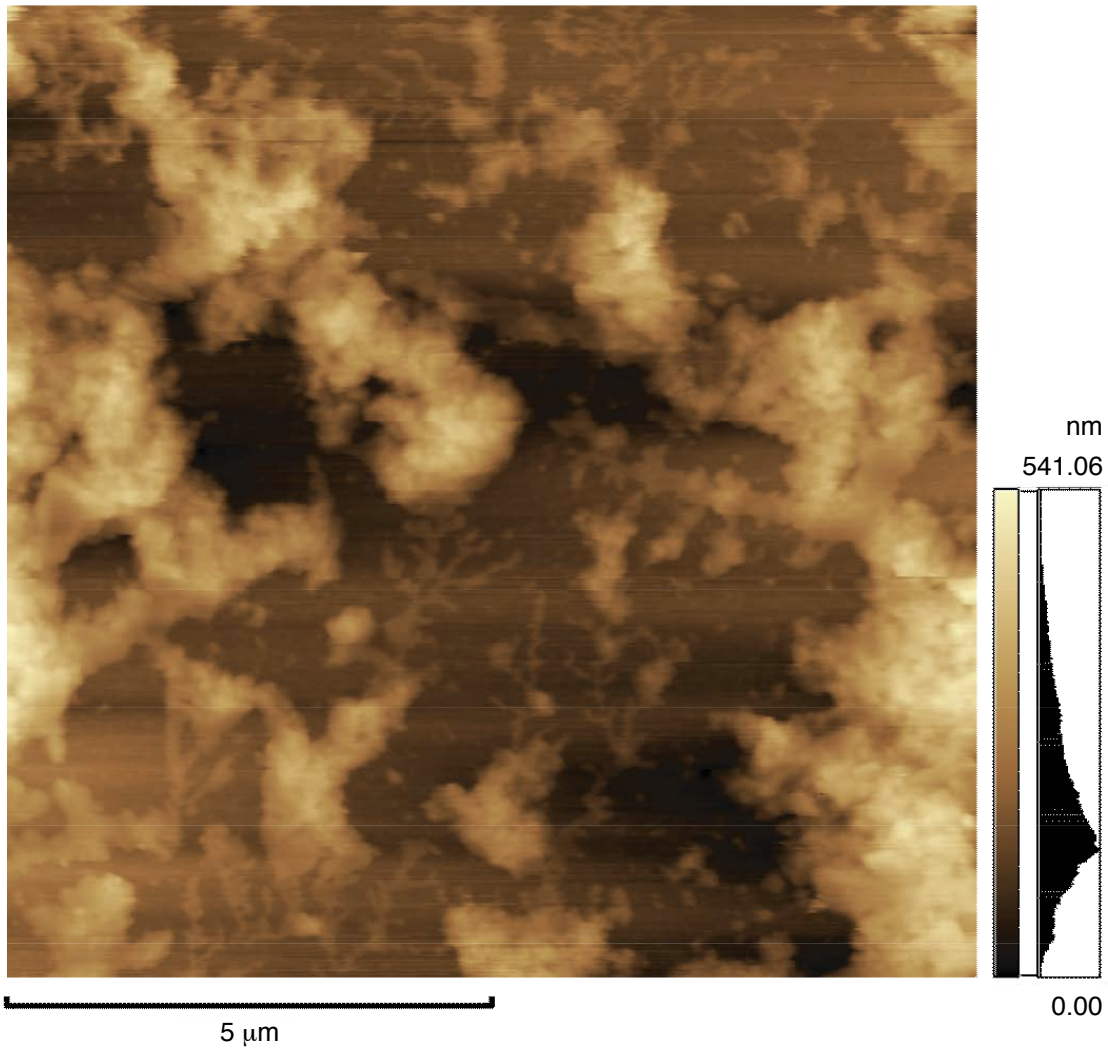

Figure 2-9. An AMF image of TPFE-siRNA complex.

siRNA transfection assay in vitro.

293-GFP was purchased from GenTarget Inc (San Diego, CA) and maintained in D-MEM with 10% FBS. 24 h before transfection, endothelial cells were lifted with 0.05% trypsin-0.53 mM EDTA (Gibco BRL, Gaithersburg, USA), washed, and then re-suspended in 12-well or 24-well plate. siRNA and TPFE was mixed, and diluted serum-free medium, Opti-MEM (Invitrogen). Lipofectamine® 2000 was used as a positive control according to the manufactures' protocol. Just before treatment, cell medium was replaced to the serum-free medium. After incubation for 48 h, cell lysate was removed, and then TRIzol® reagent was added into each well. Then samples were transferred into fresh tubes and stored at –80 °C until use for qRT-PCR.

Determination of RNAi activity.

Total RNAs were extracted from each cells and tissues using TRIzol® reagent (Invitrogen) according to the manufactures' protocol. The extracted total RNAs were treated with DNase to remove the genomic DNAs by using DNA-*free*™ Kit (Ambion) according to the manufactures' protocol. 1 μg of isolated total RNAs were transcribed into cDNA using High Capacity cDNA Reverse Transcription Kit (Applied Biosystems) and Oligo-dT primer according to the manufactures' protocol. Finally, the expression level of target gene and/or housekeeping gene in the cDNA was quantified by quantitative real-time RT-PCR using *Power* SYBR® Green PCR Master Mix (Applied Biosystems) according to the manufactures' protocol.

In briefly, chloroform was added into homogenized cells or tissues in TRIzol® reagent in the flesh tube. The sample was mixed well and incubated at room temperature for several minutes. After centrifugation, the aqueous phase was transferred to a flesh tube. Total RNA was precipitated by adding 2-propanol. After centrifugation and removal of supernatant, the total RNA

was washed with 75% aqueous solution of ethanol. After centrifugation, the supernatant was removed, and briefly dried. The extracted total RNA was treated with DNase. After incubation for 30 min at 37 °C, DNase was inactivated and transferred the RNA aqueous solution. 1 μg of total RNA was transcribed into cDNA. Reverse transcription reaction was performed at 25 °C for 10 min, at 37 °C for 2 h and 85 °C for 5 sec. The cDNAs were stored at –30 °C until use.

qRT-PCR was performed using *Power* SYBR® Green PCR Master Mix (Applied Biosystems) and ABI7000 Sequence Detection System with 7000 System SDS Software ver. 1.2 (Applied Biosystems). Data are presented as the fold difference in GFP expression normalized to the housekeeping gene *β*-Actin as the endogenous reference, and relative to the negative control cells. Primers used in qRT-PCR for GFP, TLR4 and *β*-Actin are:

GFP-forward	5′-GACGTAAACGGCCACAAGTT-3′
GFP-reverse	5′-GGTCTTGTAGTTGCCGTCGT-3′
β-Actin-forward	5′-CGCACCACTGGCATTGTCAT-3′
β-Actin-reverse	5′- TTCTCCTTGATGTCACGCAC-3′

PCR parameters consisted of 2 min at 50 °C, 10 min at 95 °C, followed by 40 cycles of PCR for GFP at 95 °C for 15 sec and at 60 °C for 1 min, or by 40 cycles of PCR for *β*-actin at 95 °C for 15 sec and at 54 °C for 1 min.

Cytotoxicity assay.

The MTT assay is designed to measure the cytotoxicity. GFP overexpressed cells were harvested, collected, and resuspended in 100 μL of D-MEM at a concentration of 2×10^4 cells per 1 well over a 96-well plate before the siRNA transfection. TPFE-siRNA complexes were diluted to a series of concentrations in 50 μL of PBS to prepare test solutions. Just before addition of the test solutions, the medium was removed and 50 μL of fresh medium was

added. The test solutions were added into the wells in the 96-well plate, and the cells were incubated for 48 h at 37 °C in a humidified atmosphere with 5 % of CO_2. At the end of cell culture, the number of viable cells in each wells of the wells was determined by a quantitative colorimetric staining assay using 3-(4,5-dimethylthiazol-2-yl)-2,5-diphenyl-tetrazolium bromide (MTT) (Cell Proliferation Kit I (MTT), Roche) as followed the manufactured protocol. Briefly, after incubation for 48 h, 4 μL of MTT labeling reagent was added into the wells in the 96-well plate, and the cells were incubated for 4 h. After incubation, 100 μL of solubilizing solution was added to the wells in 96-well plate, and then incubated overnight at 37 °C in a humidified atmosphere with 5 % of CO_2. Absorbance at 550 nm of each wells was measured, and absorbance at 690 nm was used as a reference wavelength. The results were expressed as the relative value (%) of the control cells, which were incubated parallel with 50 μL of PBS.

The inhibitory concentrations (IC_{50}, μM) were defined as concentration required for inhibiting 50% of the cell growth. Each data point on the curve in Figure 2-6 is indicated as a median value and its error bar based on three parallel experiments. IC_{50} values and its standard errors were determined by the Dose-Response Logistic Model using software Kaleidagraph;

$$f(x) = \frac{(b-a)}{1+(x/c)^d} = \frac{100}{1+(x/c)^d}$$

where a, b, c, and d indicate minimum value (0%), maximum value (100%), IC_{50} value and gradient of a fitting curve, respectively.

Statistical analysis.

Differences among the experimental groups were detected using Student's t-test. Values are expressed as means ±SEM; $p < 0.05$ was considered significant.

References

[1] Fire, A.; Xu, S.; Montgomery, M. K.; Kostas, S. A.; Driver, S. E.; Mello, C. C. *Nature* **1998**, *391*, 806–811.

[2] Whitehead, K. A.; Langer, R.; Anderson, D. G. *Nat. Rev. Drug Discov.* **2009**, 8, 129–138.

[3] (a) Isobe, H.; Nakanishi, W.; Tomita, N.; Jinno, S.; Okayama, H.; Nakamura, E. *Mol. Pharm.* **2006**, *3*, 124–134. (b) Ying, Q.; Zhang, J.; Liang, D.; Nakanishi, W.; Isobe, H.; Nakamura, E.; Chu, B. *Langmuir* **2005**, *21*, 9824–9831. c) Nakamura, E.; Isobe, H.; Tomita, N.; Sawamura, M.; Jinno, S.; Okayama, H. *Angew. Chem. Int. Ed.* **2000**, *39*, 4254–4257.

[4] (a) Maeda-Mamiya, R.; Noiri, E.; Isobe, H.; Nakanishi, W.; Okamoto, K.; Doi, K.; Sugaya, T.; Izumi, T.; Homma, T.; Nakamura, E. *Proc. Natl. Acad. Sci. U.S.A.* **2010**, *107*, 5339–5344. (b) Isobe, H.; Nakanishi, W.; Tomita, N.; Jinno, S.; Okayama, H.; Nakamura, E. *Chem.–Asian J.* **2006**, *1–2*, 167–175.

[5] Isobe, H.; Cho, K.; Solin, N.; Wertz, D. B.; Seeberger, P. H.; Nakamura, E. *Org. Lett.* **2007**, *9*, 4611–4614.

[6] Homma, T.; Harano, K.; Isobe, H.; Nakamura, E. *Angew. Chem. Int. Ed.* **2010**, *49*, 1665–1668.

[7] Branz, W.; Malinowski, N.; Schaber, H.; Martin, T. P. *Chem. Phys. Lett.* **2000**, *328*, 245–250.

[8] Okamoto, K.; Iwasaki, N.; Nishimura, C.; Doi, K.; Noiri, E. et al. *Am. J. Human Genet.* **2010**, *86*, 54–64.

[9] (a) Lv, H.; Zhang, S.; Wang, B.; Cui, S.; Yan, J. *J. Control. Release* **2006**, *114*, 100–109. (b) Dass, C. R. *J. Mol. Med.* **2004**, *82*, 579–591.

[10] Dokka, S.; Tokedo, D.; Shi, X.; Castranova, V.; Yojanasakul, Y. *Pharm. Res.* **2000**, *17*, 521–525.

[11] Mizuno, K.; Zhiyentayev, T.; Huang, L.; Khalil, S.; Nasim, F.; Tegos, G. P.; Gali, H.; Jahnke, A.; Wharton, T.; Hamblin, M. R. *J. Nanomed. Nanotechnol.* **2011**, *2*, 2–8.

[12] (a) Slater, T. F.; Sawyer, B.; Strauli, A. *Biochem. Biophys. Acta* **1963**, *77*,

383–393. (b) Vistica, D. T.; Skehan, P.; Scudiero, D.; Monks, A.; Pittman, A.; Boyd, M. R. *Cancer Res.* **1991**, *51*, 2515–2520.

[13] Pangborn, A. B.; Giardello, M. A.; Grubbs, R. H.; Rosen, R. K.; Timmers, F. J. *Organometallics* **1996**, *15*, 1518–1520.

[14] (a) Provencher, S. W. *Biophys. J.* **1976**, *16*, 27–41. (b) Provencher, S. W. *Comp. Phys. Comm.* **1982**, *27*, 213–227.

Chapter 3. Lung-Specific siRNA Delivery via Agglutination-Induced Lung Accumulation Using a Water-Soluble Cationic Amino-Fullerene

3.1. Introduction

RNA interference (RNAi) has emerged since its discovery[1] as a powerful tool of gene silencing, which inhibits gene expression at the post-transcriptional level by the sequence-specific cleavage of specific mRNA. RNAi is mediated by small interfering RNA (siRNA), which is small non-coding RNA with the 21 to 23 nucleotide-length. However, siRNAs are rapidly degraded by nuclease under physiological environment, and are difficult to permeate through the hydrophobic cell membranes due to their high solubility in water. Therefore, it is required the carriers with highly stabilizing as well as effectively delivering siRNA into cells.[2] Moreover, the organ-specific delivery is also necessary for treating tissue-specific diseases.

Lung diseases are the most common medical conditions, and afflict people worldwide. However, there are limited successes of lung-specific delivery systems. Two major strategies of the administration for treating lung diseases are pulmonary inhalation and microspheres. The inhalation is that the drugs and carriers are applied to alveolar surface. The drugs must first internalize into the protective mucus layer and then into the epithelial cell layer to deliver the lung tissues. Therefore, the lung-specific delivery by the inhalation is generally an inefficient pathway for the high administration into the lung. Moreover the inhalation often induces the lung fibrosis.[3] On the other hand, microspheres, with the sizes ranging from 5 to 15 μm, have known to be able to accumulate in the alveolar capillaries barriers and were taken up to the alveolar macrophages. However, particles with its diameter > 5 μm may stack in the lung capillary and lead to the chronic obstructive pulmonary emphysema,[4] and arterial embolism after intravenous accumulation.[5] In addition, from the viewpoint of drug delivery systems, the particles with the sizes > 5 μm is difficult to penetrate the cell membranes. Therefore, it is

necessary of the efficient lung-specific delivery systems to overcome these drawbacks. Shim et al. have reported the lung specific delivery of an anticancer drug.[6] The mean diameter of polymer-based carriers dramatically increased from 200–300 nm to several micrometers by addition of mouse plasma as a function of the surface charges. These significant changes of size to the several micrometers led to the accumulation of the lung because of the lung capillary, which is the narrowest capillary in the whole body.

Recently, our group has developed DNA delivery systems using water-soluble cationic amino-fullerene derivatives.[7,8] The cationic amino-fullerenes can aggregate with plasmid DNA by electrostatic interaction and hydrophobic effect of fullerene to form submicrometer-sized globules. The more hydrophobic nature of fullerenes than alkyl chains in lipids appears to enable the amino-fullerenes to form stable fullerene-DNA complexes, which led to effective stabilization of oligonucleotides by nucleases and to deliver the DNA into cells with no cytotoxicity, especially tetra(piperazino)fullerene epoxide (TPFE) was achieved in vivo gene delivery without acute organ toxicity. In addition, the length of siRNA (~ 7 nm) is much shorter than that of plasmid DNA. Therefore, not only TPFE but also siRNA work as a kind of molecular glues each other by the electrostatic interactions. It is expected that TPFE can deliver siRNA lung-specifically as following pathways (Figure 3-1): (1) TPFE aggregates with siRNA to form a submicrometer-sized complex, (2) the TPFE-siRNA complex further agglutinates with plasma proteins in bloodstream to form a large particle (> 1 μm), (3) the large particle stacks and remains in the narrow lung capillary, (4) TPFE-siRNA complex releases from the large particle to deliver the lung cells selectively. In this study, I developed a lung-specific siRNA delivery system using TPFE. The efficiency of siRNA delivery in vitro was examined by adjusting of TPFE-to-siRNA ratio. Lung selective delivery and its therapeutic application were also evaluated.

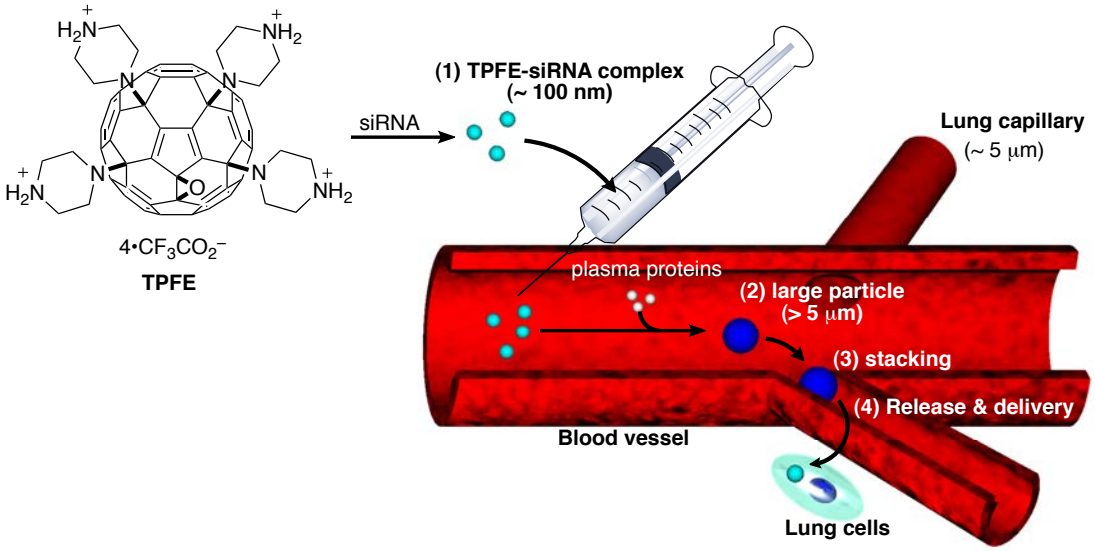

Figure 3-1. Schematic illustration of lung specific siRNA delivery using TPFE.

3.2. Size increase of TPFE-siRNA under physiological environment

I first evaluated the sizes of TPFE-siGFP complexes in water and serum for the lung-specific delivery (Figure 2-4). As described in Chapter 2, the TPFE and siRNA spontaneously formed the submicrometer globules determined, which is suitable for the cellular uptake. The TPFE-siGFP complexes were stable in water for 6 h not to change their sizes. On the other hand, the average diameter of TPFE-siRNA complexes significantly increased from ~400 nm to ~5 μm, and then precipitates were observed after 1 h. These results strongly suggest that the TPFE-siRNA rapidly aggregates with serum proteins in bloodstream, and immediately accumulates in the narrow lung capillaries.

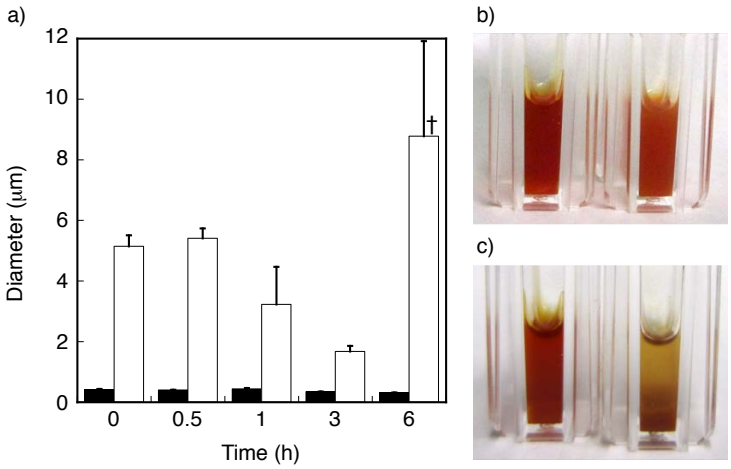

Figure 3-2. TPFE-siRNA complex under physiological condition. a) Time-dependent DLS analysis of TPFE-siGFP in the absence (black) and in the presence (white) of mouse serum. † indicates the observation of precipitates. b), c) Photographs of TPFE-siGFP solutions at 0 h (b) and 6 h (c), respectively.

3.3. Lung-specific delivery of TPFE-siRNA complex

3.3.1 In vivo biodistribution of TPFE-siRNA complexes

The in vivo biodistribution of TPFE-siRNA complexes were evaluated by the knockdown of GFP mRNA expression. TPFE-siGFP complex with 100 μg of siRNA was injected into GFP-expressed C57BL/6 mice, and maintained for 24 and 48 h. The mice were sacrificed and collected perfused tissue specimens from brain, heart, lung, liver, kidney, spleen and peritoneum. The transfection efficiency was expressed the same as in vitro experiments. TPFE-siNEG was used as a negative control. The result clearly showed that lung specifically showed significant knockdown efficiency at 24 h after transfection (62%). However, no significant knockdown was observed in all tissues at 48 h ($P > 0.05$).

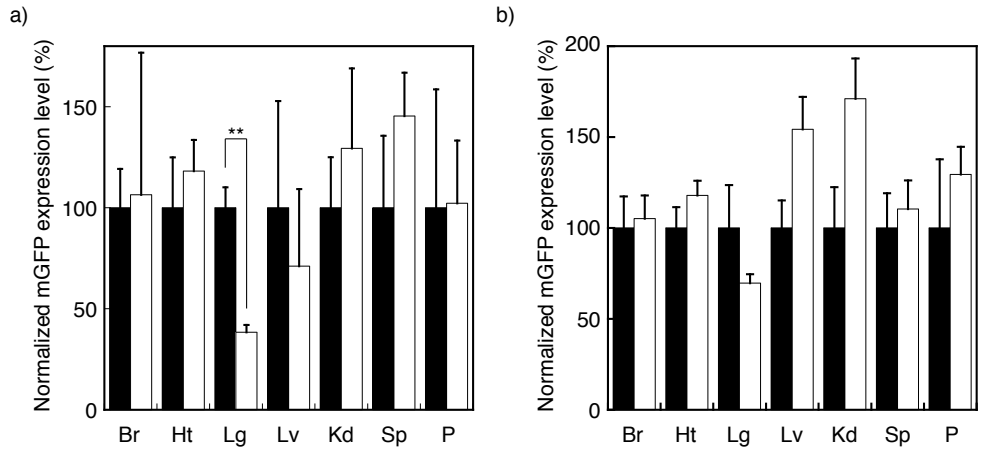

Figure 3-3. siRNA delivery in vivo. siRNA delivery at 24 (a) and 48 h (b) after post-injection. Black and white bars indicate siNEG and siGFP, respectively. Error bars are SEM. ** $P < 0.005$ versus siNEG groups. Abbreviations: Br, brain; Ht, heart; Lg, lung; Lv, liver; Kd, kidney; Sp, spleen; P, peritoneum.

The accumulated TPFE-siRNA complexes can be clearly observed by optical microscopy as a brownish-orange colored region without any specific staining (Figure 3-4, see also Experimental section).

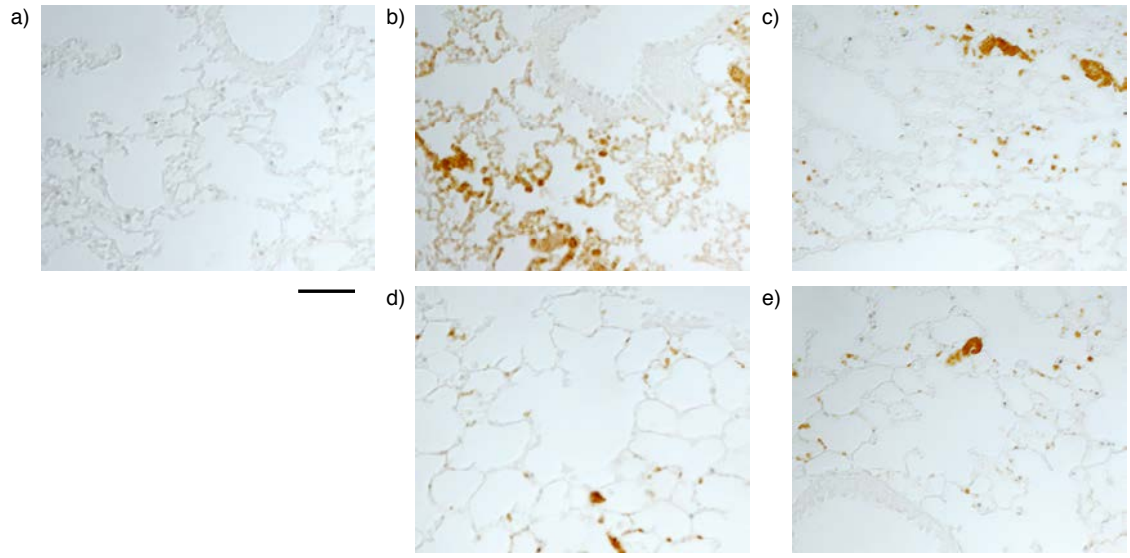

Figure 3-4. Accumulation of TPFE-siRNA complexes in lung sections. Histological appearance of TPFE in mouse lungs sacrificed at 15 min (b), 3 (a) and (c), 12 (d), and 24 h (e) after saline (a) or TPFE-siRNA complexes (b)–(e) injections. Brownish-orange colored area indicates the color of TPFE. Scale bar is 200 μm. Original maginification used, × 20.

Therefore, the accumulation behavior was evaluated by the lung histology stained with hematoxyline and eosin (H&E) (Figure 3-5, see also Experimental section). TPFE-siGFP complex was injected intravenously into mice, and then lung specimens were collected for the lung histology at the time of sacrifice (15 min, 3, 12, and 24 h). TPFE first distributed in lung capillary after injection, and then TPFE-siRNA complexes rapidly internalized into cells within 3 h. After that TPFE was gradually distributed in lung tissues and cells. The mechanism of cross-cellular transfer of TPFE is not clear, but one possible mechanism is cell-released microvesicles known as an intercellular communication, by which other carbon cluster-based carrier, carbon nanotube distributed between the cells.[9]

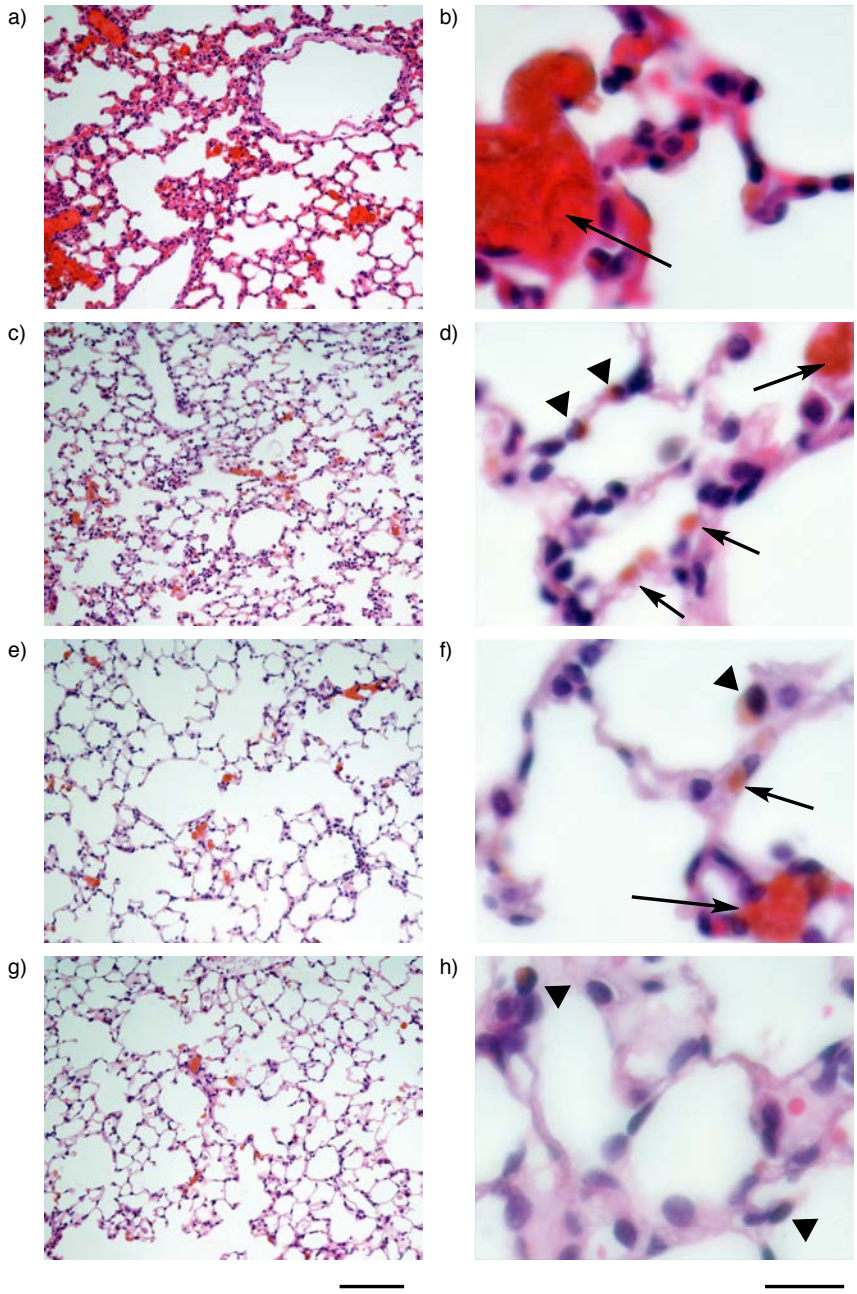

Figure 3-5. Accumulation of TPFE-siRNA complexes in lung capillaries and cells. a)–f) Histological appearance of TPFE in mouse lungs stained with H&E that was sacrificed at 15 min (a) and (b), 3 (c) and (d), 12 (e) and (f), and 24 h (g) and (h) after TPFE-siRNA injection. Brownish-orange colored area indicates the color of TPFE. Arrows and arrowheads indicate the lung capillaries and cells, where TPFE localized, respectively. Original magnification used and scale bars: (a), (c), (e) and (g), × 20, 100 μm; (b), (d), (f) and (h), × 60, 20 μm.

To examine the releasing rate of siRNA in the lung cells, I also investigated the time-dependent relationship between the accumulation in lung and the knockdown efficiency. Time-dependent accumulation of TPFE-siRNA complex in lung was measured by the area size of the orange colored regions from the lung histology shown in Figure 3-4 calculated by ImageJ software (Figure 3-6, red). The highest accumulation was obtained at 15 min, and then TPFE rapidly decreased along with cellular uptakes, may due to the release of small TPFE-siRNA complexes from the TPFE-siRNA-plasma protein aggregates. Finally, the accumulation of TPFE-siRNA complexes gradually decreased, suggesting that TPFE cleared from the lung cells. In addition, the time-dependent knockdown efficiency was also investigated (Figure 3-6, blue). I observed the significant knockdown of the gene expression only at 24 h after the post-injection. It is known that it takes RNAi pathway 12–24 h, which indicates that TPFE-siRNA rapidly internalized into lung cells within 3 h, and then siRNA was immediately released from TPFE-siRNA complexes by means of neutralization of the secondary amine moieties on TPFE by acylation (or any equivalent reaction) in the cytoplasm and hence loss of RNA-binding ability. The released siRNA then cleaved target mRNA by RNAi, and remaining TPFE was cleared from the lung cells and tissues. These results clearly suggest that the TPFE can be utilized for the rapid siRNA delivery for lung diseases.

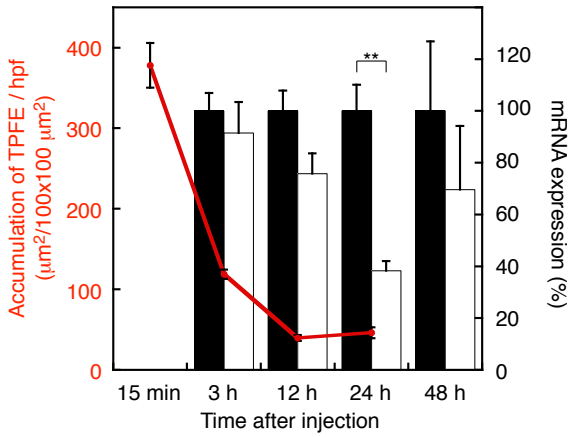

Figure 3-6. Time-dependent TPFE accumulation from histology and RNAi activity from mRNA. Red line shows the accumulation of TPFE in lung per high power field (hpf). Black and white bars indicate the normalized expression level of EGFP mRNA with injection of siNEG and siGFP, respectively. Error bars are SEM. ** $P < 0.005$ v.s. RNAi activity of siNEG-injected mice.

3.3.2 *Tissue selectivity between siRNA and plasmid DNA*

Tissue-selectivity of siRNA delivery is different from previous reports of TPFE-based DNA delivery system in vivo.[4a] TPFE-siRNA complexes effectively accumulated in lung. However, TPFE delivered DNA more effectively into liver and spleen than Lipofectin, which is a commercially available lipid-based DNA transfection agent, whereas the efficiency in lung was lower than that of Lipofectin. This difference comes from the different behavior of the size-changes of TPFE-oligonucleotides in serum. The size of TPFE-DNA complexes did not change for 2 h by addition of serum. On the other hand, the size of TPFE-siRNA complexes significantly increased to ~ 5 μm just after addition of serum. The structure of TPFE-siRNA complex would significantly differ from that of TPFE-DNA complex because of the difference of size between the plasmid DNA (~ 6 kbp, e.g., 4.4 kbp plasmid DNA forms 300–520 nm)[10] and the siRNA (21 bp, ~ 7 nm). The plasmid DNA is much larger than TPFE micelle in acidic buffer (~ 7 nm). It is thought that one DNA covered with

TPFE micelle to form very stable 100 nm globules. On the other hand, as I described above, siRNA is the same as the TPFE micelle, so TPFE and siRNA first form ~ 10 nm aggregates, and then further aggregation takes place to form submicrometer-sized particles. Therefore, in the presence of serum, submicrometer-sized globules immediately transform and aggregate with plasma proteins to form micrometer-sized aggregates. Therefore, TPFE-DNA complexes remained their sizes within 100 nm for 2 h in the bloodstream, then immediately passed through the lung capillary. However, TPFE-siRNA complexes aggregate with plasma proteins within a minute, and then rapidly accumulated in the lung capillary.

3.3.3 Toxicity

As I described in Chapter 2, the TPFE-siRNA complexes did not show any cytotoxicity in vitro. Importantly, the TPFE-siRNA complexes also showed no acute organ toxicity, especially in lung for 2 weeks after intravenous injection. Rojanasakul et al. have reported that Lipofectamine2000 and other cationic liposomes showed significant dose-dependent toxicity not only in vitro but also in vivo, especially pulmonary inflammation.[10,11] Their study suggests that increasing the cationic charges shows increasing toxicity and inflammatory activity, and reactive oxygen species (ROS) play a key role in the cationic lipid-mediated toxicity. It is well known that the [60]fullerene and its derivatives have a potential to scavenge ROS.[12] TPFE itself works not only as a transfection agent but also as a radical scavenger. Therefore, TPFE-siRNA complexes did not show any toxicity in vivo. This result assures the use of TPFE for the therapeutic application.

3.4. Therapeutic application of siRNA delivery using TPFE for sepsis model

3.4.1 Brief introduction of sepsis

As observed for the experiments of the lung specific delivery of siRNA, I evaluated the potential application of TPFE for sepsis-related death. A rapid accumulation of neutrophils into lungs, especially the narrow lumen of lung capillaries, is thought to underlie the pulmonary failure that leads to the sepsis-related death.[13] Curing the pulmonary failure is one of the challenging tasks in the medical and clinical fields. A major factor contributing to the inappropriate infiltration of neutrophils into lungs is the shedding of lipopolysaccharide (LPS) from Gram-negative bacteria into the circulation. LPS-induced activation of mammalian cells occurs through toll-like receptor-4 (TLR4), the dominant LPS receptor. LPS induces endothelial activation and neutrophils are sequestered into the lungs. Thus, the wild-type mice, C3H/HeN (*TLR4*$^{+/+}$), dramatically increased neutrophils in the lung capillaries induced by the systemic LPS injection, whereas *TLR4* missense mutation mice, C3H/HeJ (*TLR4*$^{-/-}$), from which macrophages completely nonresponsive to LPS, showed no/low accumulation of neutrophils into the lungs with the systemic LPS injection. However, TLR4 works as the immune mechanism, so it is impossible to delete the *tlr4* gene by using the gene therapy. Therefore, RNAi is one of the promising approaches for curing the sepsis-related death by reducing expression of TLR4.

3.4.2 Delivery of TLR4-targeted siRNA for therapeutic application

To evaluate the potential application of TPFE, I intravenously injected TLR4-targeted siRNA (siTLR4) into wild-type C3H/HeN mice (*TLR4*$^{+/+}$). After harvesting for 24 h, LPS was injected intratracheally, and then sacrificed after additional 6 h. The right bronchus was ligated not to contaminate and seep out the Mildform from the bronchus, and then right lung specimens were collected

for RNA and protein analyses. Mildform was injected intratracheally into left lung, and then the left lung was collected for the histological analysis. siGFP was used as a negative control, and missense mutation mouse (C3H/HeJ, *TLR4*$^{-/-}$) was used as a positive control not to accumulate the neutrophils. The knockdown efficiency was expressed the same as the experiments of siGFP delivery (Scheme 3-1).

Scheme 3-1. Schematic illustration of experimental procedure. i.v., intravenous injection; i.t., intratracheal injection.

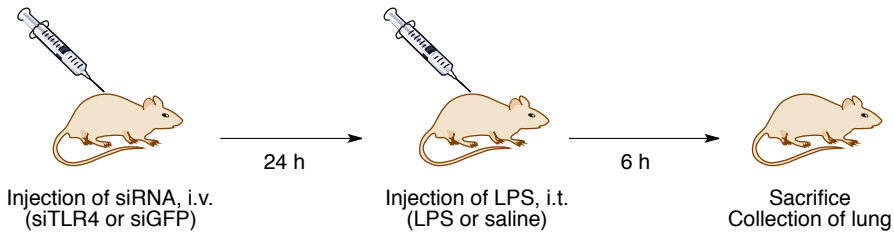

The accumulation of the neutrophils in the lung was determined by counting the number of positive-cells stained with Giemsa staining (Figure 3-7). The significant accumulation of neutrophils was observed when TPFE-siGFP complex was injected into wild-type mice (C3H/HeN, *TLR4*$^{+/+}$), whereas the accumulation was not observed in the case of missense mutation mice (C3H/HeJ, *TLR4*$^{-/-}$, Figure 3-7a, b and d). By the injection of TPFE-siTLR4 the expression of TLR4 mRNA in lung was knocked down (Figure 3-7e), and hence resulted the decrease of the number of neutrophils in lung specimens as same as those of missense mutation mice (Figure 3-7c and d). These results clearly indicate that the delivery of siTLR4 by TPFE suppressed the accumulation of neutrophils in lung.

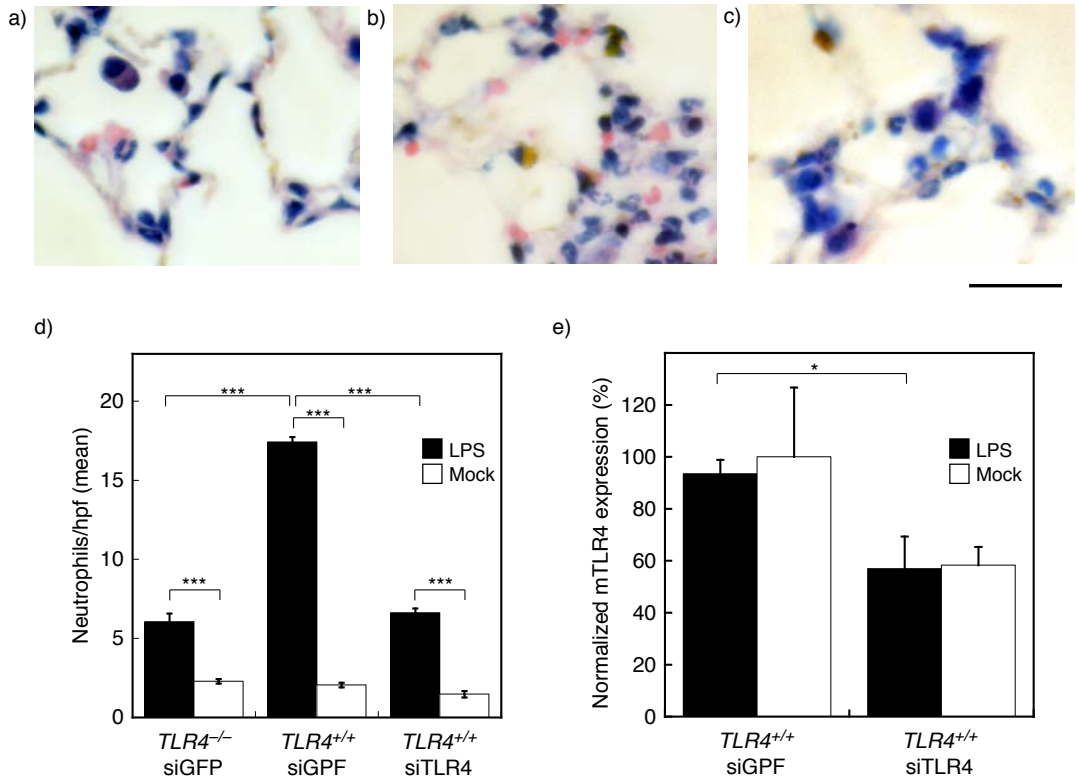

Figure 3-7. Suppression of neutrophil sequestration into lung by lung-specific delivery of siTLR4. a)–c) Neutrophils stained with Giemsa staining. TPFE-siGFP treated mice of C3H/HeJ (*TLR4*$^{-/-}$) (a) and C3H/HeN (*TLR4*$^{+/+}$) (b), and TPFE-siTLR4 treated mouse of C3H/HeN (*TLR4*$^{+/+}$) (c) with intratracheal LPS-injection are shown. Scale bar is 20 μm. d) Quantitative analysis of neutrophil sequestration into lung. Black and white bars show the intratracheal treatment of LPS and saline, respectively. e) Knockdown efficiency of TLR4 mRNA. Error bars are SEM. * $P < 0.05$, *** $P < 0.001$.

3.5. Conclusion

In summary, I developed the lung-specific siRNA delivery system using a cationic fullerene, TPFE with no acute organ toxicity. TPFE-siRNA complexes rapidly accumulated in the lung and internalized into the lung cells due to the globular size increase in the bloodstream. This result assures the usefulness of the cationic fullerene-based siRNA carrier for the clinical applications. In addition, according to the enhanced permeation and retention

(EPR) effect,[14] DDS carriers more effectively accumulate in a solid tumor than normal cells. It is expected that TPFE-siRNA complex effectively accumulates in a lung cancer cells.

3.6. Experimental section

General.

Analysis with high performance liquid chromatography (HPLC) was performed on JASCO HPLC system equipped with an ODS column (Senshu PEGASIL ODS, 4.6 × 250 mm; column temperature at 40 °C) or a Bucky Prep column (Nacalai Tesque Cosmosil Bucky Prep, 4.6 × 250 mm; column temperature at 40 °C). Distilled water was further deionized with Millipore Milli-Q. The dynamic laser light scattering (DLS) study was carried out on a Malvern Zetasizer Nano ZS machine. AFM measurement was conducted on a Shimadzu SPM-9700 with a silicon cantilever (Olympus, OMCL-AC160TS). Quantitative real-time reverse transcriptase-polymerase chain reaction (qRT-PCR) analyses were performed by ABI7000 Sequence Detection System or ViiA7™ Real-Time PCR System (Applied Biosystems).

Materials.

Unless otherwise noted, materials were purchased from Tokyo Kasei Co., Aldrich Inc., and other commercial suppliers and used after appropriate purification before use. Anhydrous ethereal solvents (stabilizer-free) were purchased from WAKO Pure Chemical and purified by a solvent purification system (GlassContour)[15] equipped with columns of activated alumina and supported copper catalyst (Q-5) prior to use. All other solvents were purified by distillation and stored over molecular sieves 4Å. siRNA targeting green fluorescent protein (siGFP) (sense strand, 5′-CGGCAAGCUGACCCUGAAGUU-3′ and antisense strand, 5′-UGAACUUCUGGGUCUGCUUGC-3′), siRNA targeting TLR4 (siTLR4) (sense strand, 5′-GUUCCAUUGCUUGGCGAAUGUUU-3′ and antisense strand, 5′-ACAUUCGCCAAGCAAUGGAACUU-3′) and scrambled siRNA as a

negative control (siNEG) (sense strand, 5′-CGGCAAGUCUCCCAAGGAGUU-3′ and antisense strand, 5′-UGAACUCCUUGGGAGACUUGC-3′) were purchased from Hokkaido System Science Co., Ltd. (Hokkaido, Japan). PCR primers were purchased from Invitrogen. Mouse serum is collected from C57BL/6 mice. LPS from *Escherichia coli* serotype O110:B4 was purchased from Sigma Aldrich.

Mice.

EGFP overexpressed C57BL/6 mice (C57BL/6-Tg (CAG-EGFP)) were purchased from Japan SLC Inc. C3H/HeN and C3H/HeJ mice were purchased from CLEA Japan. All mice were maintained on feed and water *ad libitum*. All animal experiments were conducted in accordance with the National Institutes of Health Guide for the Care and Use of Laboratory Animals.[16]

DLS analysis.

DLS measurement was performed on a Malvern Zetasizer Nano ZS equipped with an He-Ne laser operating at 4 mW power and 633 nm wavelength, and a computer-controlled correlator, at a 173° accumulation angle. Measurement was carried out at room temperature in a polystyrene or glass cuvette. The data were processed using dispersion technology software version 4.10 to give Z-average particle size and polydispersity index (PDI) value by cumulant analysis, and particle size distribution by CONTIN analysis.[17]

siRNA transfection assay in vivo.

8–10 weeks age of EGFP overexpressed mice were used for transfection analyses. Mice were assigned randomly to 1 of 2 groups: the siGFP + TPFE group and the siNEG + TPFE group. TPFE-siRNA complexes containing 100 μg of siRNA with N/P ratio of 20 was injected intravenously.

Mice were maintained on feed and water *ad libitum*. Mice were anesthetized with dietylether, and sacrificed. Tissue specimens from brain, heart, lung, liver, kidney, spleen and peritoneum were collected in TRIzol® reagent and kept –80 °C until use for qRT-PCR.

Determination of RNAi activity.

Total RNAs were extracted from each cells and tissues using TRIzol® reagent (Invitrogen) according to the manufactures' protocol. The extracted total RNAs were treated with DNase to remove the genomic DNAs by using DNA-*free*™ Kit (Ambion) according to the manufactures' protocol. 1 μg of isolated total RNAs were transcribed into cDNA using High Capacity cDNA Reverse Transcription Kit (Applied Biosystems) and Oligo-dT primer according to the manufactures' protocol. Finally, the expression level of target gene and/or housekeeping gene in the cDNA was quantified by quantitative real-time RT-PCR using *Power* SYBR® Green PCR Master Mix or Fast *Power* SYBR® Green PCR Master Mix (Applied Biosystems) according to the manufactures' protocol.

In briefly, chloroform was added into homogenized cells or tissues in TRIzol® reagent in the flesh tube. The sample was mixed well and incubated at room temperature for several minutes. After centrifugation, the aqueous phase was transferred to a flesh tube. Total RNA was precipitated by adding 2-propanol. After centrifugation and removal of supernatant, the total RNA was washed with 75% aqueous solution of ethanol. After centrifugation, the supernatant was removed, and briefly dried. The extracted total RNA was treated with DNase. After incubation for 30 min at 37 °C, DNase was inactivated and transferred the RNA aqueous solution. 1 μg of total RNA was transcribed into cDNA. Reverse transcription reaction was performed at 25 °C for 10 min, at 37 °C for 2 h and 85 °C for 5 sec. The cDNAs were stored at –30 °C

until use.

qRT-PCR was performed using *Power* SYBR® Green PCR Master Mix (Applied Biosystems) and ABI7000 Sequence Detection System with 7000 System SDS Software ver. 1.2 (Applied Biosystems) or Fast *Power* SYBR® Green PCR Master Mix (Applied Biosystems) and ViiA7 Real-Time PCR System with ViiA7 software. Data are presented as the fold difference in GFP expression normalized to the housekeeping gene *β*-Actin as the endogenous reference, and relative to the negative control cells. Primers used in qRT-PCR for GFP, TLR4 and *β*-Actin are: GFP (forward, 5′-GACGTAAACGGCCACAAGTT-3′; reverse 5′-GGTCTTGTAGTTGCCGTCGT-3′), TLR4 (forward 5′-TTTATTCAGAGCCGTTGGTG-3′; reverse, 5′-CAGAGGATTGTCCTCCCATT-3′) and *β*-Actin (forward, 5′-CCACAGCTGAGAGGGAAATC-3′; reverse, 5′-TCTCCAGGGAGGAAGAGGAT-3′). PCR parameters consisted of 2 min at 50 °C, 10 min at 95 °C, followed by 40 cycles of PCR for GFP at 95 °C for 15 sec and at 60 °C for 1 min, by 40 cycles of PCR for TLR4 at 95 °C for 15 sec and at 60 °C for 1 min or by 40 cycles of PCR for *β*-actin at 95 °C for 15 sec and at 60 °C for 1 min.

Lung histology.

To evaluate accumulation of TPFE-siRNA complex in lung, mice treated with TPFE-siRNA intravenously for 15 min, 3, 12 and 24 h, and lungs were fixed with Mildform *via* tracheal injection, and resuspended in Mildform. Formalin-fixed tissues were embedded in paraffin. 5 μm-thick sections were stained with hematoxylin and eosin (H&E) staining for nucleus or without any staining. The accumulation of TPFE-siRNA were determined by area of colored region of 20 fields at a magnification of × 20 from non-stained lung section taken by an optical microscopy (ECLIPSE 80i; Nikon) equipped with digital

camera (DXM1200F) and Nikon ACT-1 software. The mean area per high-power field (100 × 100 μm^2) was then calculated by ImageJ software.

To evaluate neutrophil accumulation into lung, TPFE-siTLR4 complex was injected intravenously into mice (C3H/HeN or C3H/HeJ). After harvesting for 24 h the mice treated intratracheally with LPS or saline for additional 6 h were sacrificed, and right lungs were collected, and left lungs were fixed with Mildform *via* tracheal injection and resuspended in Mildform. Collected lung specimens were stored at –80 °C until use for determination of RNAi activity. Formalin-fixed tissues were embedded in paraffin. 3 μm-thick sections were stained with Giemsa staining for neutrophils. The sections were analyzed by optical microscopy (ECLIPSE 80i; Nikon). Neutrophil numbers were determined by counting the number of positive-stained cells over 20 fields at a magnification of × 40. The mean number of positive cells per high-power field was then calculated.

Figure 3-8. Lung histology without any staining sacrificed at 3 h after injection of saline. Scale bar is 100 μm.

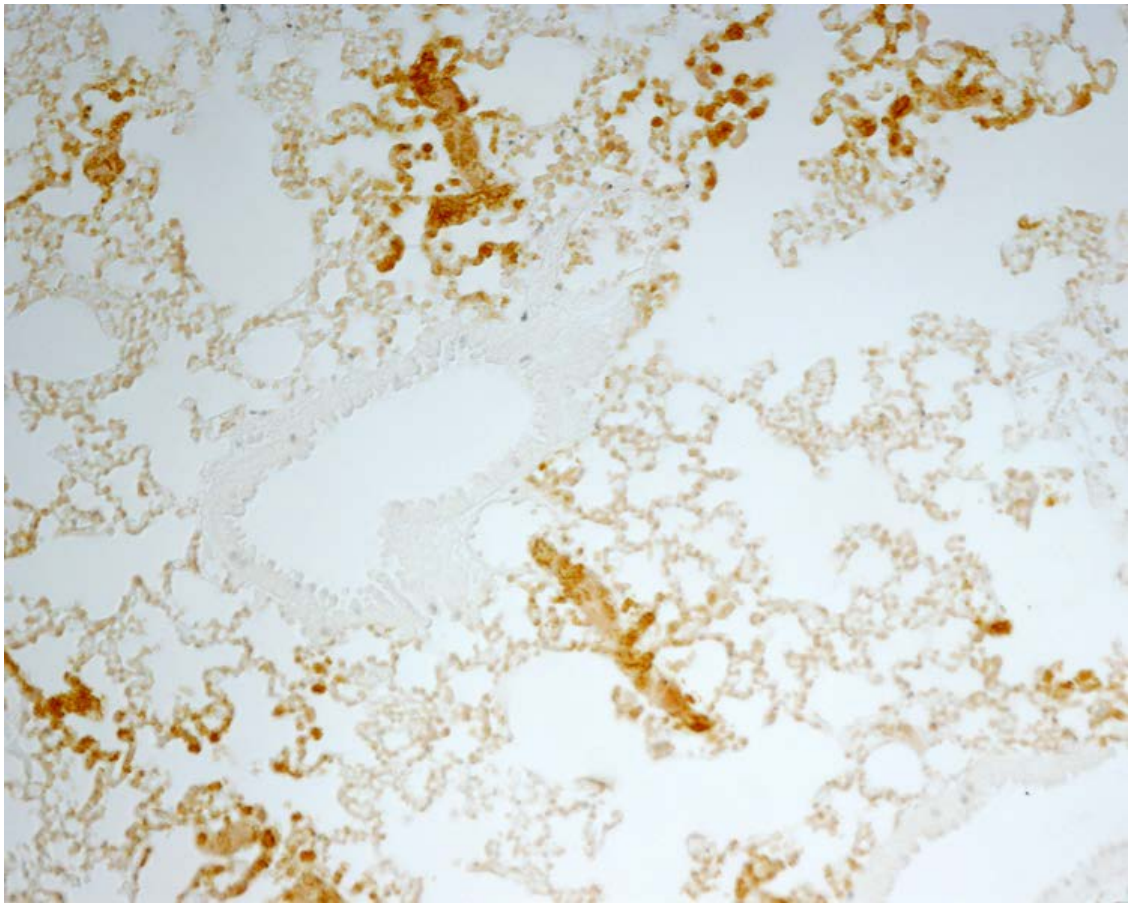

Figure 3-9. Lung histology without any staining sacrificed at 15 min after injection of TPFE-siGFP complex. Scale bar is 100 μm.

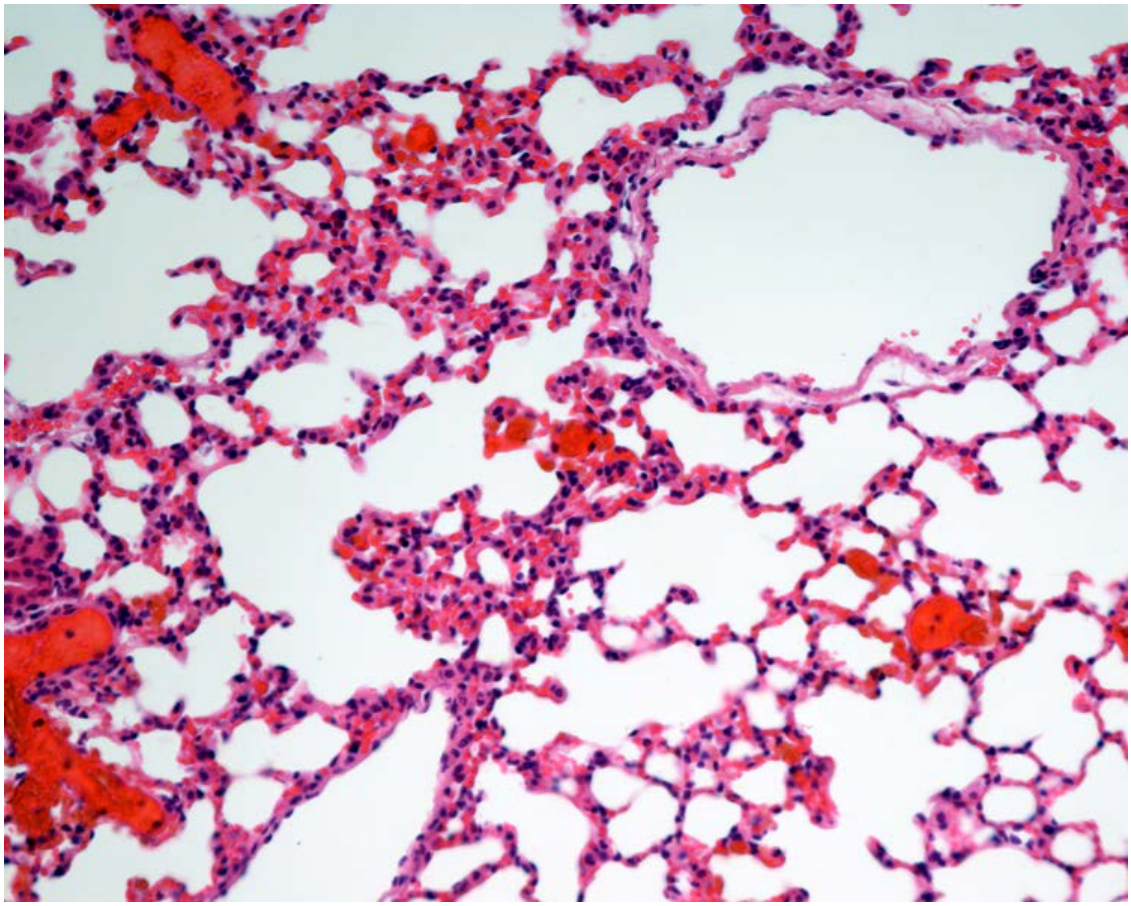

Figure 3-10. Lung histology stained with H&E sacrificed at 15 min after injection of TPFE-siRNA complexes. Scale bar is 100 μm.

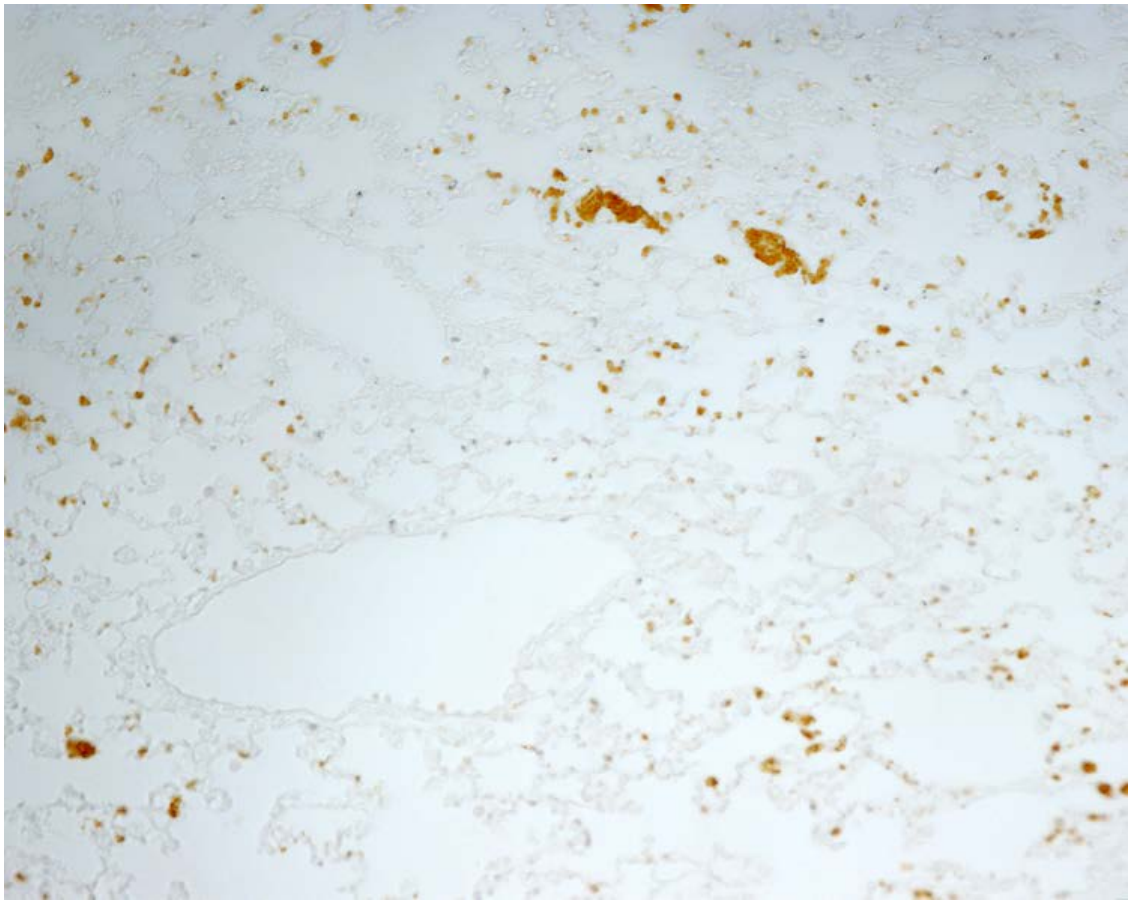

Figure 3-11. Lung histology without any staining sacrificed at 3 h after injection of TPFE-siGFP complex. Scale bar is 100 μm.

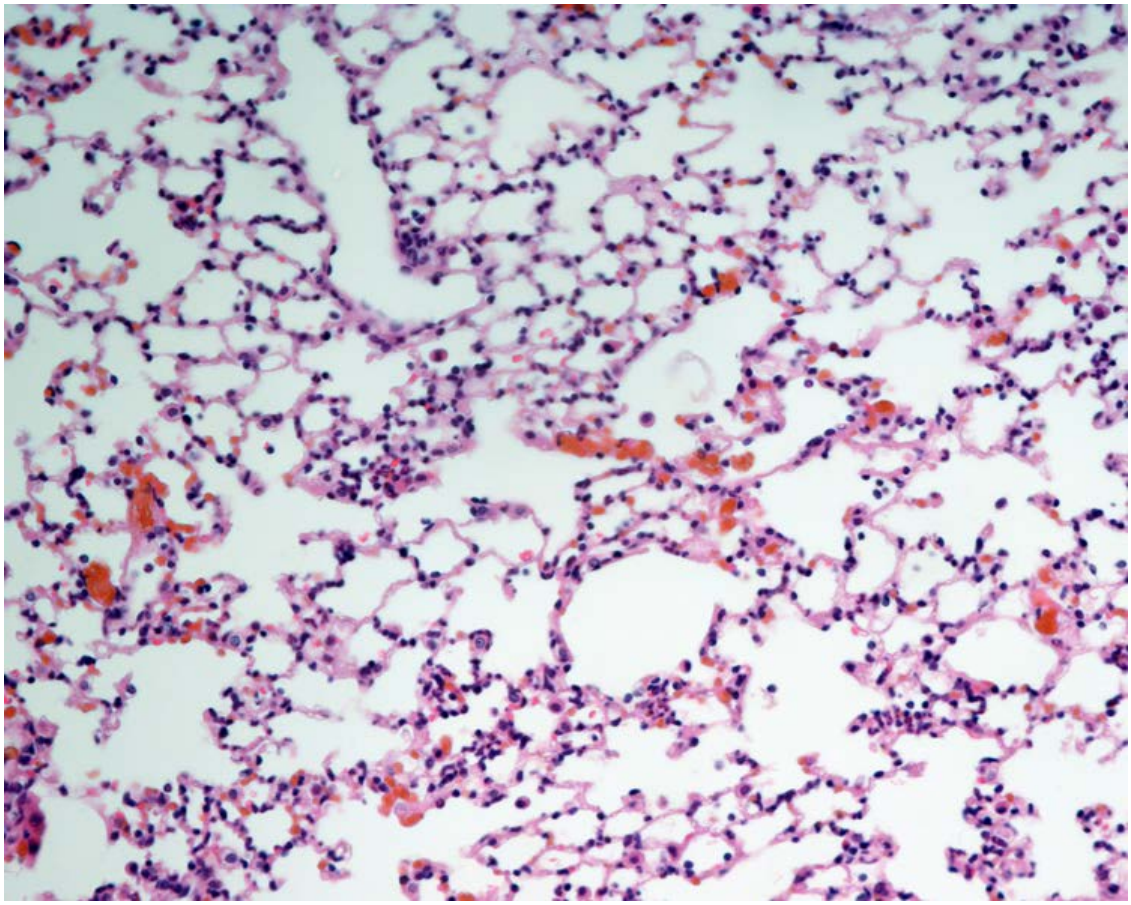

Figure 3-12. Lung histology stained with H&E sacrificed at 3 h after injection of TPFE-siRNA complexes. Scale bar is 100 μm.

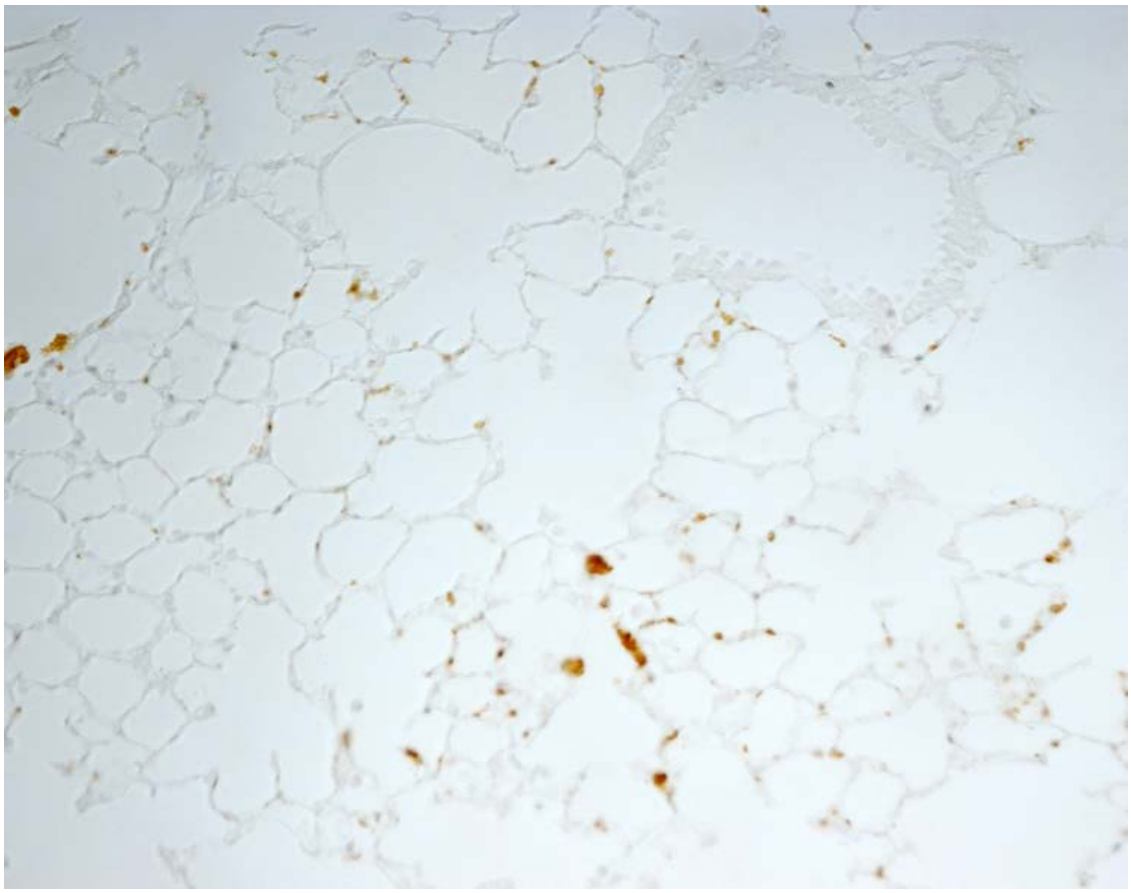

Figure 3-13. Lung histology without any staining sacrificed at 12 h after injection of TPFE-siGFP complex. Scale bar is 100 μm.

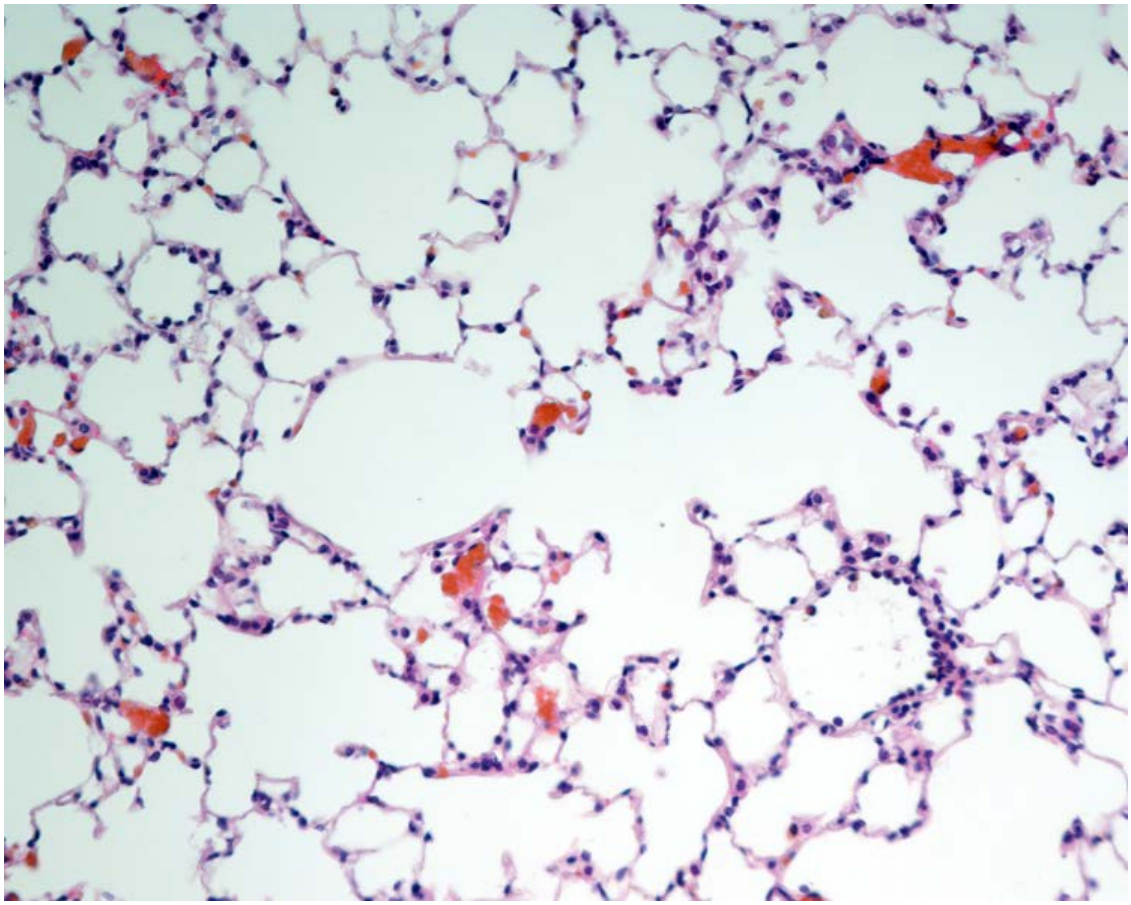

Figure 3-14. Lung histology stained with H&E sacrificed at 12 h after injection of TPFE-siRNA complexes. Scale bar is 100 μm.

Figure 3-15. Lung histology without any staining sacrificed at 24 h after injection of TPFE-siGFP complex. Scale bar is 100 μm.

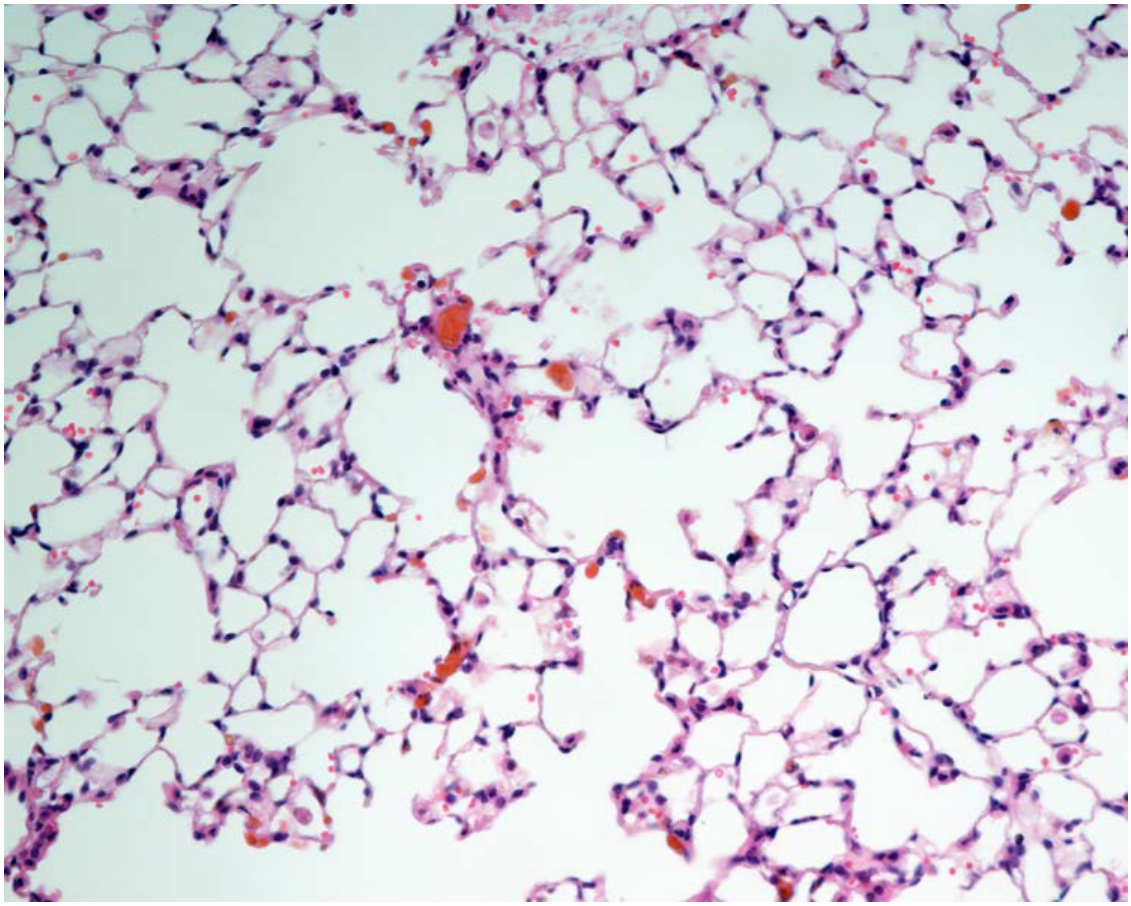

Figure 3-16. Lung histology stained with H&E sacrificed at 24 h after injection of TPFE-siRNA complexes. Scale bar is 100 μm.

Statistical analysis.

Differences among the experimental groups were detected using Student's t-test. Values are expressed as means ±SEM; $p < 0.05$ was considered significant.

References

[1] Fire, A.; Xu, S.; Montgomery, M. K.; Kostas, S. A.; Driver, S. E.; Mello, C. C. *Nature* **1998**, *391*, 806–811.

[2] Whitehead, K. A.; Langer, R.; Anderson, D. G. *Nat. Rev. Drug Discov.* **2009**, 8, 129–138.

[3] (a) Kitamura, H.; Ichinose, S.; Hosoya, T.; Ando, T.; Ikushima, S.; Oritsu, M.; Takemura, T. *Pathol. Res. Pract.* **2007**, *203*, 575–585. (b) Klonne, D. R.; Dodd, D. E.; Losco, P. E.; Troup, C. M.; Tyler, T. R. *Fundam. Appl. Toxicol.* 1998, *10,* 682–690.

[4] Eldem, T.; Speiser, P.; Hincal, A. *Pharm. Res.* **1991**, *8*, 47–54.

[5] Saralidze, K.; Van Hooy-Corstjens, C. S.; Koole, L. H.; Knetsch, M. L. *Biomaterials* **2007**, *28*, 2457–2464.

[6] Yang, R.; Yang, S.-G.; Shim, W.-S.; Cui, F.; Cheng, G.; Kim, I.-W.; Kim, D.-D.; Chung, S.-J.; Shim, C.-K. *J. Pharm. Sci.* **2009**, *98*, 970–984.

[7] (a) Isobe, H.; Nakanishi, W.; Tomita, N.; Jinno, S.; Okayama, H.; Nakamura, E. *Mol. Pharm.* **2006**, *3*, 124–134. (b) Ying, Q.; Zhang, J.; Liang, D.; Nakanishi, W.; Isobe, H.; Nakamura, E.; Chu, B. *Langmuir* **2005**, *21*, 9824–9831. c) Nakamura, E.; Isobe, H.; Tomita, N.; Sawamura, M.; Jinno, S.; Okayama, H. *Angew. Chem. Int. Ed.* **2000**, *39*, 4254–4257.

[8] (a) Maeda-Mamiya, R.; Noiri, E.; Isobe, H.; Nakanishi, W.; Okamoto, K.; Doi, K.; Sugaya, T.; Izumi, T.; Homma, T.; Nakamura, E. *Proc. Natl. Acad. Sci. U.S.A.* **2010**, *107*, 5339–5344. (b) Isobe, H.; Nakanishi, W.; Tomita, N.; Jinno, S.; Okayama, H.; Nakamura, E. *Chem.–Asian J.* **2006**, *1–2*, 167–175.

[9] Marangon, I.; Boggetto, N.; Ménard-Moyon, C.; Venturelli, E.; Béoutis, M.-L.; Péchoux, C.; Luciani, N.; Wilhelm, C.; Bianco, A.; Gazeau, F. *Nano Lett.* **2012**, *12*, 4830–4837.

[10] (a) Maurer, N.; Mori, A.; Palmer, L.; Monck, M.A.; Mok, K. W. C.; Mui, B.; Akhong, Q. F.; Cullis, P. R. *Mol. Membr. Biol.* **1999**, *16*, 129–140. (b) Lewis, R. J.; Huang, J. H.; Pecora, R. *Macromolecules* **1985**, *18*, 944–948.

[11] Dokka, S.; Toledo, D.; Shi, X.; Castranova, V.; Rojanasakul, Y. *Pharm.*

Res. **2000**, *17*, 521–525.

[12] (a) Lens, M.; Medenica, L.; Citernesi, U. *Biotechnol. Appl. Biochem.* **2008**, *51*, 135–140. (b) Krusic, P. J.; Wasserman, E.; Keizer, P. N.; Morton, J. R.; Preston, K. F. *Science* **1991**, *254*, 1183–1185.

[13] Andonegui, G.; Bonder, C. S.; Green, F.; Mullaly, S. C.; Zbytnuik, L.; Raharjo, E.; Kubes, P.*J. Clin. Invest.* **2003**, *111*, 1011–1020.

[14] Matsumura, Y.; Maeda, H. *Cancer Res.* **1986**, *46*, 6387–6392.

[15] Pangborn, A. B.; Giardello, M. A.; Grubbs, R. H.; Rosen, R. K.; Timmers, F. J. *Organometallics* **1996**, *15*, 1518–1520.

[16] Committee on Care and Use of Laboratory Animals (1985) Guide for the Care and Use of Laboratory Animals (Natl. Inst. Health, Bethesda), DHHS Publ No (NIH) 85–23.

[17] (a) Provencher, S. W. *Biophys. J.* **1976**, *16*, 27–41. (b) Provencher, S. W. *Comp. Phys. Comm.* **1982**, *27*, 213–227.

Chapter 4. Post-Modification of Fullerene Vesicle via Cu(I)-Catalyzed Click Reaction and its Application for Drug Delivery Systems

4.1. Introduction

Sub-100 nm capsular objects such as virus capsids displaying proteins on their surface serve as a model of nm-sized tools for detection, reporting and delivery of molecules, such as drugs and imaging dyes, in a biological environment.[1] Biological nanocapsules are formed by controlled integration of functional parts through multistep covalent and noncovalent chemical processes, which, however, is difficult to achieve in a flask for several reasons: the paucity of methods to prepare sub-100 nm capsular platforms under mild conditions, to modify their structures after their formation in water and, most importantly, and to analyze with molecular precision the structure of such sub-100 nm objects that typically lack structural uniformity and periodicity.[2]

Our group made a unique discovery sometimes ago that fullerene anions bearing five aryl groups on the topside of the molecules (fullerene penta-adducts) in water spontaneously form vesicular structure (Scheme 4-1).[3,4,5] The vesicles show unimodal distribution of diameter centered at ca. 30 nm,[3,4,5] exhibit low water permeability,[4,6] and no cytotoxicity.[7] Interestingly, these fullerene anions except pentaphenyl fullerene (**PhK**) has unique amphiphilic structure, in which non-polar (fullerene core)/polar (cyclopentadienide anion)/non-polar (aryl groups) motif compared with traditional lipids (polar head/non-polar tail). Owing to this unique structure and strong cohesive force of fullerene core, the substituents on the aryl groups expose to the aqueous phase. Therefore, it is expected that the post-functionalization of fullerene vesicle can be achieved by introduction of reaction sites on the substituents of fullerene.

Scheme 4-1. Schematic illustration of fullerene vesicles.

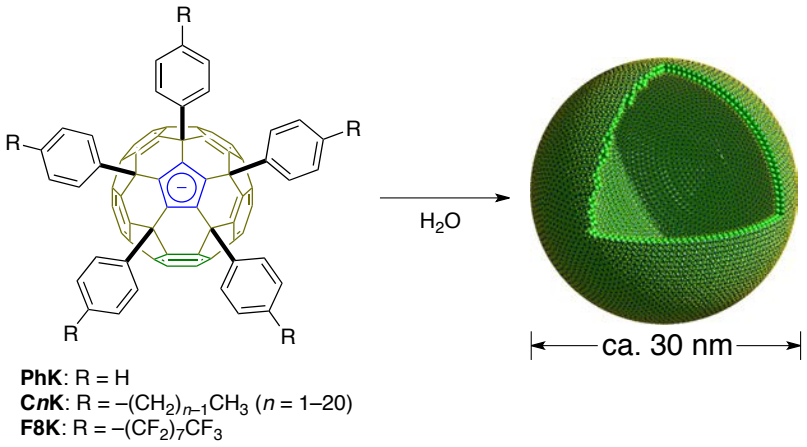

Huisgen 1,3-dipolar cycloaddition reaction[8] has been widely used in many fields after the discovery in 2002 of Cu(I) catalyst by Meldal et al. and Shapless et al. independently because of a major improvement in both of rate and regioselectivity.[9] Notably, biological application of this reaction, including the drug delivery systems, has gained considerable attention due to the tolerance in aqueous media.[10] Thus, it is expected that this cycloaddition reaction can be applicable for post-functionalization of the fullerene vesicle.

In this study, I developed a sub-100 nm capsule platform for construction of protein-covered nanocapsules through covalent and noncovalent stepwise post-functionalization in a highly controlled manner using the potassium salt of penta(oct-7-yl)fullerene (**C8(7Y)K**). Their structures was characterized with a state-of-the-art, subnanometer spatial resolution, low-accelerating-voltage scanning electron microscopy (SEM) equipped with a monochromatic electron source.[11] Finally, I demonstrated the vesicle for the vehicle of drug delivery systems.

4.2. Characterization of post-functionalizable fullerene vesicle

4.2.1 Synthesis and preparation of alkynyl fullerene vesicle

Penta-alkynyl fullerene **C8(7Y)H** was synthesized by penta-addition reaction of organocopper reagent to [60]fullerene (Scheme 4-2).[12] Grignard reagent **1** was prepared from corresponding bromide **3**. The organocapper reagent was prepared from Grignard reagent **1** in situ to react with C_{60} followed by a desilylation reaction to afford penta-alkynyl fullerene **C8(7Y)H** in 66% yield.

Scheme 4-2. Synthesis of penta-alkynyl fullerene **C8(7Y)H**.

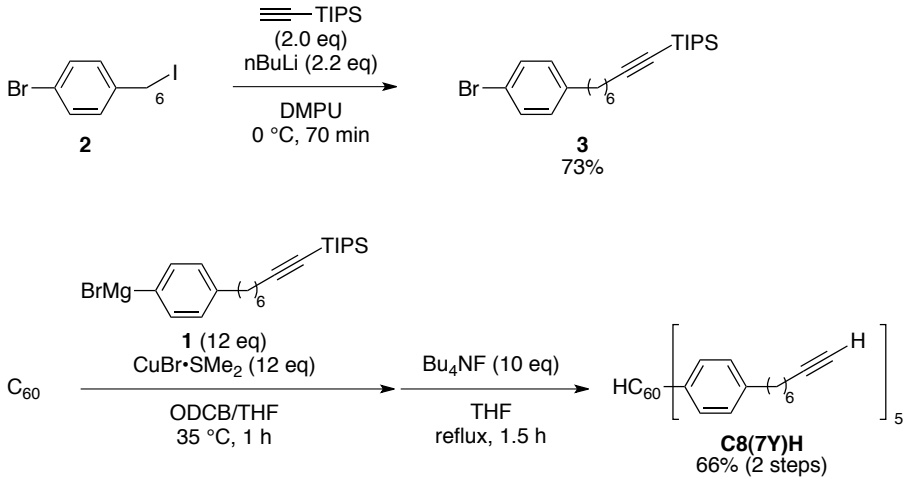

C8(7Y)K vesicle was prepared following to the reported procedure (Scheme 4-3).[3,4,5] **C8(7Y)H** was treated with *t*-BuOK in THF to afford a THF solution of potassium anion **C8(7Y)K**, then the solution was slowly injected into pure water or D_2O followed by removal of THF under reduced pressure to obtain an reddish orange colored transparent solution. It is notable that the anion **C8(7Y)K**, which has the highly hydrophobic fullerene as well as the hydrophobic alkyl chains, can dissolve in water.

Scheme 4-3. Preparation of **C8(7Y)K** vesicle.

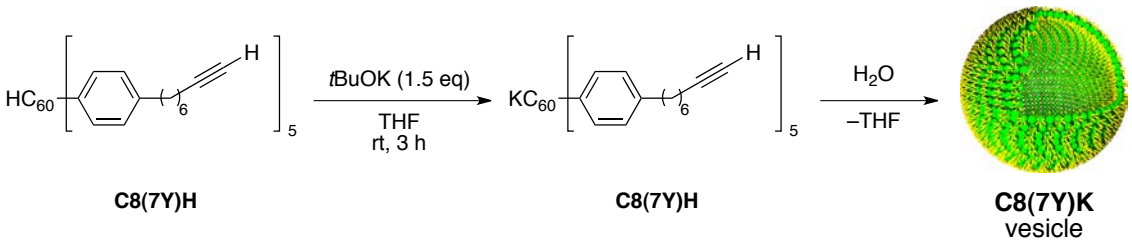

A dynamic light scattering (DLS) measurement was performed to measure an average hydrodynamic radius (Figure 4-1). **C8(7Y)K** vesicle is very stable in solution without significant size changes at 10 to 90 °C or after storage for over one year at room temperature in air. As reported fullerene vesicles,[3,4,5] ^{1}H and ^{13}C NMR analyses in D_2O did not give any signals due to the densely packed bilayer structure. DLS analysis of the vesicle showed a narrow distribution (polydispersity index (PDI), 0.05) in cumulant analysis and the average hydrodynamic radius was determined as 8.1 ± 0.1 nm. Therefore, one vesicle exposes about 400 fullerene molecules and 2000 alkyne termini on the surface.

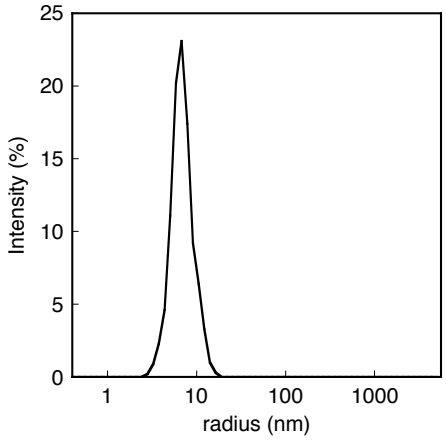

Figure 4-1. DLS analysis of C8(7Y)K vesicle.

A scanning transmission electron microscopy (STEM) analysis and an

atomic force microscopy (AFM) analysis were conducted (Figure 4-2; see also Figure 4-21). The STEM image clearly showed the round shape objects with a narrow size distribution. The contrast of the round shape objects of the STEM image is weaker than those of the STEM image of other fullerene vesicles.[3,4,5] It assumed that the spherical objects collapsed under a condition of the STEM observation. On the other hand, according to the AFM image, the height of the aggregate is around 18 nm, which indicates a good agreement with the results of the DLS analysis. Nevertheless, this result suggests that the spherical aggregated structure was obtained in the solution state. These results concluded that the anion of **C8(7Y)K** forms the bilayer vesicle structure.

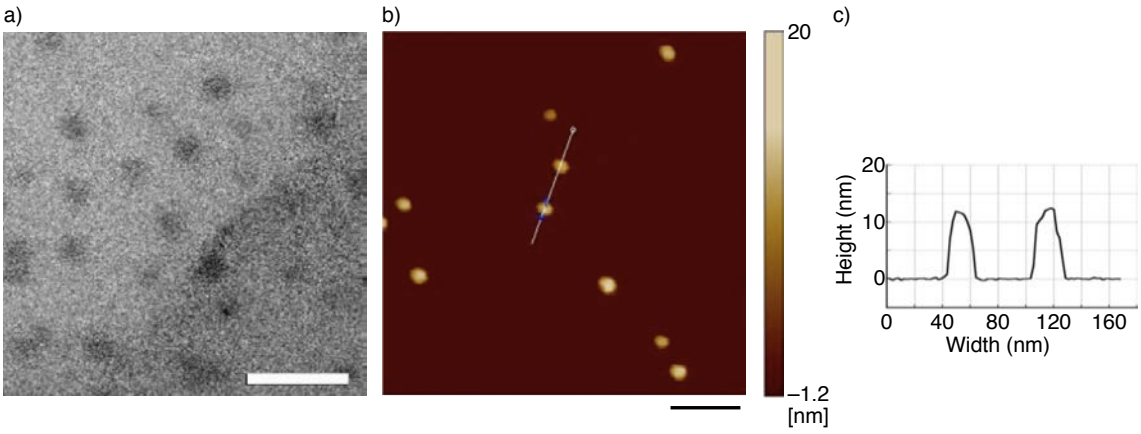

Figure 4-2. Characterization of the **C8(7Y)K** vesicle. a) STEM image of the vesicle on carbon film without metal coating. Scale bar is 50 nm. b) AFM image of the vesicle on mica substrate. Scale bar is 500 nm. c) Height profile of AFM image in ***Figure 4-2***b.

4.2.2 Encapsulation of organic molecules in the fullerene vesicle

To apply the **C8(7Y)K** vesicle for the DDS carrier, evaluation of its ability of the encapsulation of molecules is necessary. I prepared a carboxyfluorescein encapsulated fullerene vesicle. The THF solution of **C8(7Y)K** was slowly injected into an aqueous solution of 5(6)-carboxyfluorescein (1.7 mM), then the aqueous solution of carboxyfluorescein and **C8(7Y)K** vesicle was

purified by gel permeation chromatography on Sephadex G-50 for the removal of excess amount of carboxyfluorescein, which exist outside of the vesicle (Scheme 4-4).

Scheme 4-4. Preparation of solute-encapsulated **C8(7Y)K** vesicle. a) Schematic illustration of solute-encapsulated vesicle. b) Structure of 5(6)-carboxyfluorescein.

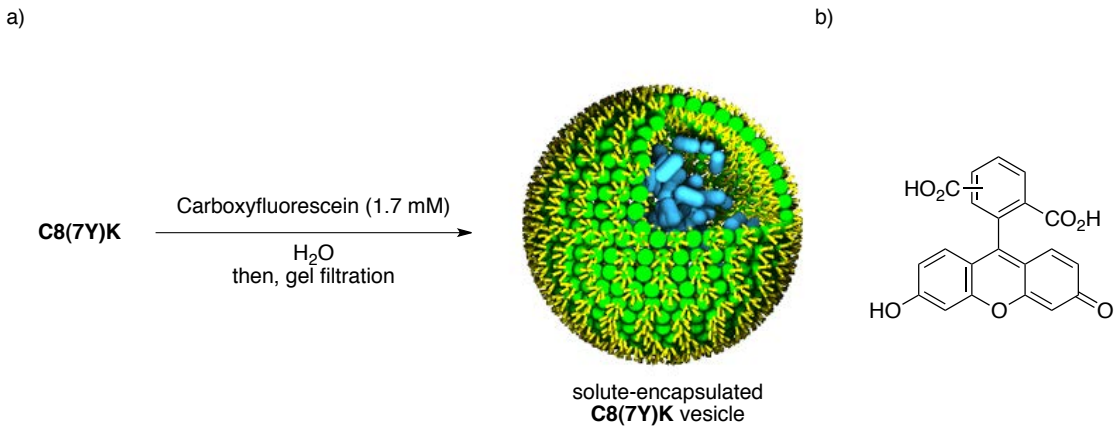

The encapsulated carboxyfluorescein was measured by a fluorescence measurement (Figure 4-3). The fluorescence originated from carboxyfluorescein (λ_{em} = 518 nm) was observed from the vesicle, but the intensity did not change till 24 h. **C8(7Y)K** vesicle was removed by addition of aqueous solution of NH_4Cl for protonation of the cyclopentadienide moiety to obtain a precipitate. After removal of precipitate, the pH value of the obtained aqueous solution was adjusted as the same as the initial value by addition of NaOH aq. solution, because the fluorescence of carboxyfluorescein is sensitive to pH.[13] The fluorescent intensity was significantly increased, indicating that the **C8(7Y)K** vesicle entrapped the carboxyfluorescein in its hollow space and on its fullerene membrane. This result clearly suggests the applicability of the DDS carrier.

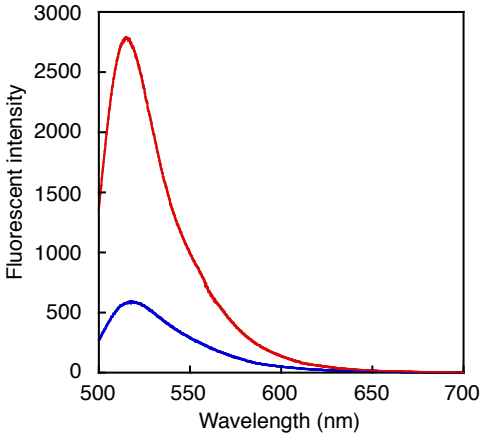

Figure 4-3. Fluorescence analysis of the carboxyfluorescein-encapsulated **C8(7Y)K** vesicle. The concentrations of anion of the **C8(7Y)K** are 13 μM. Excitation wavelength is 490 nm. The measurement was conducted in water at 25 °C.

4.2.3 Post-functionalization of fullerene vesicle by click reaction

To examine the efficiency of surface modification after the formation of **C8(7Y)K** vesicle (post-functionalization) by chemical reaction, I first performed the copper(I)-catalyzed click reaction with an 7-hydroxy-3-azidocumarin **4** (Figure 4-4a), which by itself is fluorescently inactive but becomes intensely fluorescent after the formation of 1,2,3-trizole ring because of the loss of the azido group by cycloaddition.[14] I monitored the click reaction by the fluorescence of the 7-hydroxycoumarin group at 530 nm (λ_{ex} = 490 nm) (Figure 4-4). The **C8(7Y)K** vesicle (2.5 μM) was treated with 5 eq (for one **C8(7Y)K** molecule) of azidocoumarin **1** in the presence of copper(II) sulfate (100 mol%, 20 mol% per terminal alkynyl groups) and sodium ascorbate as a reducing agent. The fluorescent intensity at 530 nm rapidly increased in a week and reached a plateau after 2 weeks (Figure 4-4c, blue). On the other hand, the fluorescent intensity of the saturated analogue of **C8(7Y)K**, **C8K**, did not increased (Figure 4-4c, red), suggesting that the terminal alkynes on the surface of the fullerene vesicle selectively react with azide compounds.

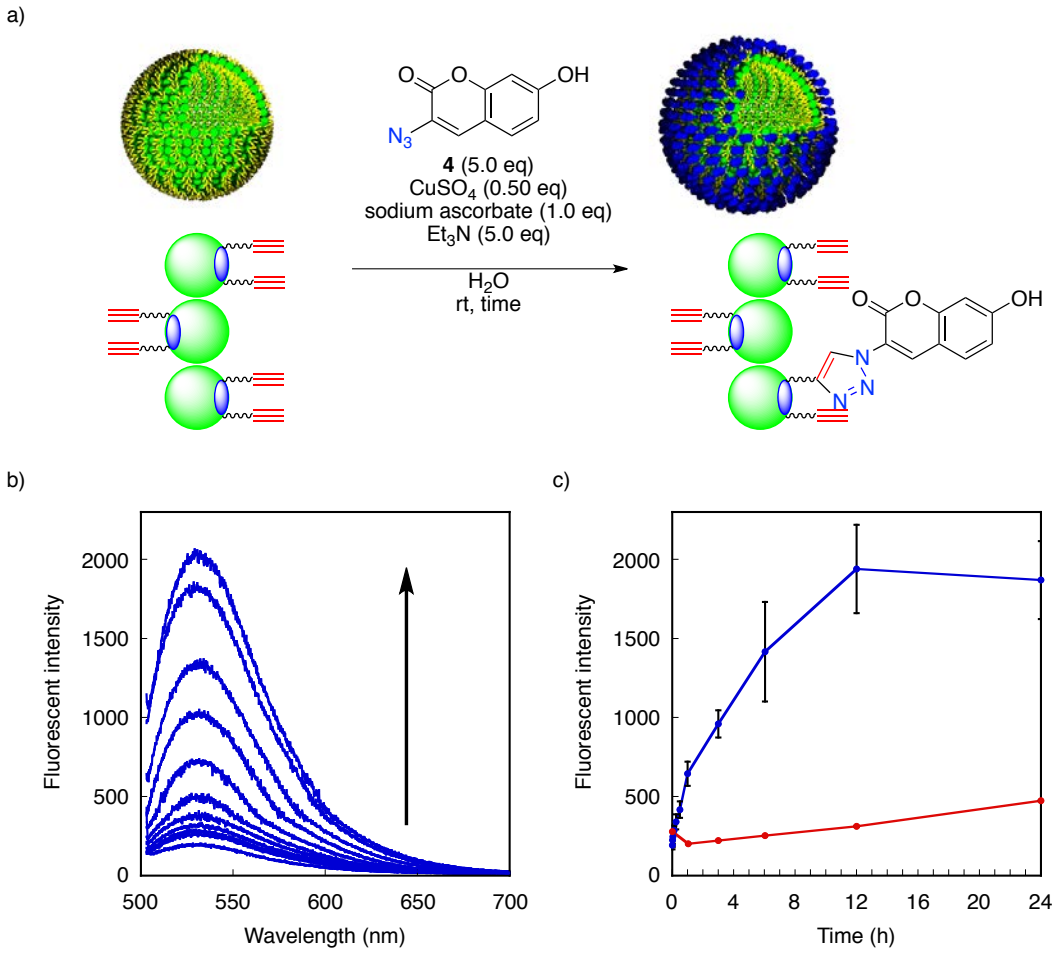

Figure 4-4. Surface modification of the **C8(7Y)K** vesicle with a coumarin fluorophore. (a) Schematic illustration of the click reaction with azidocoumarin **4** on the vesicle surface. (b) Fluorescence spectral change by the reaction of the **C8(7Y)K** vesicle with azidocoumarin **4**. (c) Average fluorescent intensity at 530 nm for the **C8(7Y)K** vesicle (blue) and the **C8K** vesicle (red) as a function of reaction time ($N = 3$).

By comparison of the molar fluorescent intensity of a reference triazolo-product of the azidocoumarin **4** and 1-hexyne, I estimate that 19% of the terminal alkyne groups (i.e. one octynyl group per one fullerene) reacted with the azidocoumarin **4** (Figure 4-5). Note that the maximum wavelength of the fluorescence from the coumarins on the vesicle was red-shifted when compared with triazolocoumarins in a neutral pH solution (492–497 nm),[14] which is ascribed to the slightly basic condition in the reaction (pH 8–9) as

7-hydroxycoumarin derivatives show red-shifted fluorescence peaks in a basic solution.[15]

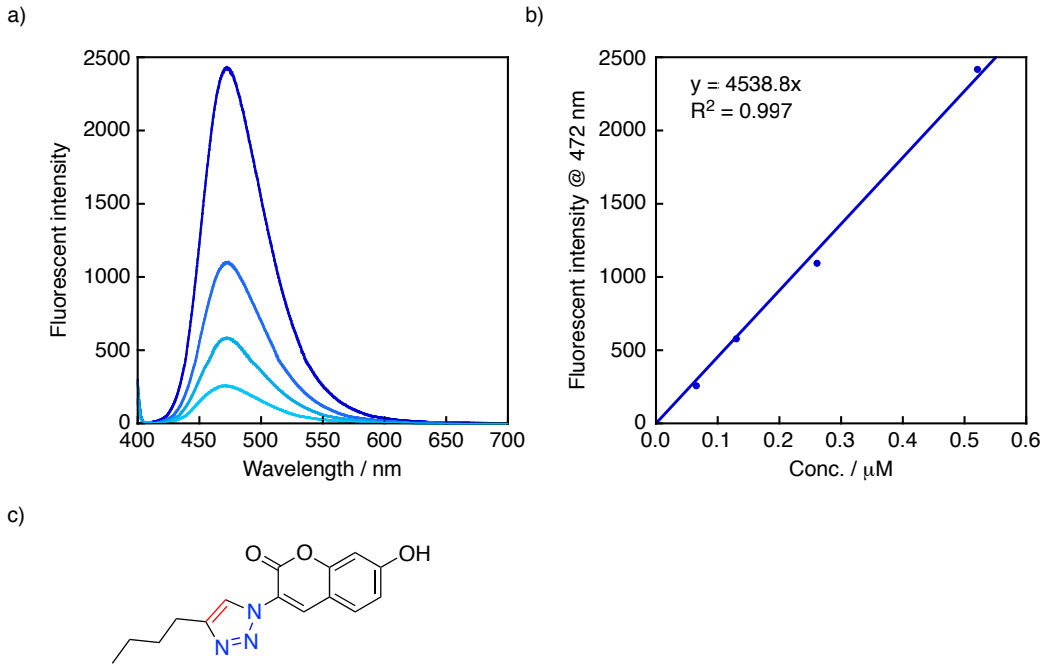

Figure 4-5. Fluorescent analysis of reference addition product of azidocoumarin 1 and 1-hexyne. (a) Fluorescent intensity (λ_{ex} = 390 nm at 25 °C in water) in the range of concentration from 0.07 to 1.04 μM. (b) Fluorescent intensity at 472 nm as a function of concentration. (c) Structure of a reference product.

4.3. Construction and characterization of protein-covered fullerene vesicle

4.3.1 Preparation of avidin-covered vesicle

I next installed biotin groups on the surface of the **C8(7Y)K** vesicle by the click reaction for construction of an avidin-covered fullerene vesicle. To prepare the avidin-covered vesicle, more than 60 biotin residues are required per a vesicle. Therefore, the efficiency of the click reaction (19%) is high enough for fully covering the surface. The **C8(7Y)K** vesicle was reacted with 5 equiv. of azido-tagged biotin-tetra(ethylene)glycol (TEG) conjugate **biotin-N**$_3$[16] in the presence of copper(II) sulfate and sodium ascorbate as same procedure as I described above, followed by the purification using the gel permeation

chromatography on Sephadex G-50 for removal of unreacted **biotin-N**$_3$ to obtain the biotinylated **C8(7Y)K** vesicle (Biotin-**C8(7Y)K**). I then noncovalently attached avidin, which is a protein known as a strong binding with a biotin moiety, to the biotinylated vesicle. Avidin-covered vesicle was prepared upon mixing the vesicle with avidin in phosphate buffered saline (PBS) (fullerene/avidin mole ratio of 1:1).

4.3.2 DLS analyses of avidin-covered vesicle

Biotinylated fullerene vesicle and avidin-covered vesicle was first analyzed by DLS (Figure 4-6). The size distribution of the biotin vesicle was rather narrow (PDI, 0.12) and the average hydrodynamic radius increased by 3.5 nm from 8.1 ± 0.1 to 11.6 ± 0.1 nm (Figure 4-6a, blue), which roughly agrees with the length of the tethered biotin unit (ca. 2.8 nm). Importantly, no size change in DLS occurred during the purification, indicating that the Biotin-**C8(7Y)K** vesicle is robust enough to be purified by gel permeation chromatography. On the other hand, the DLS analysis of the solution of the avidin vesicle gave a very broad peak centered at 41 nm (Figure 4-6a, red). The large PDI (0.23) suggested the aggregation of vesicles. The avidin is a tetrameric protein and each subunit has a binding pocket, so the avidin molecule induced the aggregation of the protein-covered vesicles in an aqueous solution. Hence, the DLS analysis gave a little information of the individual vesicle particles. These results indicate that the DLS analysis tolerates for the determination of covalent modification of nanomaterials but dose not tolerate for the noncovalent modification.

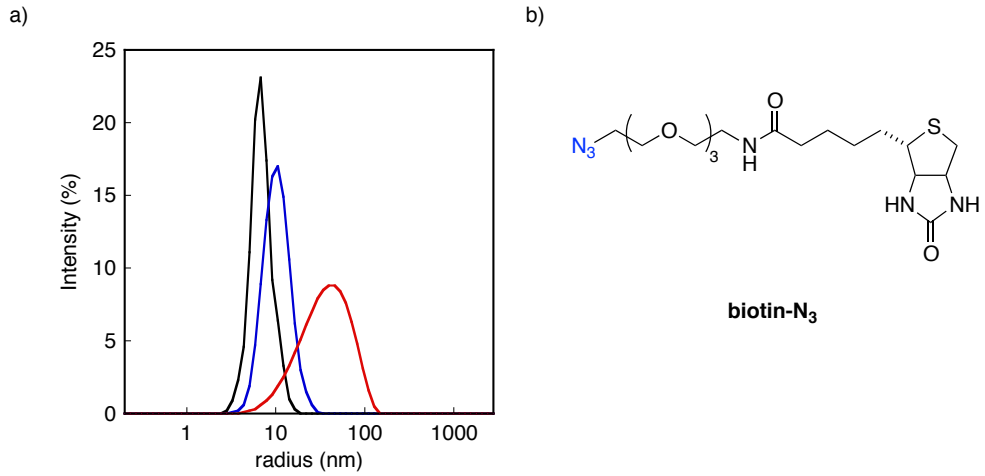

Figure 4-6. DLS analysis of the **C8(7Y)K** vesicles. a) Hydrodynamic radii distribution of the **C8(7Y)K** (black), Biotin-**C8(7Y)K** (blue) and avidin vesicles (red) are shown. b) Structure of **biotin-N**$_3$.

4.3.3 Sub-nm resolution SEM observation of protein-coated fullerene vesicles

The aggregation is a ubiquitous phenomenon and represents a bottleneck for structural analysis in studies on self-assembled organic materials and proteins. Thus, the obscure DLS and uninformative spectroscopic data provided no definitive evidence for the attachment of avidin molecules as I described above. It is required the characterization techniques for individual objects with a high resolution. Scanning electron microscopy (SEM) imaging can be applicable for the observation of the vesicles. However, the conventional SEM imaging technique of proteins has the big problems: (1) Specimens must often be left unstained to observe details of the biological structures; however, lack of staining significantly decreases image contrast. (2) Damage by electrons. I consider it useful to explore the utility of a state-of-the-art SEM that features low acceleration voltage, a monochromatic electron beam (< 0.2 eV energy spread), and a subnanometer spatial resolution. Not just allowing for imaging of fine surface details, these features remove two inherent problems of conventional SEM imaging that have prevented its application to the

nanometer-resolution analysis of nonconducting objects: nanometer-thick Pt/Pd coating of the specimen that greatly reduces the quality of the information on the surface structure and electron damage to the specimen.

I found that the vesicles (**C8(7Y)K**, Biotinylated **C8(7Y)K** and avidin vesicles) can be best analyzed after spin coating the solutions at 1500 rpm on an indium tin oxide (ITO)/glass substrate that was cleaned by UV/ozone treatment immediately before use. The coated substrates were dried for 1 h at room temperature kept at 5×10^{-5} Pa before being placed in the SEM chamber. Imaging was achieved with an electron beam current of 25 pA with an acceleration voltage between 1 and 2 kV. The state-of-the-art SEM combined with the use of a superhydrophilic and conducting ITO substrate permitted to obtain subnanometer resolution images of the vesicles and the small protein molecules because of the high affinity. The use of conductive ITO substrate for micrometer-resolution SEM imaging of cultured cells without metal staining was first reported by Fransen.[17] I found that the ITO is a good substrate for subnanometer-resolution studies. This SEM machine features unicolor technology to realize monochromatic electron beam (< 0.2 eV energy spread) and observation at short working distance (WD) of 1 mm, which was achieved by a new objective lens technology. The microcrystals of ITO and avidin molecules can be observed clearly without metal coating (Figure 4-7a). An SEM using a nonmonochromatic electron source (electron beam with > 0.65 eV energy spread) produced the image in Figure 4-7b that has an image contrast too low to be useful.

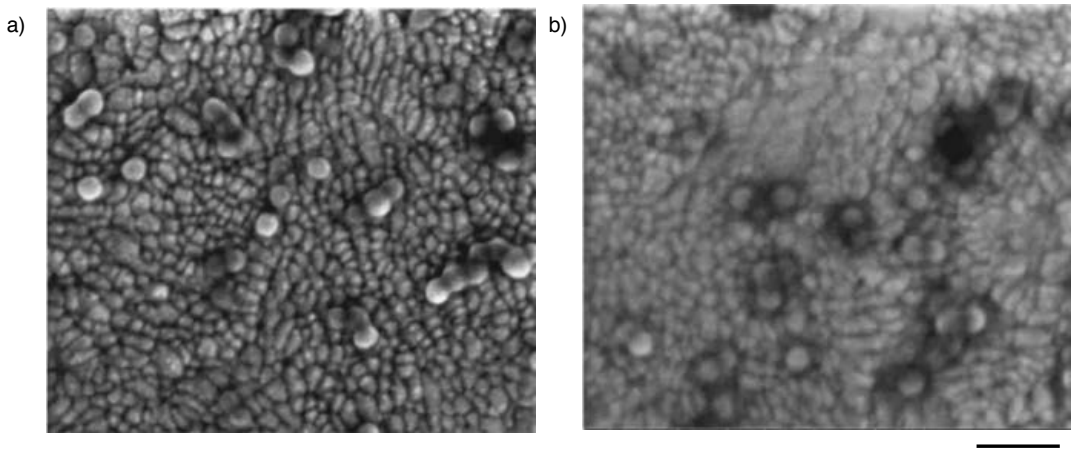

Figure 4-7. Avidin-coated vesicles on ITO/glass. (a) Image taken under operation in unicolor mode with WD of 1 mm. (b) Without unicolor mode at WD of 4 mm (conventional SEM analysis condition). We could not compare images of the same area by using different mode due to contamination of irradiated area at the first scan of image acquisition. Scale bar is 100 nm.

Figure 4-8 illustrates the detrimental effects on the image quality of the conventional Pt/Pd coating of the specimen. The metal coating covered the avidin molecules and the ITO microcrystals (Figure 4-8b and c), which could not be analyzed the detail of the surface. The coating increased the average radius of vesicle by 4 nm to 19.7 ± 2.2 nm or more to 24.6 ± 3.4 nm after 1 or 5 nm Pt/Pd coating (Figure 4-8d). Mica and silica substrates are insulating and hence resulted sample charge-up and no images.

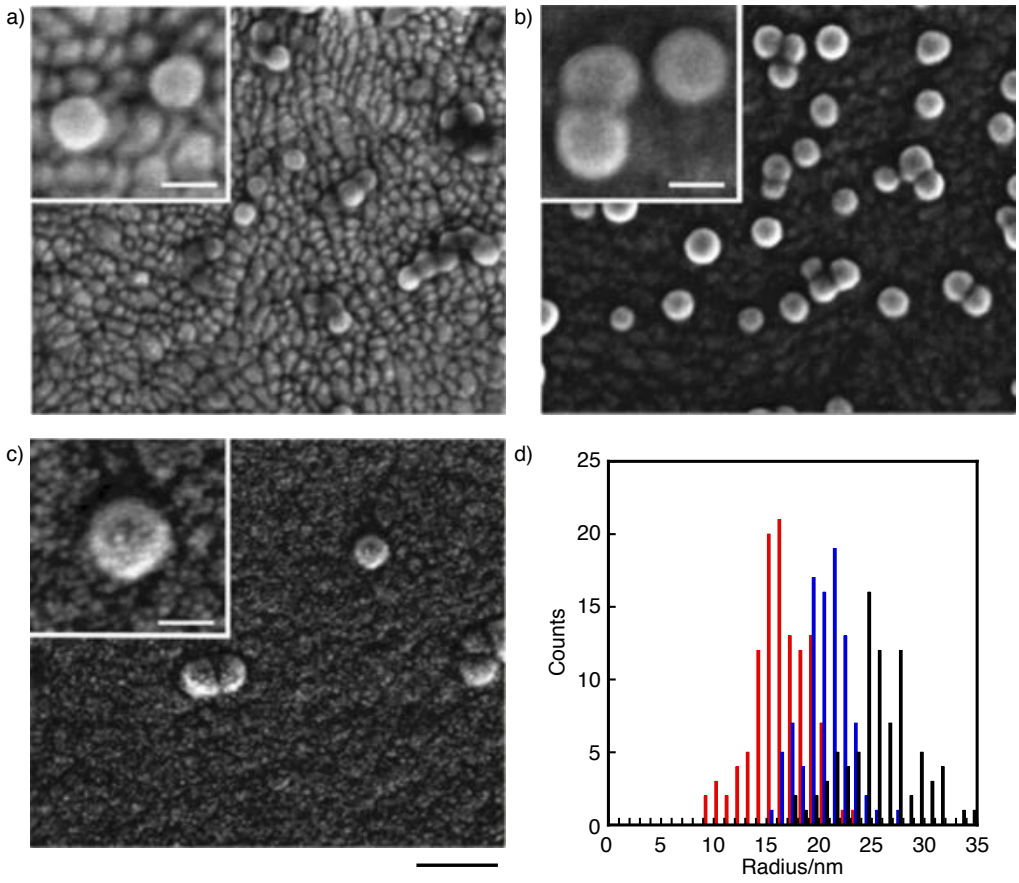

Figure 4-8. SEM images of avidin-coated fullerene vesicles on glass/ITO substrate. a) The image of vesicles without metallic coating. b) The images of vesicles after deposition of Pt/Pd with the thickness of 1 nm. c) Vesicles after deposition of Pt/Pd with the thickness of 5 nm. Particles of the alloy are clearly observed on the vesicles and ITO grains. Scale bar is 100 nm. Inset: magnified images of the individual vesicles. d) Histogram of the number of the avidin-coated vesicles plotted against the radius of the vesicles in SEM. Red, intact vesicle (N = 116); Blue, 1 nm coating of Pt/Pd (N = 93); Black, 5 nm coating of Pt/Pd (N = 85).

On the superhydrophilic ITO substrate (treated by UV/ozone just before use, water contact angle of 0°), the vesicles can be observed individually. However, on the hydrophobic Si/SiO_2 surface (contact angle of 70°), the vesicles the vesicles aggregated and fused extensively (Figure 4-9), and could not be coated on gold or HOPG substrates.

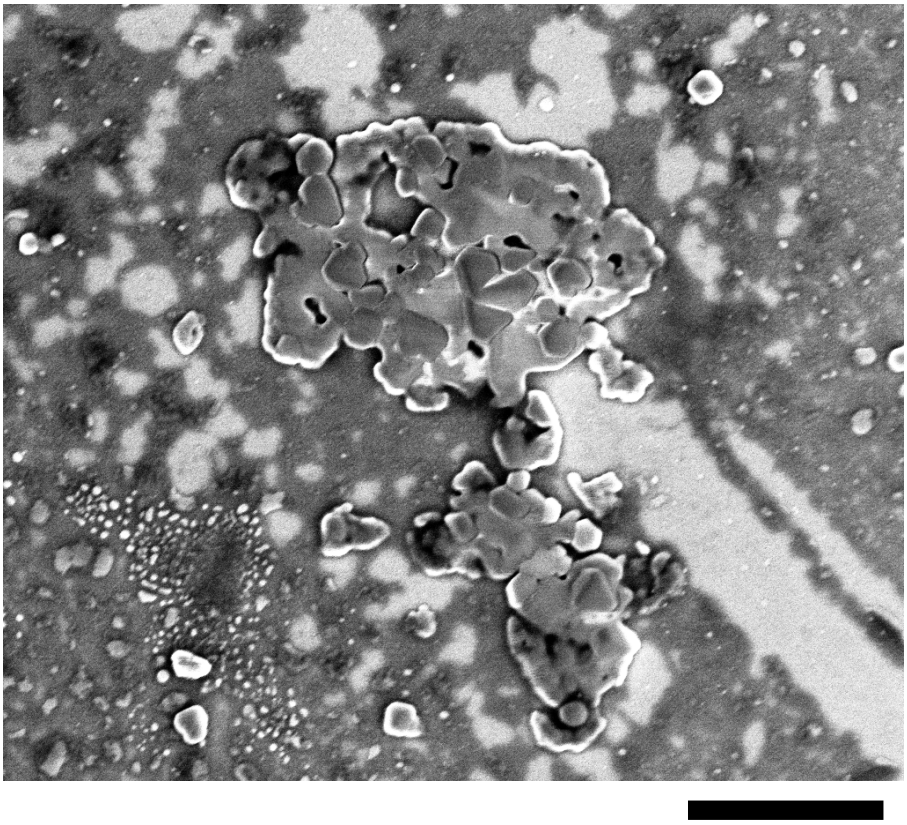

Figure 4-9. SEM image of a huge aggregate of avidin-coated vesicles on a silicon substrate.

Figure 4-10 showed the vesicles on the ITO/glass substrate using the state-of-the-art SEM imaging. The avidin vesicle can be clearly observed by SEM, whereas the **C8(7Y)K** vesicle and the biotinylated vesicle on ITO were found that they are far less stable than the avidin vesicle. The **C8(7Y)K** vesicles showed only a very small number of the spherical objects, and instead many dark flat spots on ITO microcrystal (Figure 4-10a; see also Figure 4-14). The electron diffraction X-ray (EDX) analysis revealed the presence of carbon atoms, and hence I concluded that they are collapsed vesicles. In contrast, the **C8(7Y)K** vesicles on a carbon film under STEM conditions were much more stable, and AFM analysis under ambient pressure and temperature on mica showed no trace of decomposition (Figure 4-2). Similarly, the biotinylated vesicles showed many flat stains and spherical objects (Figure 4-10b; see also Figure 4-15). On

the other hand, the avidin vesicles were uniformly distributed on the microcrystalline surface of the ITO substrate and each vesicle was clearly imaged (Figure 4-10c; see also Figure 4-16). The much higher stability of the avidin vesicle compared with the **C8(7Y)K** and biotinylated vesicles suggests that the avidin molecules on the surface cross-linked underlying fullerene molecules through multidentate binding with the biotin groups.

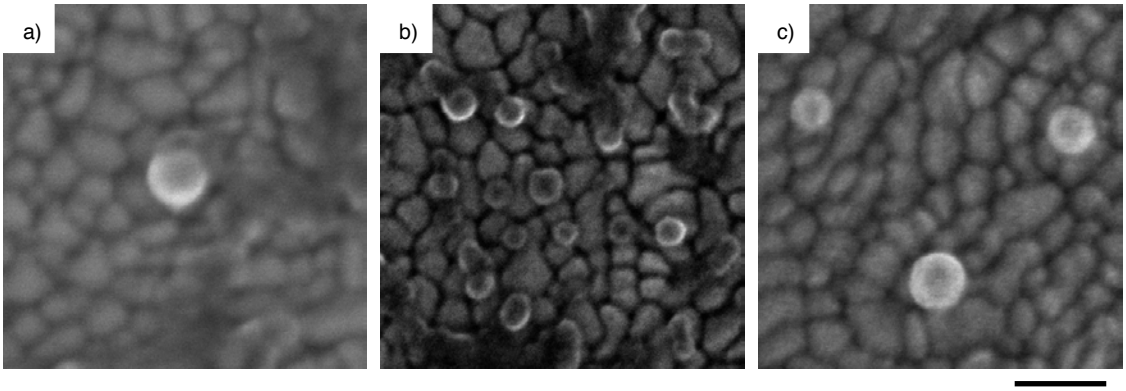

Figure 4-10. SEM images of **C8(7Y)K** vesicles. a) **C8(7Y)K** vesicle. b) Biotin-**C8(7Y)K** vesicle. c) Avidin vesicle. Scale bar is 50 nm.

I analyzed the average radius of the biotin-**C8(7Y)K** and avidin vesicles from SEM images, and the **C8(7Y)K** vesicle from STEM images. The average radii determined from hundreds of the **C(7Y)K**, biotin and avidin vesicles were 7.6 ± 1.4, 11.7 ± 1.6 and 15.5 ± 2.7 nm, respectively (Figure 4-11). The average radii of the **C8(7Y)K** and biotin vesicles from STEM/SEM are good agreement with the DLS data (Figure 4-6). In addition, the average radius increased by 3.8 nm after addition of avidin, which roughly corresponds to the size of an avidin molecule (ca. 5 nm) minus the depth of the biotin binding pocket (1.5 nm, Figure 4-11b).[18] These results indicate that the biotin moieties on the surface of the biotinylated vesicle were recognized by avidin to obtain the avidin-coated fullerene vesicle.

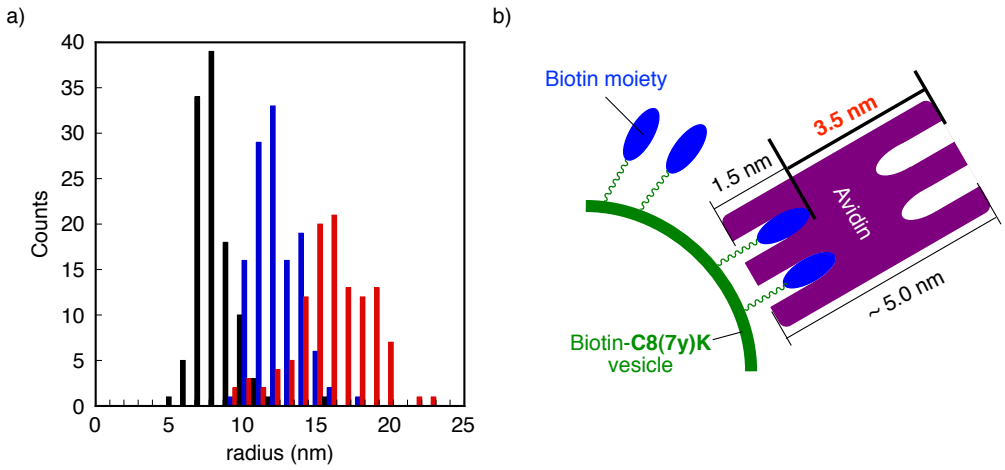

Figure 4-11. Size distribution of **C8(7Y)K** vesicles. a) Histogram of average radii obtained from STEM and SEM. **C8(7Y)K** (STEM), biotin-**C8(7Y)K** (SEM) and avidin-coated vesicles (SEM) are showed black, blue and red bars, respectively. b) Schematic illustration of avidin-coated **C8(7Y)K** vesicle.

The low acceleration voltage prevents charging of the specimen, produced nanometer-resolution images of the vesicles without metal coating and hence gave us information on the surface structure of the avidin-coated vesicle, which cannot be obtained either by TEM on a carbon film or AFM measurement on a mica surface. Thus, the vesicle images obtained after the first few scans (ca. 3 min at a beam current of 25 pA) caused a change in the surface structure (e.g., dehydration of protein), which now shows as bright and protruded areas, and dark areas (Figure 4-12a, b). The histogram of the bright areas that can be analyzed largely from the top of the vesicle (Figure 4-12b, circled in red) showed two peaks at 30–45 and 65–75 nm^2 (Figure 4-12c). The former is close to the projection area of a single molecule of avidin, which is 25–30 nm^2,[19] and the latter to that of two molecules. Therefore, I consider that the bright areas are due to individual avidin molecules. From these data, we can estimate that at least ca.20 avidin molecules are attached to the surface of the biotinylated **C8(7Y)K** vesicle.

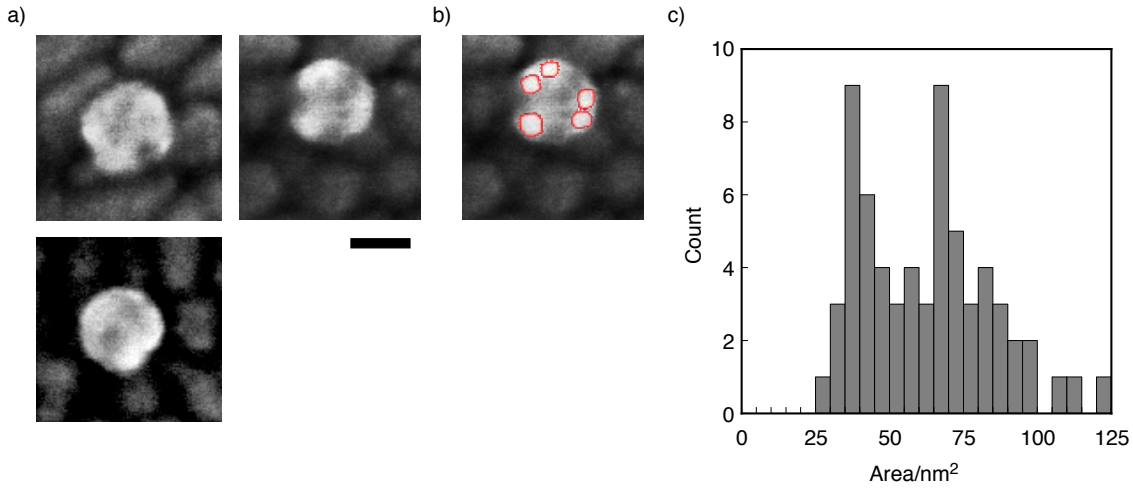

Figure 4-12. SEM images of avidin–biotin–**C8(7Y)K** conjugated vesicles. a) the image of vesicles taken after scanning at 25 pA for 3 min. Scale bar is 20 nm. b) The vesicle in ***Figure 4-12***a right, where bright areas are highlighted in red. c) Histogram for the 62 bright areas on 36 avidin–biotin–**C8(7Y)K** vesicles.

4.4. Application of fullerene vesicle for drug delivery system

4.4.1 Preparation of DOX-encapsulated vesicle

Finally, I describe application of the **C8(7Y)K** vesicle for drug delivery to a cancer cell.[20] I prepared the doxorubicin (DOX)-encapsulated vesicle as followed the procedure described above (Scheme 4-5). I added 5.0 μmol of **C8(7Y)K** in THF to an aqueous solution containing 5.3 μmol of DOX to form the DOX-containing vesicle, attached the biotin groups by a click reaction and separated the vesicles from excess DOX and copper reagents, etc. by chromatography.

Scheme 4-5. Preparation of DOX-encapsulated **C8(7Y)K** vesicle. a) Schematic illustration of DOX-encapsulated vesicle. b) Structure of doxorubicin (DOX).

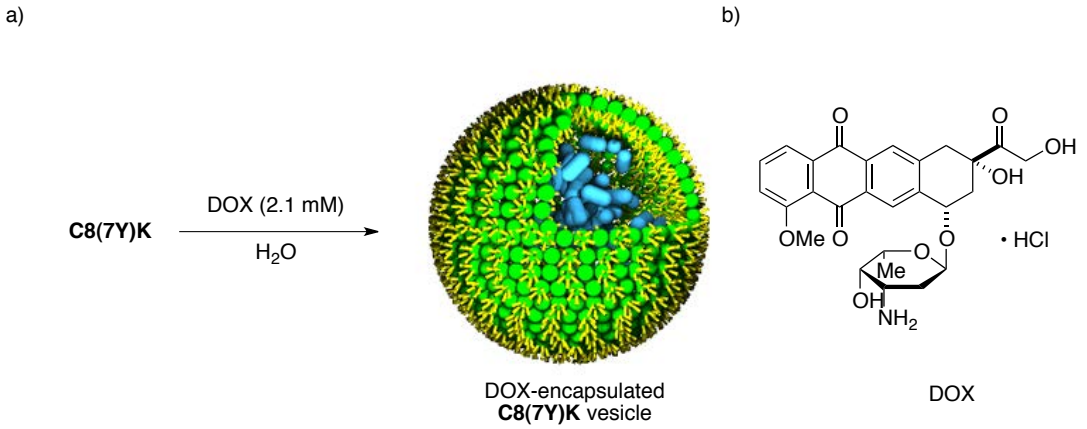

4.4.2 Anticancer drug delivery in vitro

I incubated this vesicle solution, which contains 2.5 pmol of DOX (25 nM if homogeneously dissolved in the medium), together with human liver carcinoma cells (HepG2) for 48 h. I measured the cell viability by MTT assay, and observed a cell viability of 67 ± 7% (Figure 4-13a). In contrast, the biotin vesicles free of DOX showed a cell viability of 93 ± 3%, and the 25 nM solution of DOX without vesicle encapsulation showed a cell viability of 93 ± 3% (IC_{50} value of 3.4 μM determined under the same conditions, Figure 4-13b; see also 4.6 Experimental section).

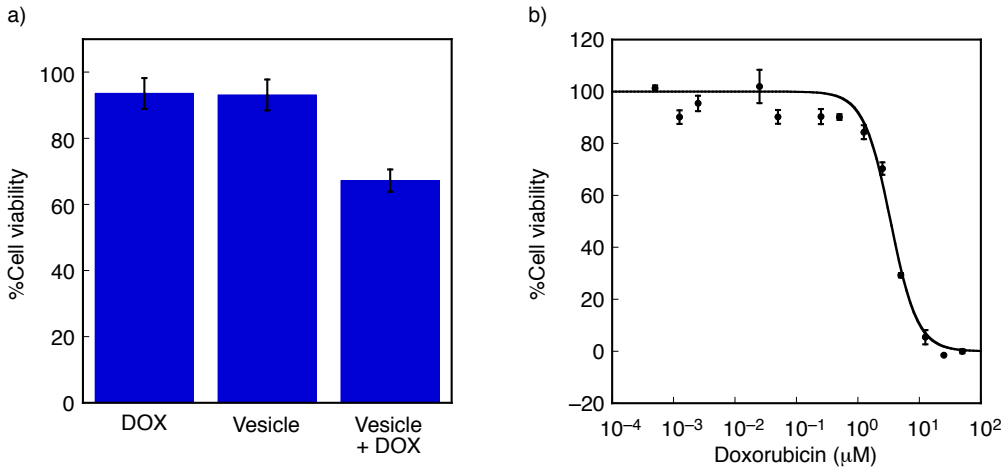

Figure 4-13. Delivery of anticancer drug by biotinylated **C8(7Y)K** vesicle. a) Cell viability. DOX, 25 nM of free DOX; Vesicle, Biotin-**C8(7Y)K** vesicle; Vesicle + DOX, DOX-encapsulated vesicle. Error bars are SEM. b) Dose-dependent cytotoxicity of free DOX.

4.5. Conclusion

In summary, I have developed the post-functionalizable nanocapsules through stepwise covalent and noncovalent surface modifications. The alkynylated vesicle survives the conditions of the click reaction and chromatographic purification, and can be further noncovalently conjugated with avidin molecules. By placing the avidin-coated vesicles on a conducting and superhydrophilic ITO surface, I showed that the low-accelerating-voltage SEM is capable of detecting single avidin molecules on the vesicle. ITO/glass is frequently used in organic electronics research, but it has seldom been used for biological imaging except for one report on micrometer-resolution SEM imaging of cultured cell.[17] I found that the ITO substrate is useful for imaging individual objects that tend to aggregate in water. This unique ability of the SEM stems from the monochromatic electron source and low accelerating voltage that allowed probing the structure of the insulating objects without metal coating. Finally, using this well characterized capsule I also showed that

an anticancer drug can be encapsulated in the interior of the capsule and used for drug delivery.

4.6. Experimental section

General.

All reactions dealing with air- or moisture-sensitive compounds were carried out in a dry reaction vessel under nitrogen or argon. The water content of the solvent was confirmed with a Karl-Fischer Moisture Titrator (MKC-210, Kyoto Electronics Company) to be less than 10 ppm. Analytical thin-layer chromatography (TLC) was performed on glass plates coated with 0.25 mm 230–400 mesh silica gel containing a fluorescent indicator (Merck). Analysis with high performance liquid chromatography (HPLC) was performed on JASCO HPLC system equipped with an ODS column (Senshu PEGASIL ODS, 4.6 × 250 mm; column temperature at 40 °C) or a Bucky Prep column (Nacalai Tesque Cosmosil Bucky Prep, 4.6 × 250 mm; column temperature at 40 °C). Flash silica gel column chromatography was performed on silica gel 60N (Kanto, spherical and neutral, 140–325 mesh) as described by Still *et al*.[21] Gel permeation column chromatography was performed on a Japan Analytical Industry LC-908 (eluent: chloroform) with JAIGEL 1H and 2H polystyrene columns. Nuclear magnetic resonance (NMR) spectra were measured on JEOL ECX-400 and ECA-500 spectrometers and reported in parts per million from tetramethylsilane. ^{1}H NMR spectra in $CDCl_3$ were referenced internally to tetramethylsilane as a standard, and ^{13}C NMR spectra to the solvent resonance. (Methyl, methylene, and methyne signals in ^{13}C NMR spectra were assigned by DEPT spectra. Routine mass spectra were acquired by atmospheric pressure chemical ionization (APCI) using a quadrupole mass analyzer on Shimazu QP-8000, and high resolution spectra by APCI or electrospray ionization (ESI) using a time-of-flight mass analyzer on JEOL JMS-T100LC (AccuTOF) spectrometer with a calibration standard of polyethylene glycol (MW 1000). Distilled water was further deionized with Millipore Milli-Q. The dynamic laser

light scattering (DLS) study was carried out on a Malvern Zetasizer Nano ZS machine. The atomic force microscopy (AFM) measurement was performed on a JEOL JSPM-4200 with a silicon cantilever (NSC-35, resonant frequency 120–190 kHz). Scanning electron microscopy (SEM) with energy dispersive X-ray analysis (EDX) was performed on a FEI Magellan 400L equipped with AMETEK/EDAX Genesis APEX4. The scanning transmission electron microscopy (STEM) observations at 294 K were performed on a JEOL JEM-2100F with a spherical aberration coefficient Cs = 1.0 nm at an acceleration voltage of 200 kV under reduced pressure of 1.0×10^{-5} Pa in the sample column. The current density is ca. 0.5 $pA \cdot cm^{-2}$. The imaging instrument used was an ultrascan charge-coupled device (CCD) camera (512 × 512 pixels). The UV-Visible spectra were recorded on a JASCO V-570 UV/Vis/NIR Spectrophotometer. Fluorescence spectra were recorded on a HITACHI F-4500 Fluorescence Spectrophotometer.

Materials.

Unless otherwise noted, materials were purchased from Tokyo Kasei Co., Aldrich Inc., and other commercial suppliers and used after appropriate purification before use. Anhydrous ethereal solvents (stabilizer-free) were purchased from WAKO Pure Chemical and purified by a solvent purification system (GlassContour)[22] equipped with columns of activated alumina and supported copper catalyst (Q-5) prior to use. All other solvents were purified by distillation and stored over molecular sieves 4Å. 1-Bromo-4-(6-iodohexyl)benzene **2**,[23] 7-hydroxy-3-azidocoumarin **4**[14] and azido-biotin **biotin-N$_3$**[16] were synthesized according to the reported procedure.

[8-(4-Bromophenyl)oct-1-ynyl]tri(1-methylethyl)silane (3).

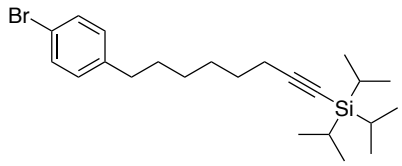

To a solution of triisopropylacetylene (1.00 g, 5.49 mmol; 2.0 eq) in THF (4 mL) was added dropwise *n*-butyl lithium in hexane (1.60 M, 3.74 mL, 5.99 mmol; 2.2 eq) at 0 °C. After stirring for 30 min, the reaction mixture was added dropwise to a solution of 1-(4-bromophenyl)-6-iodohexane **2** (996 mg, 2.71 mmol) in 1,3-dimethyltetrahydro-2(1*H*)-pyrimidone (4 mL) at 0 °C. The reaction was monitored by TLC. After stirring for 70 min, the reaction mixture was poured into ice-cold water. The organic layer was extracted three times with pentane (20 mL). The combined extracts were washed twice with brine (15 mL), dried over anhydrous magnesium sulfate, and concentrated under reduced pressure. The crude material (1.68 g) was purified by flash column chromatography on silica gel (85 g, eluent: hexane) to give the title compound (830 mg, 73%) as pale yellow oil: IR (neat) 2936, 2826, 2172, 1488, 1462, 1243, 1072, 1012, 995, 919, 883, 797, 676, 661, 622 cm^{-1}; ^{1}H NMR (500 MHz, $CDCl_3$) δ 0.88–1.09 (m, 21H), 1.29–1.36 (m, 2H), 1.41–1.62 (m, 6H), 2.24 (t, *J* = 6.9 Hz, 2H), 2.55 (t, *J* = 7.5 Hz, 2H), 7.04 (d, *J* = 8.6 Hz, 2H), 7.38 (d, *J* = 8.6 Hz, 2H); ^{13}C NMR (125 Hz, $CDCl_3$) δ 11.30, 18.64, 19.78, 28.42, 28.55, 28.68, 31.18, 35.21, 64.38, 80.13, 109.11, 130.15, 131.25, 141.69; Anal. Calcd for $C_{21}H_{37}BrSi$: C, 65.53; H, 8.85. Found: C, 65.53; H, 8.95.

6,9,12,15,18-Penta(4-{8-[tri(1-methylethyl)silyl]oct-7-ynyl}-phenyl)-1,6,9,12,15,18-hexahydro(C_{60}-I_h)[5,6]fullerene (5).

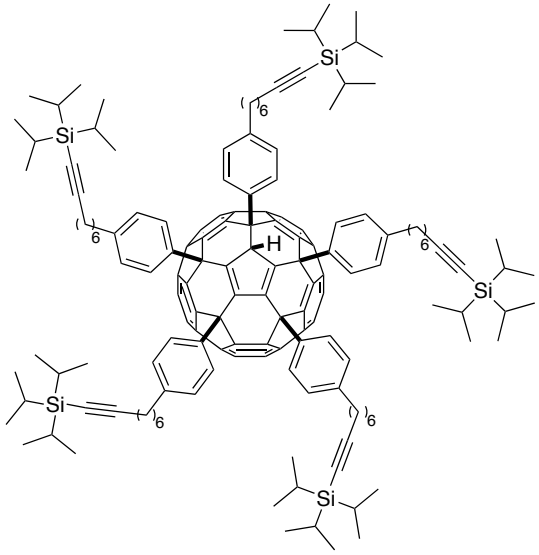

0.16 M of 4-[8-(triisopropyl)oct-7-ynyl]phenyl magnesium bromide in THF (8.0 mL, 1.90 mmol, 0.23 M; 12 eq), prepared from [8-(4-bromophenyl)oct-1-ynyl]tri(1-methylethyl)silane **3**, magnesium and catalytic amount of 1,2-dibromoethane, was added to a solution of CuBr•SMe_2 (390 mg, 1.90 mmol; 12 eq) in THF (1.0 mL) at 35 °C. After stirring for 10 min, a solution of [60]fullerene (120 mg, 0.158 mmol) in 1,2-dichlorobenzene (8 mL) was added to the reaction mixture. The reaction was monitored by HPLC (Buckyprep, eluent: 30% 2-propanol/toluene). After stirring for 50 min, the reaction was quenched with sat. aq. NH_4Cl (0.5 mL). The reaction mixture was filtrated through a pad of silica gel eluted with carbon disulfide to remove copper salts, and then was concentrated under reduced pressure. Since isolation of the target compound by reprecipitation and chromatographic methods were unsuccessful due to low crystallinity and polarity, the crude material containing 1,2-dichlorobenzene (9.55 g) was used for the next deprotection reaction without further purifications: ^{1}H NMR (500 MHz, $CDCl_3$) δ 0.95–1.08 (m, 105H), 1.20–1.67 (m, 40 H), 2.22–2.28 (m, 10H), 2.54 (t, *J* = 7.5 Hz, 2H), 2.59 (t, *J* = 7.5 Hz, 4H), 2.65

(t, *J* = 7.5 Hz, 4H), 5.24 (s, 1H), 6.94 (d, *J* = 8.0 Hz, 2H), 6.98 (d, *J* = 8.0 Hz, 4H), 7.11 (d, *J* = 8.0 Hz, 4H), 7.32 (d, *J* = 8.0 Hz, 2H), 7.49 (d, *J* = 8.0 Hz, 4H), 7.66 (d, *J* = 8.0 Hz, 4H).

6,9,12,15,18-Penta[4-(oct-7-ynyl)phenyl]-1,6,9,12,15,18-hexahydro-(C_{60}-I_h)[5,6]fullerene (C8(7Y)H).

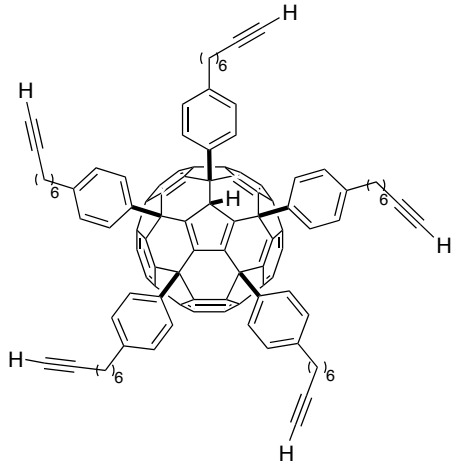

To a solution of 6,9,12,15,18-penta{4-[(8-triisopropylsilyl)oct-7-ynyl]-phenyl}-1,6,9,12,15,18-hexahydro(C_{60}-I_h)[5,6]fullerene **5** (76.5 mg, 31.5 μmol) in THF (4 mL) was added 1 M of Bu_4NF in THF (0.315 mL, 315 μmol; 10 eq). After addition, the reaction mixture was started refluxing. The reaction was monitored by MS. After stirring for 1.5 h, the reaction mixture was slowly added into methanol (50 mL) to obtain orange precipitate. The precipitate was collected by filtration, washed with methanol, and dried under reduced pressure to give the title compound (45.9 mg, 88%) as an orange solid: IR (powder) 2929, 2856, 2363, 2342, 1719, 1509, 1093, 1017, 625 cm^{-1}; ^1H NMR (500 MHz, $CDCl_3$) δ 1.25–1.70 (m, 40H), 1.92–1.96 (m, 5H), 2.14–2.22 (m, 10H), 2.54 (t, *J* = 7.5 Hz, 2H), 2.59 (t, *J* = 7.5 Hz, 4H), 2.65 (t, *J* = 7.5 Hz, 4H), 5.23 (s, 1H), 6.92 (d, *J* = 8.6 Hz, 2H), 6.97 (d, *J* = 8.6 Hz, 4H), 7.11 (d, *J* = 8.6 Hz, 4H), 7.30 (d, *J* = 8.6 Hz, 2H), 7.48 (d, *J* = 8.6 Hz, 4H), 7.65 (d, *J* = 8.6 Hz, 4H); ^{13}C NMR (100 MHz, $CDCl_3$) δ 18.38, 18.43, 18.46, 28.40, 28.46, 28.46, 28.55, 28.56, 28.58, 28.60, 28.63,

28.67, 31.18, 31.25, 31.26, 35.32, 35.36, 35.40, 58.64, 58.72, 60.77, 62.97, 68.20, 68.24, 68.25, 77.21, 84.59, 84.62, 127.70, 127.99, 128.10, 128.19, 128.37, 128.57, 128.65, 128.83, 137.18, 137.24, 141.55, 141.80, 142.07, 143.08, 143.19, 143.86, 144.00, 144.08, 144.20, 144.29, 144.31, 144.55, 145.48, 145.75, 146.00, 146.27, 146.87, 147.06, 147.17, 147.69, 147.98, 148.03, 148.21, 148.35, 148.63, 148.69, 151.81, 152.40, 152.56, 156.26; HRMS (APCI+) calcd for $C_{130}H_{86}$ [M]$^+$ 1648.6842, found 1648.6823.

Preparation of C8(7Y)K vesicle.

The vesicle solution used for this study was prepared as reported:[4] *t*BuOK in THF (1.00 M, 74 μL, 75 μmol, 1.5 eq) was added to a solution of **C8(7Y)H** (82.4 mg, 50 μmol) in THF (3.93 mL) and mixture was stirred under argon. After stirring for 3 h, a portion of the solution of **C8(7Y)K** (12.5 mM, 0.80 mL, 10 μmol) was slowly injected into ultrapure water (4.2 mL) with stirring at 400 rpm over 1 min using a syringe pump (ISIS Co.) to obtain a vesicle solution of **C8(7Y)K** (2.0 mM) in 16% THF/water. THF and water were removed by evaporation at ca. 7 kPa, and the final concentration of **C8(7Y)K** was adjusted to 2.0 mM. If it is necessary to obtain vesicle solution with narrower size distribution, the vesicle solution was centrifuged (TOMY MC-150) at 15,000 rpm for 30 min, and the supernatant was collected. The concentration of **C8(7Y)K** was determined to be 1.5 mM by UV spectra at 352 nm of wavelength. The diameter of the vesicles may vary in the range of 18–32 nm, depending on the conditions of the preparation.

Fluorescence analysis of Cu(I)-catalyzed Huisgen cycloaddition reaction.

Stock solutions of 7-hydroxy-3-aidocoumarin **4** (2.5 mM), copper(II) sulfate (0.40 mM), (+)-sodium ascorbate (0.80 mM), and triethylamine (4.0 mM) was prepared in ultrapure water. 2.0 mM of **C8(7Y)K** or **C8K**[4] vesicle in water (2.5 μL) was added to a solution of 7-hydroxy-3-azidocoumarin **4** (10.0 μL, 25

nmol; 5.0 eq), copper(II) sulfate 6.25 μL, 2.5 nmol; 50 mol%), (+)-sodium ascorbate (6.25 μL, 5.0 nmol; 1.0 eq) and triethylamine (6.25 μL, 25 nmol; 5.0 eq) in distilled-deionized water (5.0 mL) at room temperature in a 1.0 × 1.0 x 4.0 cm^3 quartz cuvette. Time-dependent fluorescent intensities were measured at excitation wavelength (λ_{ex}) of 490 nm at 25 °C, and monitored at emission wavelength (λ_{em}) of 530 nm with the slit width of 5 nm.

Preparation of biotinylated C8(7Y)K vesicle.

Biotinylated fullerene vesicle was prepared using Cu(I)-catalyzed Huisgen [3 + 2] cycloaddition reaction of azido-biotin with alkynyl fullerene vesicle. Stock solutions of **biotin-N**$_3$ (0.10 mM), copper(II) sulfate (0.010 mM), (+)-sodium ascorbate (0.060 mM), and triethylamine (0.10 mM) in distilled-deionized water was prepared. Alkynyl fullerene vesicle (1.5 mM, 400 μL, 0.60 μmol) was added slowly with stirring to a solution of **biotin-N**$_3$ (30 μL, 0.30 nmol; 5.0 equiv.), copper(II) sulfate (30 μL, 0.30 nmol; 0.50 equiv.), (+)-sodium ascorbate (10 μL, 0.60 nmol; 1.0 equiv.), and triethylamine (30 μL, 3.0 nmol; 5.0 equiv.) at room temperature. After stirring for 6 days, the reaction mixture was passed through a column of Sephadex G-50 fine (GE healthcare Japan, Japan, ϕ 10 × 100 mm) to be separated with unreacted **biotin-N**$_3$, and orange-colored fractions in the eluted solution were collected and diluted with distilled-deionized water to 5.0 mL ([**C8(7Y)K**] = 0.12 mM). The size of biotinylated **C8(7Y)K** vesicle was determined by DLS analysis and SEM measurement.

Preparation of avidin-coated C8(7Y)K vesicle.

An aqueous solution of biotinylated **C8(7Y)K** vesicle (0.15 mM, 13.5 μL, 2.0 nmol) was added to avidin (1.9 nmol) in phosphate buffered saline (100 μL) and mixed gently by a pipette at room temperature for 1 min. The size of vesicle

aggregates in solution was analyzed by DLS. For SEM measurement, the solution was diluted to 50 μM (as the concentration of **C8(7Y)K**) and subjected to SEM sample preparation described below.

DLS analyses.

DLS measurement was performed on a Malvern Zetasizer Nano ZS equipped with an He-Ne laser operating at 4 mW power and 633 nm wavelength, and a computer-controlled correlator, at a 173° accumulation angle. Measurement was carried out at room temperature in a polystyrene or glass cuvette. The data were processed using dispersion technology software version 4.10 to give Z-average particle size and polydispersity index (PDI) value by cumulant analysis, and particle size distribution by CONTIN analysis.[24]

SEM measurement.

SEM measurement was conducted on a FEI Magellan 400L. An aqueous solution of the vesicles (50 μM, 20 μL) was placed on a ITO/glass substrate cleaned by UV/ozone treatment just before use, and was spin-coated (1500 rpm) for 30 s. After drying under reduced pressure (5×10^{-2} Pa) for 10 min, the ITO substrate was subjected to the SEM observation at an acceleration voltage of 1–8 kV under a vacuum of 5×10^{-5} Pa without any conductive coatings. We took most of the images at low acceleration voltage of 1–2 kV for higher resolution (Figure 4-14, Figure 4-16–

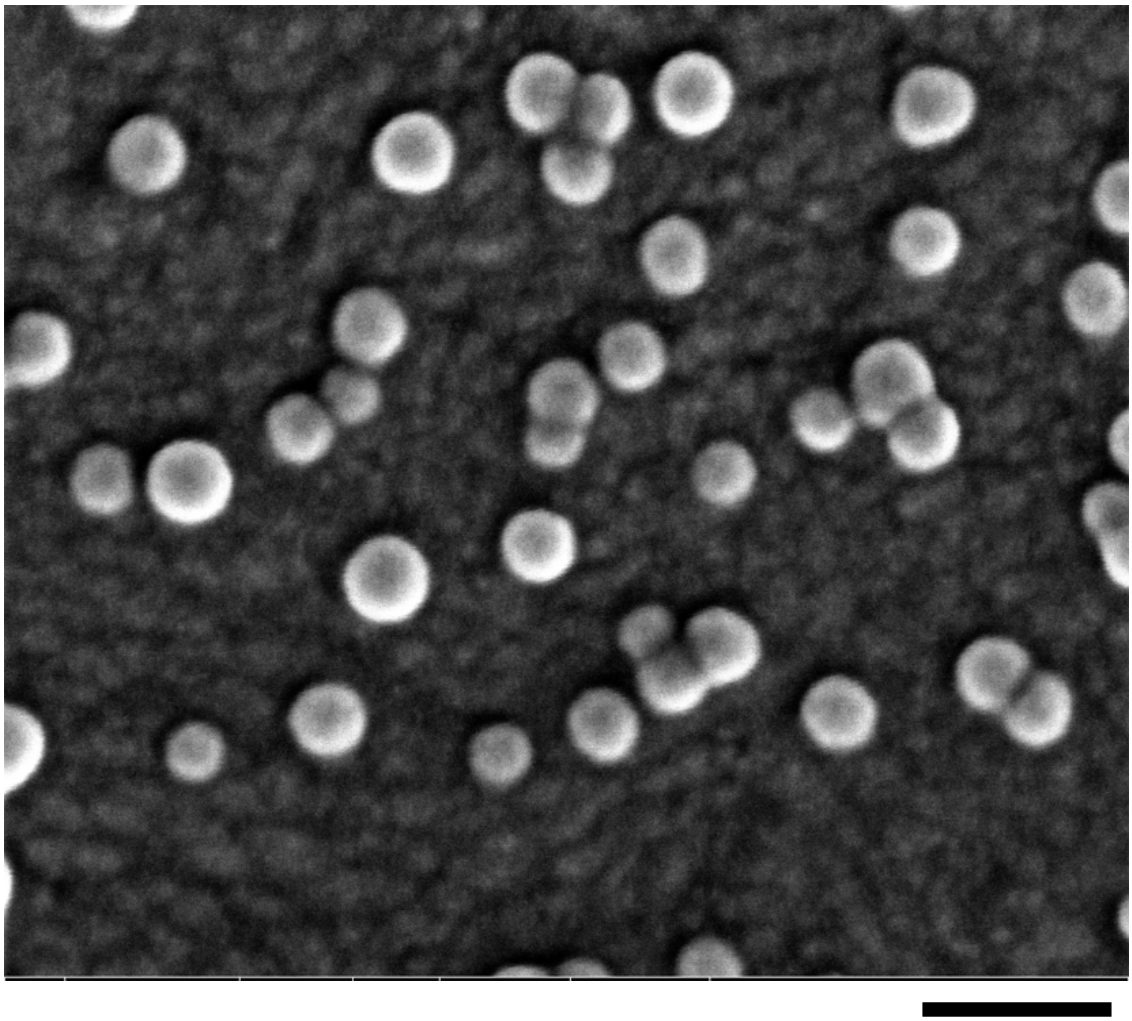

Figure 4-19), but when the size of the vesicles were small and comparable to the size of ITO grains, we applied higher acceleration voltage of 8 kV so that the spherical shape of the small vesicle particles were highlighted obviously (Figure 4-15).

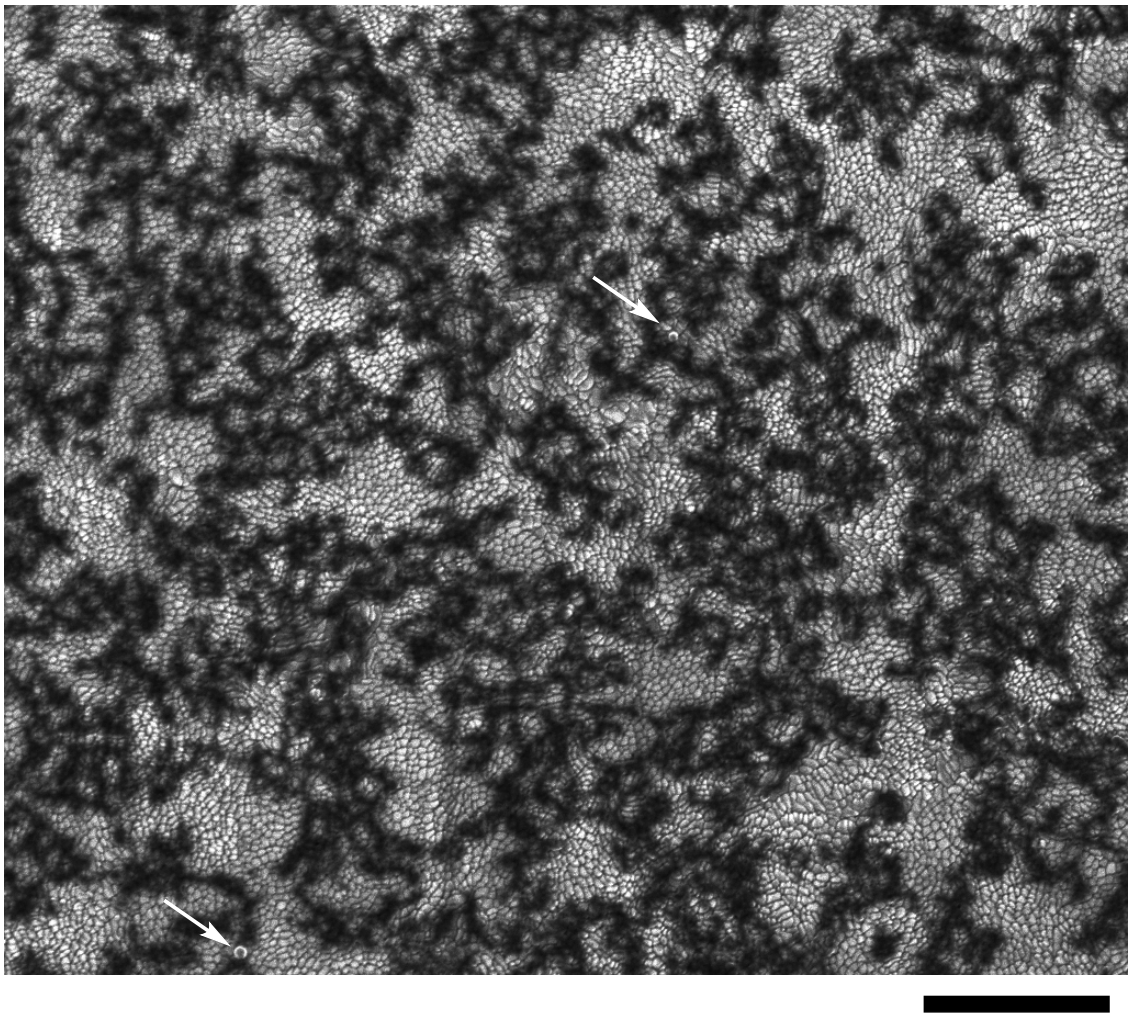

Figure 4-14. SEM image of C8(7Y)K vesicle on ITO taken at acceleration voltage of 2 kV and current intensity of 25 pA. Arrows indicate the vesicle. Scale bar is 500 nm.

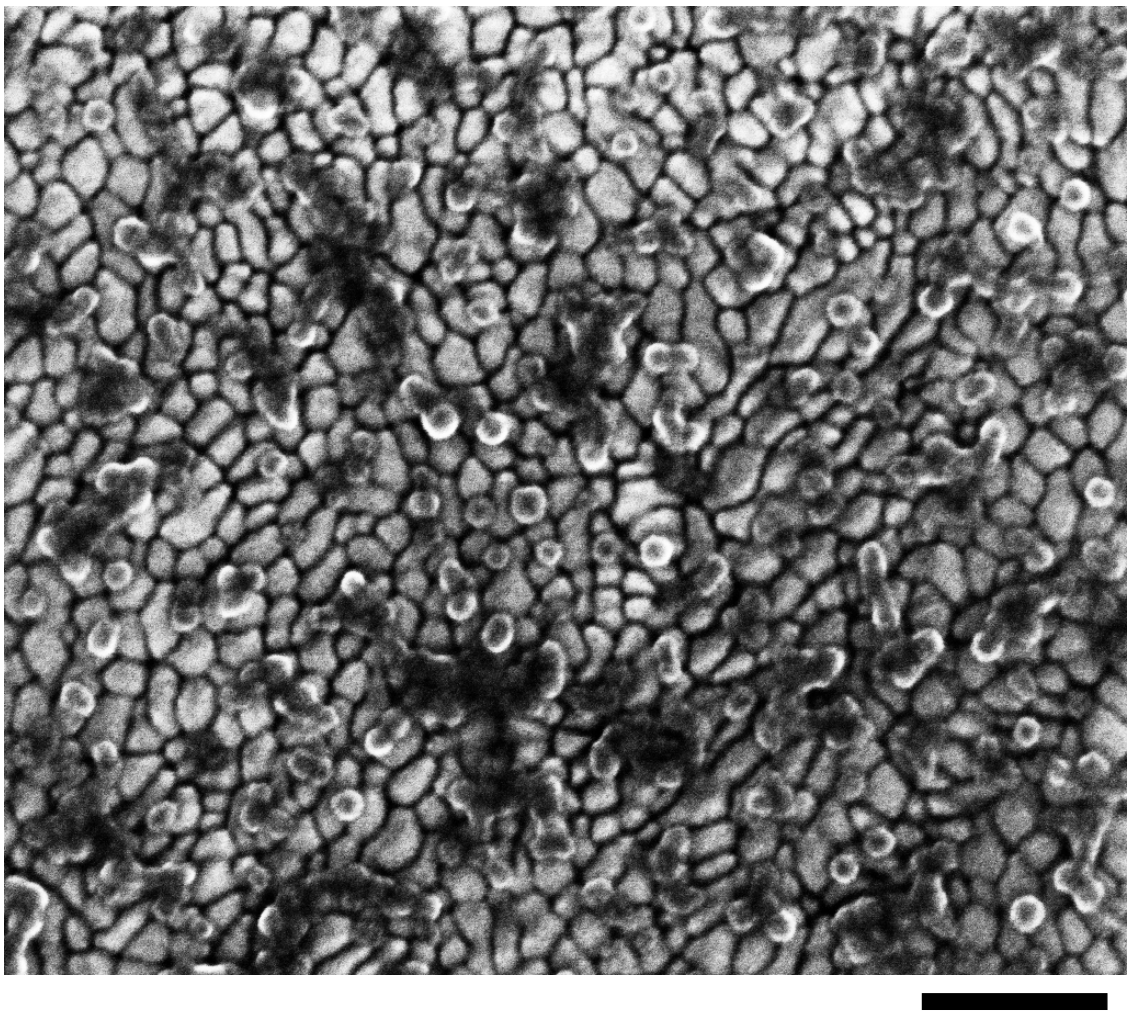

Figure 4-15. SEM image of biotinylated C8(7Y)K vesicle on ITO taken at acceleration voltage of 8 kV and current intensity of 50 pA. Scale bar is 100 nm.

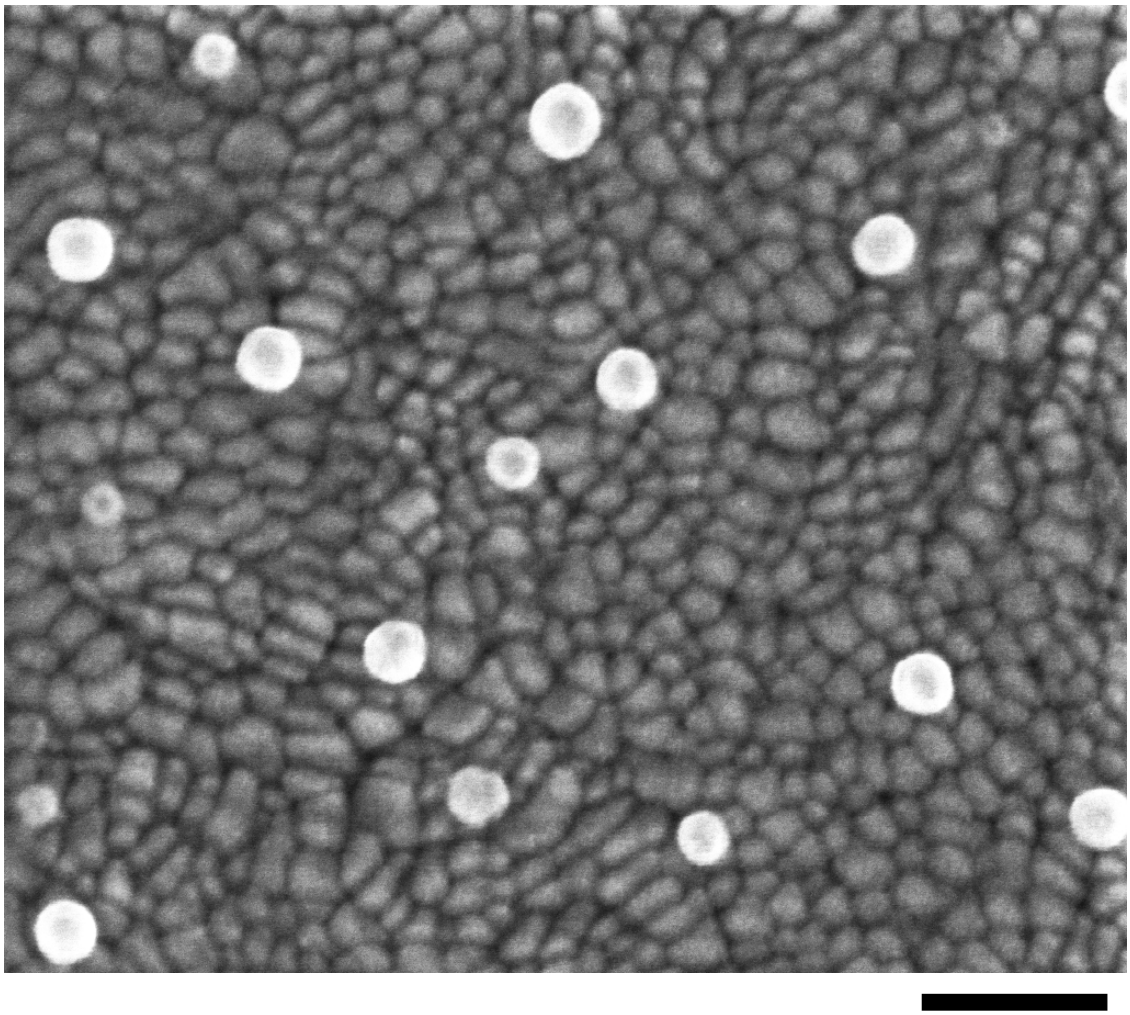

Figure 4-16. SEM image of avidin-coated vesicles on ITO taken at acceleration voltage of 2 kV and current intensity of 25 pA. This image was obtained from the first scan of this area (i.e. least effect on the specimen by electron irradiation). Scale bar is 100 nm.

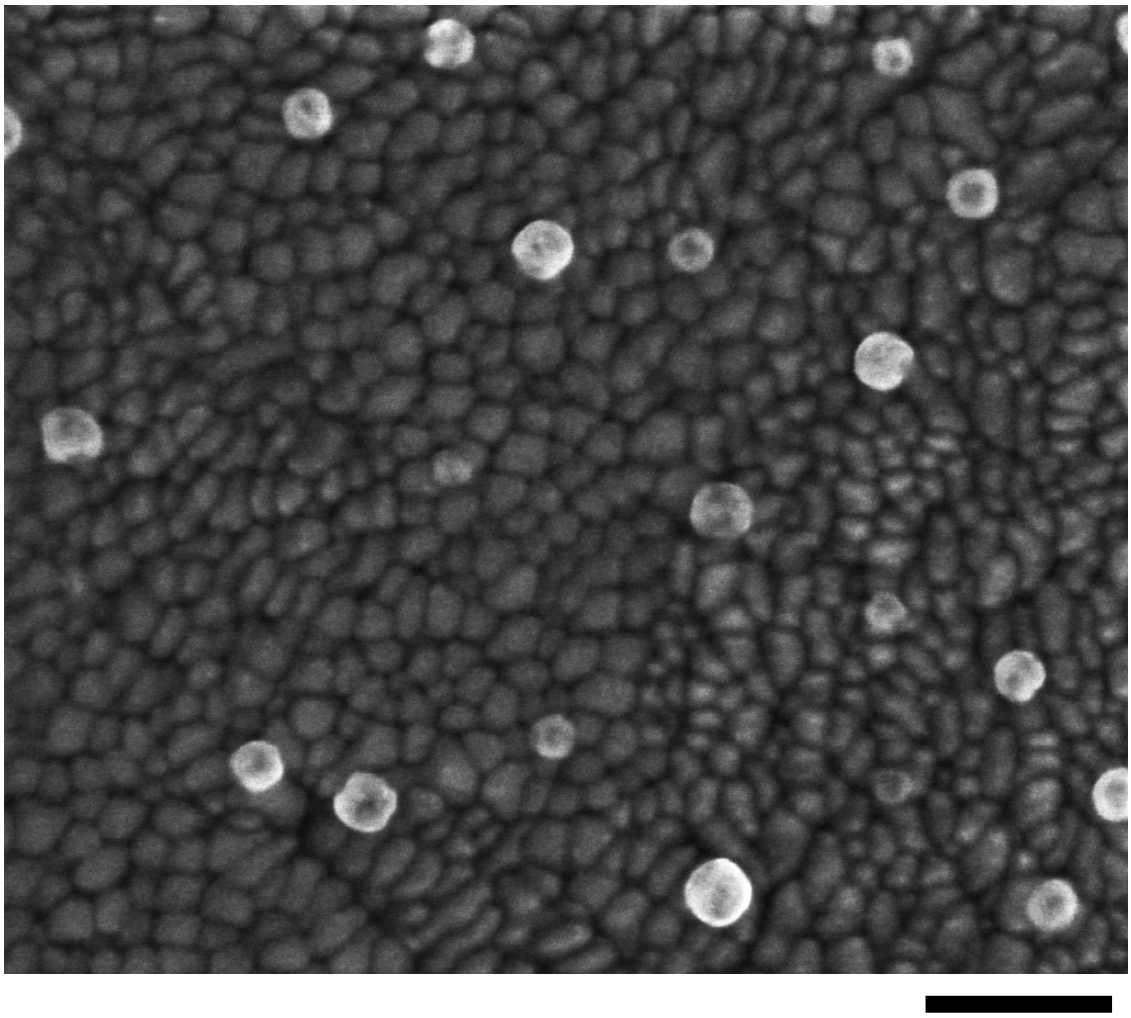

Figure 4-17. SEM image of avidin-coated vesicles, showing fine structure on their surfaces. This image was taken at acceleration voltage of 2 kV and current intensity of 25 pA and obtained after a few scans (3 minutes in total). Scale bar is 100 nm.

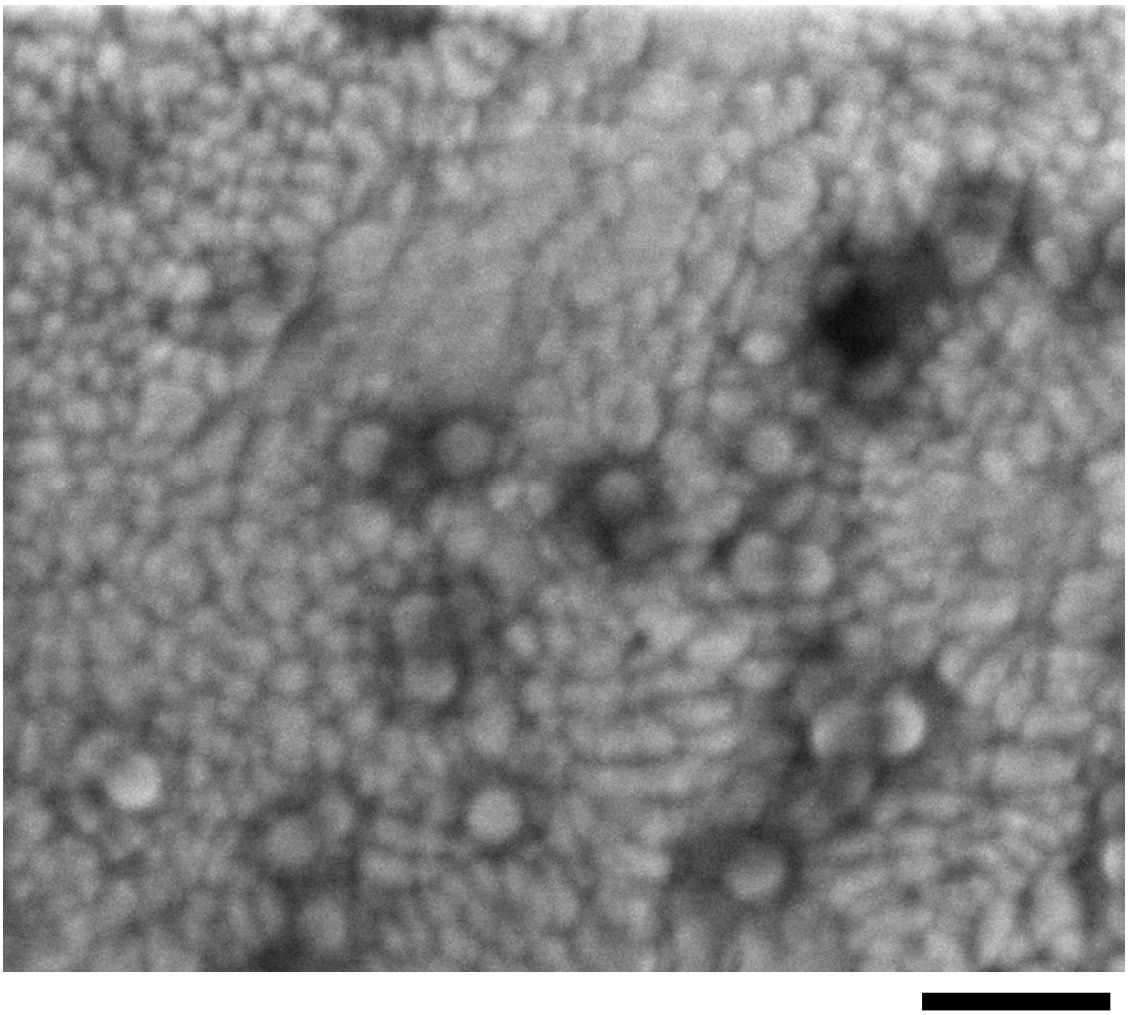

Figure 4-18. SEM image of avidin-coated vesicles with 1 nm Pt/Pd metal coating on ITO taken at acceleration voltage of 1 kV and current intensity of 12.5 pA. WD is 4 mm. Scale bar is 100 nm.

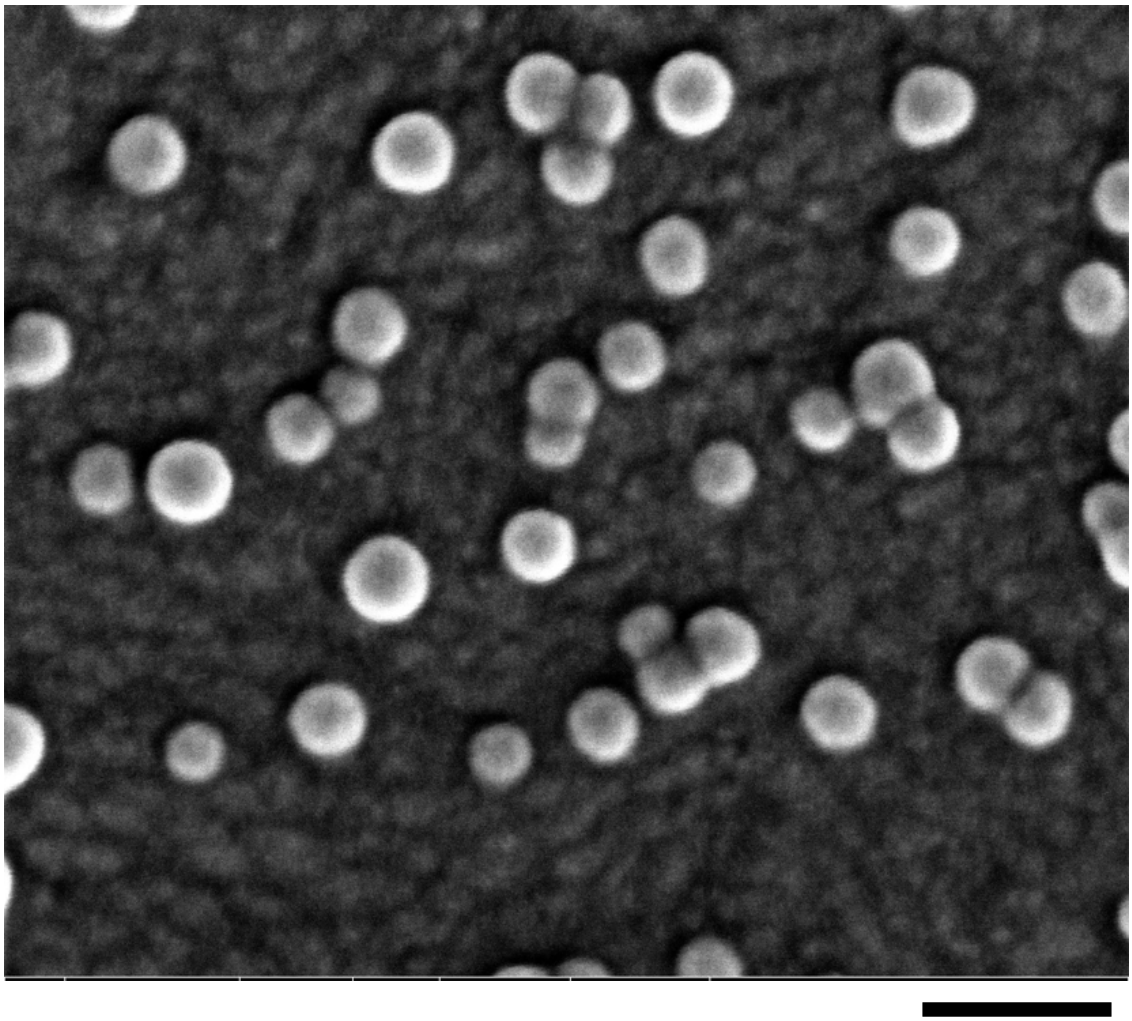

Figure 4-19. SEM image of avidin-coated vesicles with 1 nm Pt/Pd metal coating on ITO taken at acceleration voltage of 1 kV and current intensity of 12.5 pA. Scale bar is 100 nm.

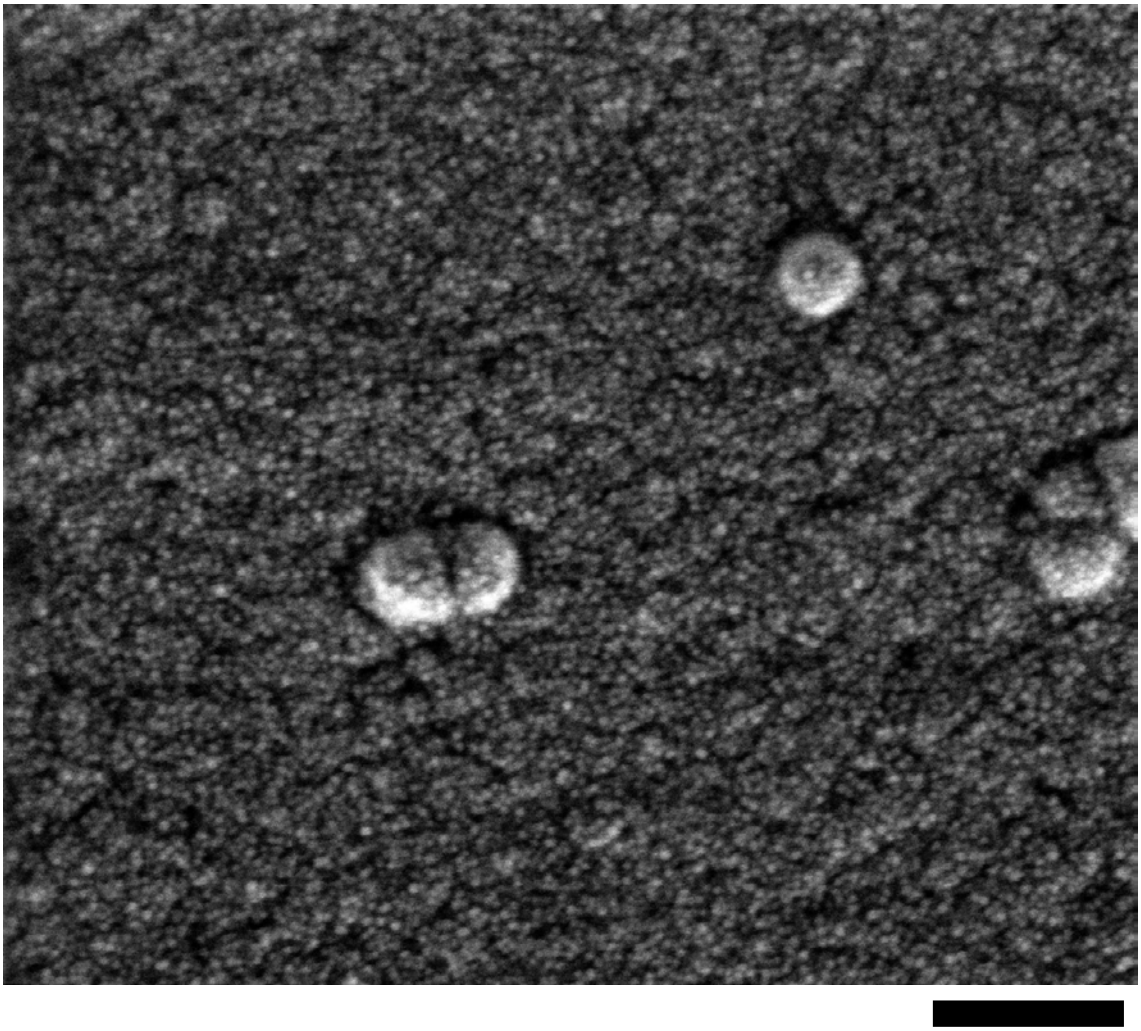

Figure 4-20. SEM image of avidin-coated vesicles with 5 nm Pt/Pd metal coating on ITO taken at acceleration voltage of 1 kV and current intensity of 12.5 pA. Scale bar is 100 nm.

AFM measurement.

AFM measurement was conducted on a Bruker MultiMode 8. Aqueous solution of the **C8(7Y)K** vesicle (2.0 mM, average diameter of 18.4 nm determined by DLS) were deposited on a mica substrate (5 × 5 mm^2) in aliquot of 2 μL under air. After drying the sample by blowing air for 10 sec and under reduced pressure (5 × 10^{-2} Pa), the AFM images were obtained by AC mode measurement. The observed width of the vesicles was 20–25 nm, which is 4 to 9 nm larger than that in SEM due to curvature of an AFM tip (ca. 2 nm radius of curvature).

STEM measurement.

STEM measurement was conducted on a JEOL JEM-2100F at 294 K with a spherical aberration coefficient Cs = 1.0 nm at an acceleration voltage of 200 kV under reduced pressure of 1.0 × 10^{-5} Pa in the sample column. The current density is ca. 0.5 pA·cm^{-2}. The imaging instrument used was an ultrascan charge-coupled device (CCD) camera (512 × 512 pixels). 50 μM of **C8(7Y)K** vesicle (2 μL) was deposited on a transmission electron microscopy (TEM) copper mesh coated with carbon film (Super Ultra High Resolution Carbon film, thickness < 6 nm, Oken Shoji Co., Ltd.), then dried under reduced pressure (4 × 10^{-2} Pa) at room temperature for 18 h.

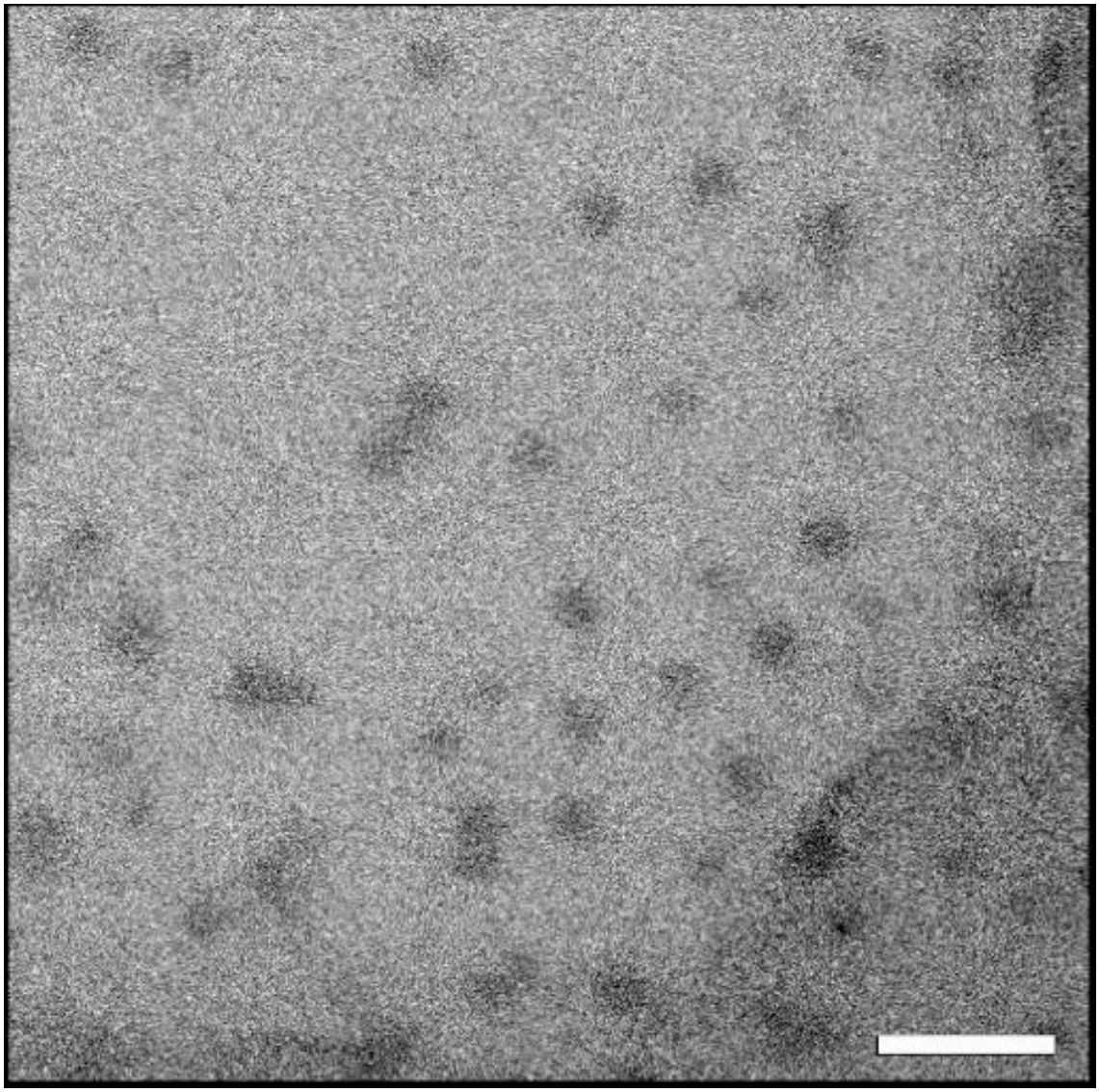

Figure 4-21. STEM image of **C8(7Y)K** vesicle on a carbon film. Scale bar is 50 nm.

Encapsulation analysis

To a solution of **C8(7Y)H** (41.2 mg, 25 μmol) in THF (4.0 mL) was added 1.0 M of potassium *tert*-butoxide in THF (75 μL, 75 μmol) at room temperature. After stirring for 3 h, the portion of the reaction mixture of **C8(7Y)K** (6.3 mM, 0.80 mL, 10 μmol) was slowly injected into a solution of 5(6)-carboxyfluorescein (3.76 mg, 10 μmol) and potassium hydroxide (3.37 mg, 60 μmol) in ultrapure water (4.2 mL) with stirring at 400 rpm for 1 min using a syringe pomp (ISIS CO.) to obtain **C8(7Y)K** vesicle (2.0 mM) in 16% THF/water. THF and water were removed by evaporation at ca. 7 kPa, and the final concentration of **C8(7Y)K** vesicle was adjusted to 2.0 mM. In order to remove the carboxyfluorescein, which was not encapsulated into the inner aqueous phase of the vesicle, 0.5 mL of vesicle solution was gel-filtered through a column of a Sephadex G-50 (GE Healthcare, Japan, ϕ 10 × 200 mm) and orange-colored fractions in the eluted solution were collected, and the solution was diluted with ultrapure water to 5.0 mL ([**C8(7Y)K**] = 0.20 mM).

0.60 mL of carboxyfluorescein-containing fullerene vesicle was added to water (9.4 mL), and fluorescent intensities at λ_{ex} = 490 nm were measured. The fluorescent intensity of all encapsulated carboxyfluorescein in the inner aqueous phase of the vesicle was measured according to the following procedure. 1.0 mL of carboxyfluorescein-containing fullerene vesicle was diluted with 0.5 mL of saturated aqueous solution of ammonium chloride, and filtered through membrane filter (PTFE, ϕ = 0.20 μm) pH value was adjusted to the same value by 0.5 mM of sodium hydroxide, and final concentration of **C8(7Y)K** vesicle was adjusted to 13 μM.

Anticancer drug delivery.

1.0 M of *t*BuOK in THF (70.1 μL, 70.1 μmol) was added to a solution of penta-alkynyl fullerene **C8(7Y)H** (77.0 mg, 46.7 μmol) in THF (3.67 mL) at room

temperature. After stirring for 3 h, the portion of the reaction mixture of **C8(7Y)K** (12.5 mM, 0.40 mL, 5.0 μmol) was slowly injected into a solution of doxorubicin (3.07 mg, 5.3 μmol) in distilled-deionized water (2.1 mL) with stirring at 400 rpm for 1 min using a syringe pomp (ISIS CO.) to obtain doxorubicin-encapsulated **C8(7Y)K** vesicle (2.0 mM) in 16% THF/water. THF and water were removed by evaporation at ca. 7 kPa, and the final concentration of **C8(7Y)K** was adjusted to 2.0 mM. Further biotinylation was conducted using this vesicle solution. Stock solutions of **biotin-N**$_3$ (200 mM), copper(II) sulfate (20 mM), (+)-sodium ascorbate (40 mM), and triethylamine (200 mM) in distilled-deionized water was prepared. Doxorubicin-encapsulated **C8(7Y)K** vesicle (500 μL, 1 nmol) was added slowly with stirring to a solution of **biotin-N**$_3$ (25 μL, 0.50 nmol; 5.0 eq), copper(II) sulfate (25 mL, 0.50 nmol; 0.50 equiv.), (+)-sodium ascorbate (25 μL, 1.0 nmol; 1.0 eq), and triethylamine (25 μL, 5.0 nmol; 5.0 eq) at room temperature. After stirring for 6 days, the reaction mixture was passed through a column of Sephadex G-50 fine (GE healthcare Japan, Japan, ϕ 10 × 100 mm) to be separated with unreacted **biotin-N**$_3$ and doxorubicin, which was not encapsulated into the inner aqueous phase of the vesicle, and orange-colored fractions in the eluted solution were collected and diluted with distilled-deionized water to 5.0 mL ([**C8(7Y)K**] = 0.20 mM). The size of biotinylated **C8(7Y)K** vesicle was determined by DLS analysis.

The MTT assay is designed to measure the cell viability. Human liver carcinoma (Hep G2) cells were harvested, collected, and resuspended in 100 μL of D-MEM at a concentration of 2 × 10^4 cells per 1 well over a 96-well plate before the treatment of **C8(7Y)K** vesicles. Biotinylated vesicles and free DOX were diluted to a series of concentrations in 50 μL of PBS to prepare test solutions. Just before addition of the test solutions, the medium was removed and 50 μL of fresh medium was added. The test solutions were added into the wells in the 96-well plate, and the cells were incubated for 48 h at 37 °C in a

humidified atmosphere with 5 % of CO_2. At the end of cell culture, the number of viable cells in each wells of the wells was determined by a quantitative colorimetric staining assay using 3-(4,5-dimethylthiazol-2-yl)-2,5-diphenyl-tetrazolium bromide (MTT; Cell Proliferation Kit I (MTT); Roche) as followed the manufactured protocol. Briefly, after incubation for 48 h, 4 μL of MTT labeling reagent was added into the wells in the 96-well plate, and the cells were incubated for 4 h. After incubation, 100 μL of solubilizing solution was added to the wells in 96-well plate, and then incubated overnight at 37 °C in a humidified atmosphere with 5 % of CO_2. Absorbance at 550 nm of each wells was measured, and absorbance at 690 nm was used as a reference wavelength. The results were expressed as the relative value (%) of the control cells, which were incubated parallel with 50 μL of PBS.

The inhibitory concentration (IC_{50}, μM) was defined as a concentration required for inhibiting 50% of the cell growth. Each data point on the curve in Figure 4-13 is indicated as a median value and its error bar based on three parallel experiments. IC_{50} values and its standard errors were determined by the Dose-Response Logistic Model using software Kaleidagraph;

$$f(x) = \frac{(b-a)}{1+(x/c)^d} = \frac{100}{1+(x/c)^d}$$

where a, b, c, and d indicate minimum value (0%), maximum value (100%), IC_{50} value and gradient of a fitting curve, respectively.

Statistical analysis.

Differences among the experimental groups were detected using Student's t-test. Values are expressed as means ±SEM; $P < 0.05$ was considered significant.

References

[1] (a) Peer, D.; Karp, J. M.; Hong, S.; Farokhzad, O. C.; Margalit, R.; Langer, R. *Nat. Nanotechnol.* **2007**, *2*, 751–760. (b) Ganta, S.; Devalapally, H.; Shahiwala, A.; Amiji, M. *J. Control. Release* **2008**, *126*, 187–204. (c) Voskuhl, J.; Ravoo, B. J. *Chem. Soc. Rev.* **2009**, *38*, 495–505. (d) Worsdorfer, B.; Woycechowsky, K. J.; Hilvert, D. *Science* **2011**, *331*, 589–592.

[2] Ogura, T *PLoS one* **2012**, *7*, e46904.

[3] (a) Zhou, S.; Burger, C.; Chu, B.; Sawamura, M.; Nagahama, N.; Toganoh, M.; Hackler, U. E.; Isobe, H.; Nakamura, E. *Science* **2001**, *291*, 1944–1947. (b) Sawamura, M.; Nagahama, N.; Toganoh, M.; Hackler, U. E.; Isobe, H.; Nakamura, E.; Zhou, S.; Chu, B. *Chem. Lett.* **2000**, *29*, 1098–1099.

[4] Homma, T.; Harano, K.; Isobe, H.; Nakamura, E. *J. Am. Chem. Soc.* **2011**, *133*, 6364–6370.

[5] Homma, T.; Harano, K.; Isobe, H.; Nakamura, E. *Angew. Chem. Int. Ed.* **2010**, *49*, 1665–1668.

[6] Isobe, H.; Homma, T.; Nakamura, E. *Proc. Natl. Acad. Sci. U.S.A* **2007**, *104*, 14895–14898.

[7] Maeda, R.; Noiri, E.; Isobe, H.; Homma, T.; Tanaka, T.; Negishi, K.; Doi, K.; Fujita, T.; Nakamura, E. *Hypertens Res.* **2008**, *31*, 141–151.

[8] (a) Huisgen, R. *Proc. Chem. Soc.* **1961**, 357–369. (b) Huisgen, R. *1,3-Dipolar Cycloaddition Chemistry*; Padwa, A, Ed.; Wiley, New York, 1984, Vol. 1, pp 1–176.

[9] (a) Meldal, M.; Tornøe, C. W. *Chem. Rev* **2008**, *108*, 2952–3015. (b) Rostovtev, V. V.; Green, L. G.; Fokin, V. V.; Sharpless, K. B. *Angew. Chem. Int. Ed.* **2002**, *41*, 2596–2599. (c) Tornøe, C. W.; Christensen, C.; Meldal, M. *J. Org. Chem.* **2002**, *67*, 3057–3064.

[10] (a) Cavalli, S.; Tipton, A. R.; Overhand, M.; Kros, A. *Chem. Commun.* **2006**, 3193–3195. (b) Hassane, F. S.; Frisch, B.; Schuber, F. *Bioconjugate Chem.* **2006**, *17*, 849–854. (c) Schatz, C.; Louguet, S.; Le Meins, J.-F.;

Lecommandoux, S. *Angew. Chem. Int. Ed.* **2009**, *48*, 2572–2575.

[11] Young, R.; Henstra, S.; Chmelik, J.; Dingle, T.; Mangnus, A.; van Veen, G.; Gestmann, I. *Proc. SPIE* **2009**, 737803.

[12] Suwamura, M.; Iikura, H.; Nakamura, E. *J. Am. Chem. Soc.* **1996**, *118*, 12850–12851.

[13] Cass, A.; Finkelstein, A. *J. Gen. Physiol.* **1967**, *50*, 1765–1784.

[14] Sivakumar, K.; Xie, F.; Cash, B. M.; Long, S.; Barnhill, H. N.; Wang, Q. *Org. Lett.* **2004**, *6*, 4603–4606.

[15] Fink, D. W.; Koehler, W. R. *Anal. Chem.* **1970**, *42*, 990‑993.

[16] (a) Fusz, S.; Srivatsan, S. G.; Ackermann, D.; Famulok, M. *J. Org. Chem.* **2008**, *73*, 5069–5077. (b) Tantama, M.; Lin, W.-C.; Licht, S. *J. Am Chem. Soc.* **2008**, *130*, 15766–15767.

[17] Pluk, H.; Stokes, D. J.; Lich, B.; Wieringa, B.; Fransen, J. *J. Microsc.* **2009**, *233*, 353–363.

[18] Wilchek, M.; Bayer, E. A. ed. *Methods in Enzymology*, Academic Press, San Diego, 1990; Vol. 184.

[19] Steiger, B.; Padeste, C.; Grubelnik, A.; Tiefenauer, L. *Electrochim. Acta*, **2003**, *48*, 761–769.

[20] (a) Russell-Jones, G.; McTavish, K.; McEwan, J.; Rice, J.; Nowotnik, D. *J. Inorg. Biochemistry* **2004**, *98*, 1625–1633. (b) Chen, J.; Chen, S.; Zhao, X.; Kuznetsova, L. V.; Wong, S. S.; Ojima, I. *J. Am. Chem. Soc.* **2008**, *130*, 16778–16785.

[21] Still, W. C.; Kahn, M.; Mitra, A. *J. Org. Chem.* **1978**, *43*, 2923–2925.

[22] Pangborn, A. B.; Giardello, M. A.; Grubbs, R. H.; Rosen, R. K.; Timmers, F. J. *Organometallics* **1996**, *15*, 1518–1520.

[23] Yao, F.; Li, C.; Vadivel, S. K.; Bowman, A. L.; Makriyannis, A. *Bioorg. Med. Chem. Lett.* **2008**, *18*, 5912–5915.

[24] (a) Provencher, S. W. *Biophys. J.* **1976**, *16*, 27–41. (b) Provencher, S. W. *Comp. Phys. Comm.* **1982**, *27*, 213–227.

Chapter 5. Summary and Outlook

For the development of the drug delivery system, I focused on the water-soluble fullerene derivatives because of their potential of unique self-assembled structure, such as micelles and vesicles.

First, I have developed lung-specific delivery system of siRNA using a water-soluble cationic amino-fullerene, TPFE (Figure 5-1). In chapter 2, I found that TPFE effectively binds with siRNA and stabilizes siRNA from nucleases by means of the formation of globules with electrostatic interactions. TPFE can deliver siRNA to the cells and release it in the cytosol in vitro. In chapter 3, I have demonstrated the agglutination-induced lung-specific siRNA delivery. Importantly, the size increase of the globules with plasma proteins from submicrometer to micrometer leads to the lung selectivity by trapping in the narrow lung capillaries (ca. 5 μm), and lung-selective knockdown was achieved without any acute toxicity. Lung accumulation and lung RNAi activity suggest that TPFE rapidly delivers siRNA into lung cells as well as immediately releases siRNA to cytoplasm. Finally, I succeeded the therapeutic application for the treatment of sepsis. This system will be helpful to design the therapeutic application for the various lung diseases, especially for the lung cancer because of the concept of enhanced permeation and retention (EPR) effect.[1]

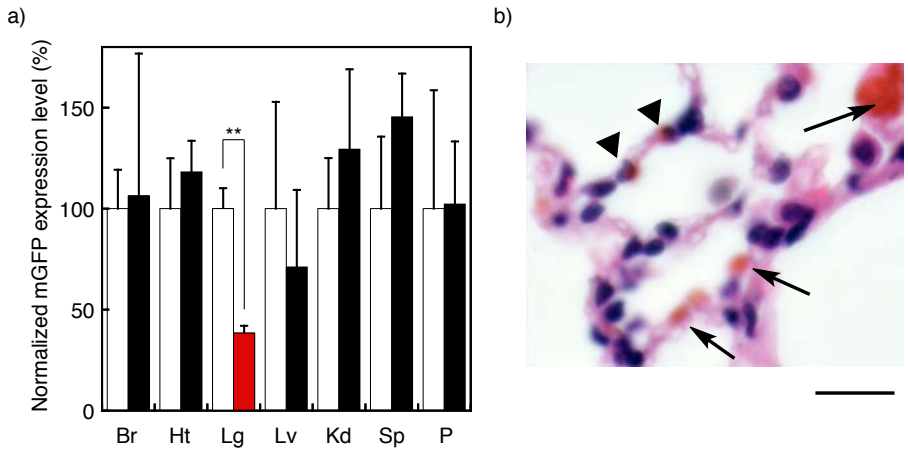

Figure 5-1. Lung-specific delivery of siRNA by a water-soluble cationic amino-fullerene, TPFE. a) Lung specific knockdown analyzed by qRT-PCR. Error bars are SEM. ** $P < 0.005$. b) Accumulation of TPFE-siRNA complex in the lung capillaries and the lung cells. H&E staining of lung section. Black arrow heads and arrows indicate TPFE-siRNA complex localized in the lung cells and the lung capillaries, respectively.

In chapter 4, I focused on the fullerene vesicles as a drug delivery vehicle. The fullerene vesicles are known as a thermally stable and low permeable bilayer membrane compared with conventional lipid-based membranes.[2] For the application to the drug carrier, I have developed the stepwise covalent and non-covalent post-functionalization of the fullerene vesicle (Figure 5-2). Terminal alkyne-tethered fullerene **C8(7Y)K** vesicle was prepared, modified with ligands via Cu(I)-catalyzed azide-alkyne click reaction, and characterized their structures and properties. By using a state-of-the-art sub-nm-resolution low-acceleration-voltage scanning electron microscopy (SEM), the vesicles can be observed high resolution without any metal coating. This SEM observation combined with indium-tin oxide (ITO)/glass substrate provides a new single molecule-level approach to the analysis of nanometer-sized organic molecules and materials.[3] Finally, I achieved antitumor activity in vitro by extremely low amount of anticancer drug

delivered by this motif.

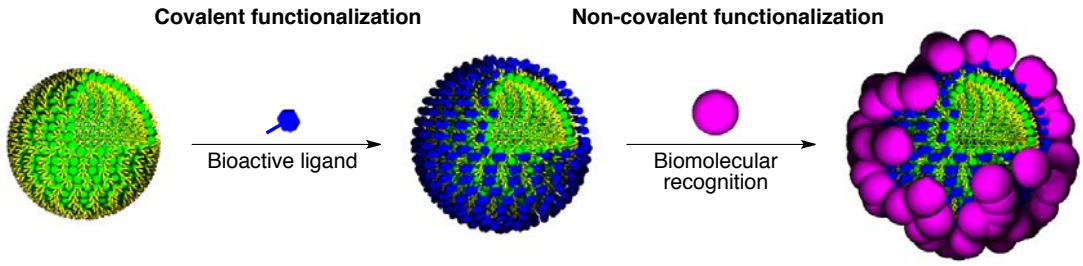

Figure 5-2. Schematic illustration of stepwise covalent and non-covalent post-functionalization of the **C8(7Y)K** vesicle.

Although a large number of researches about [60]fullerene have been studied in many fields including material and biomedical sciences, since its discovery, the study of [60]fullerene has not been well established yet now. For example, in the biomedical science, long-term toxicity has not been reported yet because of the shortness from the discovery. However, this study described in this thesis will contribute to enlarge the research field of [60]fullerene toward the supramolecular chemistry and biomedical sciences.

Reference

[1] Matsumura, Y.; Maeda, H. *Cancer Res.* **1986**, *46*, 6387–6392.

[2] (a) Homma, T.; Harano, K.; Isobe, H.; Nakamura, E. *J. Am. Chem. Soc.* **2011**, *133*, 6364–6370.; (b) Isobe, H.; Homma, T.; Nakamura, E. *Proc. Natl. Acad. Sci. U.S.A.* **2007**, *104*, 14895–14898.

[3] Nakamura, E. *Angew. Chem. Int. Ed.* **2013**, *52*, 236–252.